Universitat Politècnica de Catalunya

Departament de Física

Dynamics of large-scale shoreline perturbations.

Memòria presentada per

Jaime Alonso Arriaga García

per optar al grau de Doctor en Ciències.

Directors:

Francesca Ribas Prat

Albert Falqués Serra

Barcelona, Febrer del 2018

Contents

Chapter 1

Introduction

1.1 Motivation

The beaches are complex environments where many processes occur at the same time. The boundary between the wet beach and the dry beach, i.e. the shoreline, is a visible feature and its behaviour is an indication of the dominating processes and constraints of the system. Shorelines around the world are rarely smooth and they can present undulations and cuspate shapes. In this thesis, the term coastline perturbations is used to refer to deviations of the shoreline from an otherwise straight shoreline. On the one hand, human actions can cause shoreline perturbations via structures or beach nourishments. This human interference introduces a perturbation into the system, either in the wave field, which drives morphological changes, or in the beach itself. On the other hand, nature alone can also introduce perturbations to the coastal system via geological constraints or by positive feedbacks between the driving forces and the morphological changes.

This thesis combines field observations and morphological models to improve the understanding of large-scale coastal perturbations. Two sites are mainly studied: the Delfland Dutch coast, where a very large nourishment called Sand Engine was constructed in 2011, and the Dungeness Cuspate Foreland, which is a natural perturbation that has been evolving for thousands of years.

1.1.1 Shore nourishments

Shore nourishments consist of dumping sand on the coastal system and are used to mitigate beach erosion. This excess of sand is typically transported in time out of the nourishment area in the cross-shore and in the alongshore directions. The most well-known nourishment is the beach nourishment, perhaps due to its immediate visual impact. Sand is deposited on the sub-aerial beach, advancing the shoreline seaward (Dean, 2002). As a consequence,

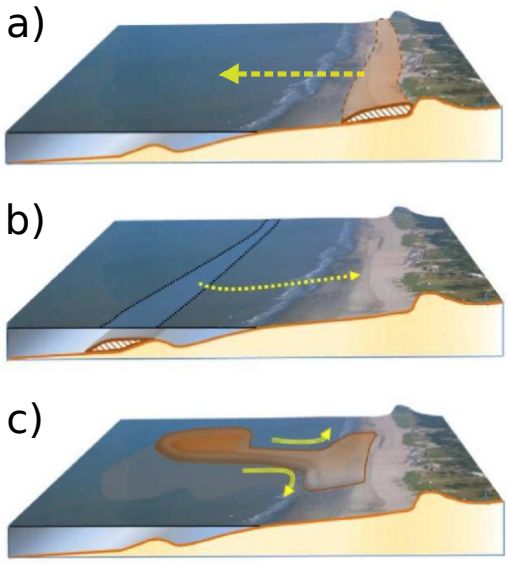

Figure 1.1.1: Conceptual diagram of the different nourishment strategies: a) beach nourishment, b) shoreface nourishment, and c) localized mega-nourishment. The yellow lines indicate the expected direction of sediment transport. Image modified from Stive et al., 2013.

the initial cross-shore profile is steeper than the original beach profile. The modification of the beach profile favours an initially rapid diffusion in the cross-shore direction while the alongshore diffusion is directly related to gradients in the alongshore sediment transport. The latter process is easily understood through a parametrisation of the alongshore sediment transport like the CERC equation (Komar, 1998)

$$Q(y) = \mu H_b^{5/2} \sin(2\alpha_b), \tag{1.1.1}$$

where H_b is the wave height at breaking and $\alpha_b = \theta_b - \phi_s$ is the angle between the wave angle at breaking, θ_b, and the local shoreline, ϕ_s. Therefore, even with a uniform wave field, the nourishment is expected to experience alongshore gradients due to the ϕ_s dependence (i.e. the perturbation in the shoreline angle) ant thereby diffuse. Other wave alongshore sediment transport parametrisations give similar qualitative results.

Another type of nourishment is the shoreface nourishment, for which the sand is deposited as a submerged berm within the active zone of the cross-shore profile, i.e. the zone were wave stirring affects the sandy bed, (Dean, 2002). Two mechanisms are present in this type of nourishment. The first one is the cross-shore feed due to the modification of the beach profile. Instead of the sand being transported offshore, as occurs for beach nourishments, the sand is transported onshore because the modified beach profile is less steep than the original one. The second one is the lee effect related to the perturbation of the wave transformation. The submerged sand causes wave focusing leading to gradients in alongshore sediment transport. In this case, the terms initially affected in Eq. (1.1.1) are the ones comprising the wave

transformation H_b and θ_b. More specifically, there will be accretion in the lee side of the submerged sand. However, this can also cause a down drift erosion zone (van Duin *et al.*, 2004).

Mega-nourishments: The Sand Engine

Nourishment strategies, that is their size and time periodicity, varies in different countries. Spain, Italy and France have an interest in coastal development (e.g. harbours) and apply a reactive strategy when negative impacts induced by these projects require coastal stabilization (Hamm *et al.*, 2002). In The Netherlands, coastal protection follows a preventive strategy and is a high-level priority as reflected by its coastal policy of maintaining the coastal position at its 1990 position (de Ruig & Hillen, 1997; Mulder *et al.*, 2011). In 2000 it was decided to extend the policy and also maintain the volume in the area between 20-m depth and the landward boundary of the dune area. The annual average nourishment volume since 1990 of about 6 Mm^3 was raised to 12 Mm^3 (see the trend in Fig. 2 of Stive *et al.*, 2013). More recently, a Dutch State Committee delivered recommendations on how to keep the Netherlands flood proof over the next century in the light of human-induced climate change and accelerated sea-level rise (Stive *et al.*, 2013). In line with their recommendations, The Netherlands adopted an innovative intervention approach named "The Sand Engine" or Zand Motor in Dutch. From now on it will be here referred also as ZM.

The ZM is a hook-shaped mega-nourishment of 17 Mm^3 which contains 1.5 times more sand than the quantity of sand used in the whole Dutch coast since the policy extended to also maintaining sand volume. The ZM had an initial alongshore length of 2.5 km and offshore extension of 1 km. It was constructed from March 2011 to July 2011 (Fig. 1.1.2) within the 17-km long beach section (Delfland coast) bounded by the harbours of Scheveningen and Hoek van Holland. Furthermore, the design contained a small lake to prevent the freshwater lens in the dunes to migrate seaward. This mega-nourishment presents characteristics of both the beach nourishments and the shoreface nourishments. In fact, this perturbation affects the wave transformation and the local shoreline angle, i.e. every term in Eq. (2.2.9). Therefore, the mega-nourishments have more complex dynamics than the traditional nourishments and the study of their dynamics is very recent.

1.1.2 Shoreline self-organized patterns

The early studies of alongshore rhythmic patterns in the coast assumed the pre-existence of templates-spatially organized structures in either the hydrodynamics or the underlying geology. More specifically, it was assumed that its shape would be imprinted on unconsolidated sand (Coco & Murray, 2007). Indeed, this occurs for example in the Carchuna system (Southern Spain) where the observed shoreline undulations are related to the wave refraction influenced by submerged canyons (Ortega-Sánchez *et al.*, 2014). As a consequence, these features are stable and quasi static. In contrast, there are shoreline undulations that are highly dynamic, exhibiting growth and migration. The self-organization theory is now the most accepted theory to explain such rhythmic undulations in the shoreline (see Coco & Murray, 2007). The main difference between the template-forcing theory and the self-

Figure 1.1.2: Aerial photograph of the Sand Engine in July 2011.

organization theory is that the morphological changes driven by a template forcing do not affect the template forcing itself, while in the framework of self-organization a positive feedback occurs between the hydrodynamics and the morphological changes driven by it. This positive feedback implies an instability of a featureless situation and is precisely the cause of the pattern formation.

Potentially self-organized shoreline undulations can be observed at different spatial and temporal scales and are related to different processes. Beach cusps are the smallest features with metres/hours characteristic scales and are related to swash zone processes (Werner & Fink, 1993; Coco *et al.*, 1999, e.g. Fig. 1.1.3a). Mega-cusps are larger features with hundreds-of-metres/weeks characteristic scales and are related to rip channels connected to rhythmic sand bars (Deigaard *et al.*, 1999; Calvete *et al.*, 2005, e.g. Fig. 1.1.3b). Shoreline sand waves are even larger features with kilometres/years characteristic scales and have been related to the energy dispersion produced by wave refraction of highly-oblique incoming waves (Zenkovitch, 1959; Ashton *et al.*, 2001; van den Berg *et al.*, 2012; Kaergaard & Fredsoe, 2013*a*, e.g. Fig. 1.1.3c). The present work deals with these larger features and due to its characteristic scales will be referred to as Kilometric-scale Shoreline Sand Waves (KSSW). The driving mechanisms are discussed in detail in Section 1.3.

Shoreline sand wave observations

From the observational point of view, the dynamics of the formation and evolution of KSSW has been difficult to study due to their large length and time scales. On one hand, these scales complicate the systematic measurement of the beach. Although the advances in satellite imagery have increased the observations of shorelines at large scales, bathymetric measurements are scarce. These bathymetric observations are necessary to understand the role played by wave-related processes. Nevertheless, there are many sites where km-scale

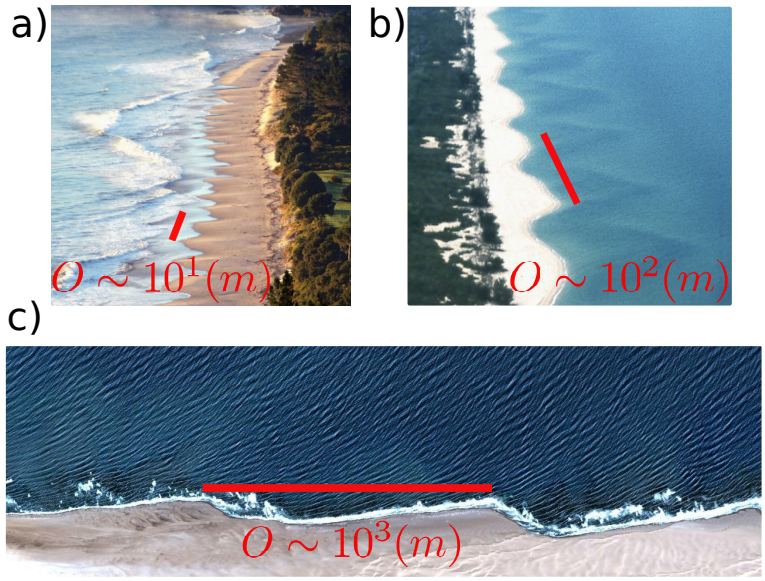

Figure 1.1.3: a) Beach cusps at Hahei Beach, N.Z. (modified from Coco and Murray, 2007). b) Mega-cusps at Cape York, Australia (modified from Coco and Murray, 2007). c) Shoreline sand waves at Namibia, Africa (downloaded from Google Earth). The wavelength order of magnitude of the patterns is illustrated in red.

shoreline sand waves have been observed and some of them have quantitatively been described in the literature. In the Holland coast, systematic alongshore wavelike behaviour, derived from topographic profiles, was observed with wavelengths of 3.5-7 km, amplitudes of 5-20 m, and a migration celerity of 0-70 m/yr (Ruessink & Jeuken, 2002). On the shore of Lake Erie (USA), Davidson-Arnott & van Heyningen (2003) used aerial photographs and topographic surveys to track shoreline sand waves with lengths in the range of 0.35-1.6 km, amplitudes of 50-100 m and a migration rate of about 150-300 m/yr. In El Puntal spit (Santander, Spain), Medellín *et al.* (2008) observed with a monitoring video system the formation of undulations with wavelengths of 0.1-0.2 km. These are the smallest ones so far reported in the literature. Intriguingly, no migration was observed. In the eastern Gulf of Finland sand waves were detected using field measurements and aerial/satellite images. Ryabchuk *et al.* (2011) found wavelengths of 0.3-1 km with amplitudes of 15-200 m and a migration rate of about 100 m/yr. In the West Coast of Denmark, Kaergaard *et al.* (2012) used measurements of cross-shore profiles to describe undulations with a wavelength of about 5-6 km, amplitudes up to 100 m and a migration rate of about 370 m/yr. At the south-west coastline of Africa, in Namibia and Angola, Ribas *et al.* (2013) used satellite images to study sand waves with wavelengths of 2-8 km, amplitudes of 60-175 m, and a migration rate of 50 m/yr (as was previously reported in a study by Elfrink *et al.*, 2003).

All these studies focused on fully formed KSSW and they were correlated with wave climates having large wave obliquity (the wave climate in Denmark is in the limit of obliquity). In one way or another, the studies presented limitations related to the large scales

of the features. The only study that observed formation events was the one performed by Medellín *et al.* (2008). However, no migration was observed despite the fact that, due to the configuration of the bay, incoming waves were almost always from the same direction and very oblique. Therefore, there is not yet a fully satisfactory test on the origin of KSSW due to high-angle waves.

1.2 Shoreline modelling

The prediction of shoreline evolution requires the solution of an equation that describes the dynamics of the shoreline (this will be treated later in detail). Such equation can be solved analytically or numerically. The analytic solutions are efficient (and elegant) and only require the initial morphological state and the forces acting upon it to give a prediction at any time. However, their solution assumes that the shoreline has a shape that can be described by a given function (see Pelnard-Considère, 1956) and can not be used for complex cases where the shoreline does not follow that particular function. In contrast, the numerical approach is more flexible but the cost comes in the form of number of computations. Here, a classification emerges: the behaviour-based models and the process-based models. The behaviour-based ones are characterised by parametrisations and by imposed behaviour rules (ideally derived from nature observations). The process-based ones are characterised by a free morphological evolution following the physical processes included in the model. Being rigorous, there are no pure process-based models since always, without exception, an assumption/parametrisation is required (i.e. an imposed behaviour). Thus, the numerical models have to be placed in some point in between of the purely behaviour-based and the purely process-based spectrum. Nevertheless, this philosophical conundrum can be avoided by considering the various scales. If the scale of interest is of the order of 10^1 m and 10^0 d (like occurs for beach cusps), then the model parametrisations have to be done, at least, at an order of magnitude smaller (10^0 m and 10^{-1} d) to be considered process-based. In this way, the same model can be behaviour-based or process-based depending on the scale of interest. As a general rule, the more processes are included in the model (and more detailed) the more expensive the computational cost will be.

The large scales of mega-nourishments (and those of shoreline sand waves), together with current computational power, limit the detail level at which physical processes can be successfully modelled. Also it can be assumed that smaller scale processes do not play a major role in the large-scale shoreline dynamics. In shoreline modelling, the approach most widely used is the numerical solution of the one-line equation. These models are based on the assumption that shoreline changes are caused only by gradients in the wave-driven alongshore sediment transport and ignore surf zone processes (e.g. rip currents, rhythmic sand bars, alongshore current meandering, etc). Once the alongshore sediment transport is computed, the gained/lost sediment is assumed to redistribute instantly in the cross-shore direction, until the depth of closure D_c, maintaining a prescribed shape of the cross-shore profile (i.e. an imposed behaviour). The reasoning for imposing such behaviour is that the beach profiles will experience the same wave forcing and that such wave forcing will cause the profile to achieve an equilibrium (i.e. the prescribed shape of the cross-shore profile) in

the long term. The resulting shoreline advance/retreat follows the equation

$$\frac{\partial x_s}{\partial t} = -\frac{1}{D_c}\frac{\partial Q}{\partial y}, \tag{1.2.2}$$

where the y axis corresponds to the mean alongshore direction, Q is the alongshore-sediment transport rate (m^3/s), computed with Eq. (1.1.1), t is time (s), and $x_s(y,t)$ (m) is the shoreline displacement respect to the mean shoreline. Due in partly to computational power, the classic one-line approach ignores the feedback between the morphology and the wave field, i.e. H_b and θ_b remain constant and alongshore uniform. This assumption also allows to find analytic solutions for Eq. (1.2.2), assuming different shoreline function shapes (e.g. Gaussian, see Pelnard-Considère, 1956). Following the growth in computational power, the one-line approach evolved to include the feedback between the morphology and the wave field (e.g. see the Genesis shoreline change model by Hanson, 1989), which proved to reduce the diffusion of shoreline perturbations (Falqués & Calvete, 2003) and thus the relevance of the correct representation of the bathymetric contours. Nevertheless, the instantaneous sediment redistribution means that the cross-shore shape and size of the shoreline is the same as those of every bathymetric contour. A better estimation of the contours is achieved by the N-line models for which the cross-shore profile is treated as N interacting layers. The long-shore profile of each contour evolves in the same way as a one-line model but with cross-shore exchange between layers (Hanson & Larson, 2001). However, the N-line models have not been used often, mainly because the cross-shore behaviour requires much more calibration and set-up effort than one-line models. Furthermore, those models do not always provide more information than that needed for calibration. Later on, Falqués *et al.* (2008) and, more formally, van den Berg *et al.* (2012) extended the one-line approach to a quasi-two-dimension approach by treating the alongshore sediment transport and the cross-shore sediment transport in a different way: the alongshore sediment transport is distributed across the profile, following the shape of the wave-alongshore current, the cross-shore transport lets the sediment of a non-equilibrium profile to slowly redistribute to eventually achieve its equilibrium shape. The representation of the bathymetric contours improved (i.e. the cross-shore shape and size of the shoreline is not necessarily the same as those of the bathymetric contours) but the treatment of the shoreline as a boundary (with exchange sediment between the dry and wet zones) imposed a model constraint to the maximum shoreline orientation (of 13°).

There are models that follow other philosophies: the cellular automata models and the linear stability models. The cellular automata models are characterized by defining cells, whose behaviour will depend on their neighbouring cells according to some rule (e.g. the most famous cellular automata model is the Conway's Game of Life, see Gardner, 1970). Ashton *et al.* (2001) combined the cellular automata concept with the one-line model concept by defining the alongshore sediment transport in each cell from deep-water wave variables (see Eq. 1.3.3). Therefore, no need for wave transformation was required since it was implicitly included in the alongshore sediment transport computation. Later, by applying linear stability analysis to the one-line modelling approach, Falqués & Calvete (2005) proposed a model to compute the growth rate and celerity of infinitesimal-amplitude sinusoidal perturbations. Therefore, the model only gives information about this type of perturbation. This model also assumes instantaneous profile changes but the cross-shore amplitude of the associated bathymetric contours can be variable. In the present thesis, the model of Falqués & Calvete (2005) is used to study the formation of KSSW and the model of van den Berg *et al.* (2012) is modified and used to study the dynamics of mega-nourishments.

1.3 Shoreline instabilities

Zenkovitch (1959) observed large-scale cuspate shapes along the shores of elongated lagoons. This characteristic, the elongation, favours the predominance of wind-driven waves in a particular direction. The dominant waves formed a high-angle with respect to the shore normal of the observed features. Zenkovitch (1959) explained that the alongshore transport is maximum for a certain wave incidence angle and that, above this angle, waves could originate such undulations.

Grijm (1960) explored for the first time the effect of the maximising-transport angle with a mathematical approach. Using a simple alongshore transport sinusoidal function a critical angle of 45°-60° was obtained. Later, Wang & LeMehaute (1980) used linear wave theory and an alongshore transport expression proportional to the alongshore component of wave energy flux at breaking to demonstrate that a maximum in alongshore transport is obtained for high-angle waves at deep waters ($\theta_\infty = 42°$) despite obtaining breaking-wave angles (after wave refraction) in the range of 2°-25° (depending on wave steepness). Their approach related θ_b to θ_∞ through linear wave theory and used an empirical relation to compute H_b from H_∞. Then, Ashton *et al.* (2001) improved upon this approach, avoiding the empirical relation of H_b, and relating the CERC equation to deep-water wave conditions (H_∞, θ_∞ and T_p, wave period). They also used linear wave theory and assuming refraction over contours locally parallel to the shoreline,

$$Q = K {H_\infty}^{12/5} {T_p}^{1/5} \cos^{6/5}(\theta_\infty - \phi) \sin(\theta_\infty - \phi). \tag{1.3.3}$$

Using this expression, the maximum of Q also occurs at 42° (Fig.1.3.4, left panel). This can be better understood if we suppose a sinusoidal shoreline (see blue line in Fig. 1.3.4) and apply Eq. (1.3.3) supposing a 30° and a 45° (Fig. 1.3.4, right panel). For the first case, the maximum of Q is found down-drift of the perturbation tip while, for the latter case, the maximum of Q is found up-drift of the perturbation tip. The latter implies a convergence of sediment near the tip area and therefore the perturbation will grow.

Ashton *et al.* (2001) modelled the evolution of shoreline sand waves (and other shoreline features) using a non-linear cellular model (also based on the one-line modelling approach), assuming the same wave transformation as for their deep-water CERC equation and by imposing periodic boundary conditions. Indeed, they found that small perturbations grew for wave conditions with an angle higher than the critical one. This mechanism has been referred to as High-Angle Wave Instability (HAWI). Their approach implicitly i) neglects the curvature of the depth contours, ii) neglects the offshore weakening of the undulations, and iii) assumes that the perturbation reaches very deep waters. These assumptions limit its applicability to very large scales (longer than the ones of the shoreline sand waves). Later, Falqués & Calvete (2005) took into account the wave transformation over curvilinear depth contours (up until the depth of closure) to study the dynamics of small-amplitude KSSW and its dependence on the bathymetric perturbation assumptions. Interestingly, they found that, for a given set of geomorphological conditions, there is a dominant wavelength. This preferred-wavelength behaviour was also found by Uguccioni *et al.* (2006). Other studies focused on understanding the role played by the depth of closure, the shape of the profile, and the percentage of oblique waves necessary for the instability to grow (see Ashton & Murray, 2006*b*; Falqués, 2006; Falqués *et al.*, 2011; van den Berg *et al.*, 2011, 2012; Kaergaard & Fredsoe, 2013*a*,*b*). Until this point, the onset of the instability was explained by the action

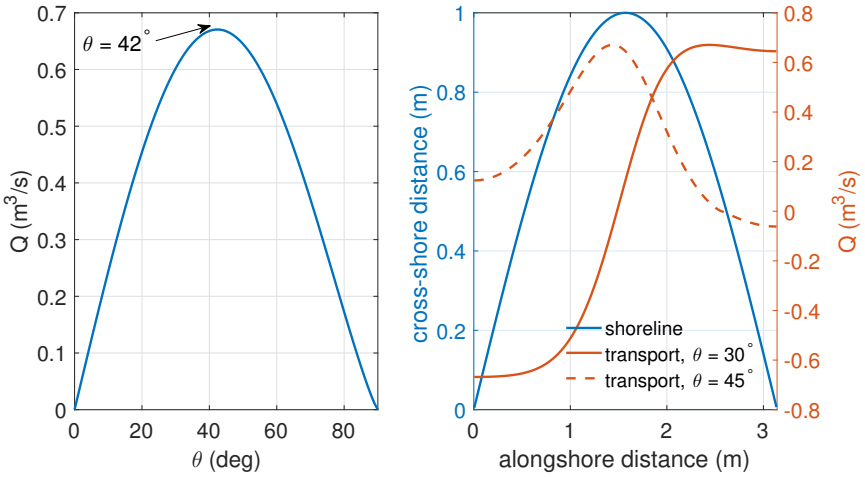

Figure 1.3.4: Alongshore sediment transport computed with Eq. (1.3.3) for various deep-water angles with the same wave height (left). Alongshore sediment transport along a parabolic shoreline for two wave incident angles (right).

of two physical effects: I) the relative wave angle with respect to the local shoreline, being larger at the down-drift flank of the KSSW crests, and II) the concentration of wave energy at the up-drift flank due to less refractive energy dispersion. van den Berg *et al.* (2014) analysed a third physical effect: III) wave energy concentration slightly down-drift of the KSSW crest due to refractive focusing. The wave-focusing effect explained the preferred wavelength for a determined beach state and wave forcing. Roughly, they found that the alongshore length scale of the KSSW equals the wavelength of the water wave offshore over the mean shoreface slope, λ_o/β.

The evolution of the shoreline depends on the wave field, which in turn depends on the bathymetric perturbation. Therefore, it is necessary to define a link between the shoreline and the depth contours. Most of the previously described studies assume that this link is achieved by a shift of the cross-shore profile following the shoreline perturbation, i.e. that the contour undulations have the same cross-shore amplitude as the shoreline. This is done either instantaneously or gradually in time. Falqués & Calvete (2005) proposed a different perturbation shape: a linear seaward decay of the bed elevation. In this case, the cross-shore amplitude of some of the contours can be larger than the one of the shoreline. Idier *et al.* (2011, 2017) proved that, as a result, the shoreline could become unstable, even for waves with an angle below the critical one of HAWI. Under these conditions, the stabilizing effect of the wave angle in HAWI (see I) in the previous paragraph) can be reversed and become destabilizing, i.e. the maximum of the relative wave angle is localized at the up-drift flank of the sand waves. This mechanism has been referred to as Low-Angle Wave Instability, LAWI (Idier *et al.*, 2011, 2017).

Testing HAWI and LAWI in nature has proven to be very challenging due to the lack of

data on KSSW observations (see Section 1.1.2) but it is plausible that they can both occur in nature. The lack of information is the reason why many studies comparing modelling with observations have done assumptions, either about the wave climate or about the reach and type of perturbation (Falqués, 2006; Kaergaard *et al.*, 2012; Ribas *et al.*, 2013; Falqués *et al.*, 2017). Therefore, a conclusive study to test HAWI and LAWI in nature is still lacking.

1.4 Research objectives and outline

The main aim of the present work is to provide more insight into the dynamics of shoreline large-scale perturbations with an emphasis on the wave obliquity. In particular, the next specific objectives are defined: i) improve the capabilities of the Q2Dmorfo model, ii) validate the 1Dmorfo model and the Q2Dmorfo model with field observations, iii) investigate the dynamics of mega-nourishments, and iv) improve the understanding of the formation of shoreline sand waves.

Previous studies have used low-resolution data to study the evolution of large-scale perturbations. In this thesis, the widely monitored ZandMotor is used to validate the Q2Dmorfo model. In order to handle the large shoreline slopes exhibited by the ZandMotor, the sand exchange between the dry beach and the wet beach is now treated with a fuzzy shoreline algorithm. Afterwards, the long-term behaviour of its diffusion and feeding capabilities to the adjacent coasts are analysed. Also, the role played by the wave forcing and the nourishment shape and size is investigated to further understand the mega-nourishment dynamics. Besides, a new site located in the South of the U.K. is studied. The formation of shoreline sand waves is described and, thanks to the available good-quality data, is used to validate the 1Dmorfo model.

The next research questions are answered in this thesis. The first two are related with modelling large-scale perturbation methodologies. The next four questions arise after the construction of the ZandMotor. The last ones are related with the lack of conclusive studies of shoreline sand waves formation in nature:

1) Can the fuzzy shoreline algorithm improve the performance of morphodynamic models?

2) Can the long-term evolution of a mega-nourishment be reproduced by current numerical models?

3) What is the long-term behaviour of the ZandMotor and in particular what is its lifetime?

4) What is the effect of wave obliquity in the evolution of a mega-nourishment? Could a mega-nourishment trigger the formation of shoreline sand waves?

5) What is the role played by the initial shape and size of a mega-nourishment on its own evolution?

6) Can the formation of km-scale shoreline sand waves be observed in nature, and if so,

is it linked to the wave climate?

7) How morphodynamic models results compare with observed shoreline sand wave formation?

This thesis is divided in 6 chapters. In chapter 2, the Q2Dmorfo model is described and modified to further expand the model capabilities to study large amplitude perturbations. In particular, a new algorithm to deal with the sediment transport in the shoreline is implemented. The new model version is compared with the previous one. Also, sea-level rise is implemented and compared against the Bruun rule prediction. Also, the 1Dmorfo model is briefly described and the cross-shore links between the shoreline and the bathymetry are tested to further understand and exemplify the HAWI and LAWI instabilities.

In chapter 3, the data of the first three years of evolution of the ZandMotor is used to calibrate and validate the Q2Dmorfo model. In particular, the parameters controlling the alongshore sediment transport strength and the cross-shore sediment transport strength and offshore reach are calibrated. Afterwards, realistic wave climates constructed with historical wave data are used to make long-term predictions of the Zandmotor behaviour.

In chapter 4, the general form of the 2D-Gaussian is used to imitate the perturbation of the ZandMotor. Once this is validated, the parameters of the 2D-Gaussian are varied to investigate the role played by its asymmetry, the shape ratio, and the volume of the mega-nourishment on its own long-term evolution. Also, the procedure to synthesize a real wave climate is optimized and then the probability of occurrence of the oblique waves is varied to better understand its effect on the long-term behaviour of a mega-nourishment.

In chapter 5, a 2-km stretch of beach located in the north-eastern flank of the Dungeness Cuspate Foreland is studied in detail. There, two formation events of shoreline sand waves are observed. The correlation of the wave climate characteristics with the formation events is investigated. Finally, the observed data is used to validate the 1Dmorfo model.

Finally, in chapter 6 a summary of the most relevant conclusions of each chapter is done by answering the proposed research questions. Also, future research lines are discussed.

Chapter 2

Description of the models

2.1 Introduction

In this thesis two morphodynamic models are used: the non-linear model Q2Dmorfo and the linear stability model 1Dmorfo. Both models provide complementary information about the shoreline dynamics, the 1Dmorfo model is very useful to study the initial formation of shoreline sand waves while the Q2Dmorfo model is useful to study the non-linear dynamics of beaches in the long-term. An important part of this thesis consists on modifying the Q2Dmorfo model. The Q2Dmorfo applications of this Chapter have the objective of showing the effect of the improvements made while the two research studies performed with this model are found in Chapters 3 and 4. Also in this Chapter, the 1Dmorfo is applied to simple scenarios to explain the model strengths, limitations and outputs while the research study performed with this model is found in Chapter 5.

The Q2Dmorfo model (or quasi-two-dimensional morphodynamic model) is a non-linear model for large-scale shoreline dynamics (1 km-100 km) on a medium to long-term time scale (months to years). In order to handle such scales in a computationally efficient way, the model is based on the assumption that the shoreline dynamics is controlled by the gradients in the alongshore transport and that the cross-shore beach profiles tend to a previously defined equilibrium profile. The alongshore sediment transport is parametrised directly from the wave transformation and follows the typical shape of the alongshore current. The resulting accumulated/eroded sediment causes profile perturbations. The perturbed profile

---

Subsection 2.2.5 is largely based on Arriaga *et al.* (2014): Arriaga, J., Ribas, F., Marino-Tapia, I. J. & Falqués, A. 2014 Km-scale shoreline sand waves: numerical modelling and observations. In *Coastal Eng. 2014*. Doi: 10.9753/icce.v34.sediment.68

Subsections 2.3.5 and 2.3.6 are partly based on Idier *et al.* (2017): Idier, D., Falqués, A., Rohmer, J. & Arriaga, J. 2017 Self-organized kilometre-scale shoreline sandwave generation: sensitivity to model and physical parameters. *J. Geophys. Res.* **122**, doi:10.1002/2017JF004197 and on Falqués *et al.* (2017): Falqués, A., Ribas, F., Idier, D. & Arriaga, J. 2017 Formation mechanisms for self-organized km-scale shoreline sand waves. *J. Geophys. Res. Earth Surf.* **122**, 10.1002/2016JF003964

is modelled to tend to the equilibrium profile by means of a diffusive cross-shore transport. Such transport is assumed to be stronger near the shoreline and to decay to a residual value beyond the active depth. The wave transformation computed over the evolving bathymetry takes into account refraction and shoaling over the curvilinear contours up to the breaking point. These simplifications limit the application to large-scale features. Consequently, surf-zone morphodynamic patterns such as near-shore sand bars and rip currents can not be modelled with the Q2Dmorfo model. Moreover, the tides and aeolian transport are neither taken into account.

A first version of the model was presented in Falqués *et al.* (2008). The next version, presented by van den Berg *et al.* (2012), included improvements in the discretization and the boundary conditions. This last version had two important shortcomings. First, the evolving shoreline was treated as a sharp boundary between the dry and wet beach, which was difficult to implement numerically. In particular, the model could not handle correctly the shoreline evolution when the shoreline deviated from the mean shoreline (y-axis) more than $\approx 13^{\circ}$. Second, the direction of the sediment transport followed the global x-axis and y-axis directions regardless of the shoreline orientation. The first model improvement in the present thesis is the implementation of the *fuzzy shoreline algorithm*: the dynamic equations are now solved throughout the whole domain and the shoreline is treated as a transition zone. This allows the description of larger shoreline deviations. The second improvement is that the cross-shore direction is computed locally as the direction of maximum bed level gradient (i.e. the normal direction to the local contours) of a smoothed bathymetry. Finally, the model has also been recently adapted to handle sea level variations.

The 1Dmorfo linear stability model, introduced by Falqués & Calvete (2005), aims to describe the dynamics of the small departures of the coastline with respect to a rectilinear shoreline. Therefore it is ideal to investigate the initial formation of shoreline sand waves and has previously been used to investigate such conditions (Falqués, 2006; Falqués *et al.*, 2011; Idier *et al.*, 2011; Falqués *et al.*, 2017; Idier *et al.*, 2017). The alongshore sediment transport is computed in a similar fashion as the Q2Dmorfo model but the cross-shore sediment transport assumes instantaneous changes of the beach profile. Unlike the Q2Dmorfo, the 1Dmorfo can describe diverse cross-shore transport dynamics, i.e. the shape of the bathymetric perturbations associated to the shoreline. This flexibility allowed to study diverse shoreline instability mechanisms (Falqués & Calvete, 2005; Idier *et al.*, 2011).

In Section 2.2 the improved Q2Dmorfo model is described with an emphasis on the improvements done in the sediment transport computation with respect to the model version presented by (van den Berg *et al.*, 2012). Also tests are performed to (i) compare the improved version of the model with the one of van den Berg *et al.* (2012) for the case of an evolving train of shoreline sand waves and to (ii) evaluate the sea level rise implementation by reproducing the Bruun rule (Bruun, 1962). In this thesis the 1Dmorfo model is not modified but a brief description is done in Section 2.3 with an emphasis on the shape of the assumed bathymetric perturbation. The model details can be found in Falqués & Calvete (2005). Also, tests are performed to (i) understand/explain the role played by two types of bathymetric perturbations, the first one related to the high-angle wave instability and the second one related to the low-angle wave instability, and to (ii) compare the 1Dmorfo model and the Q2Dmorfo model using the site of Srd. Holmsland Tange.

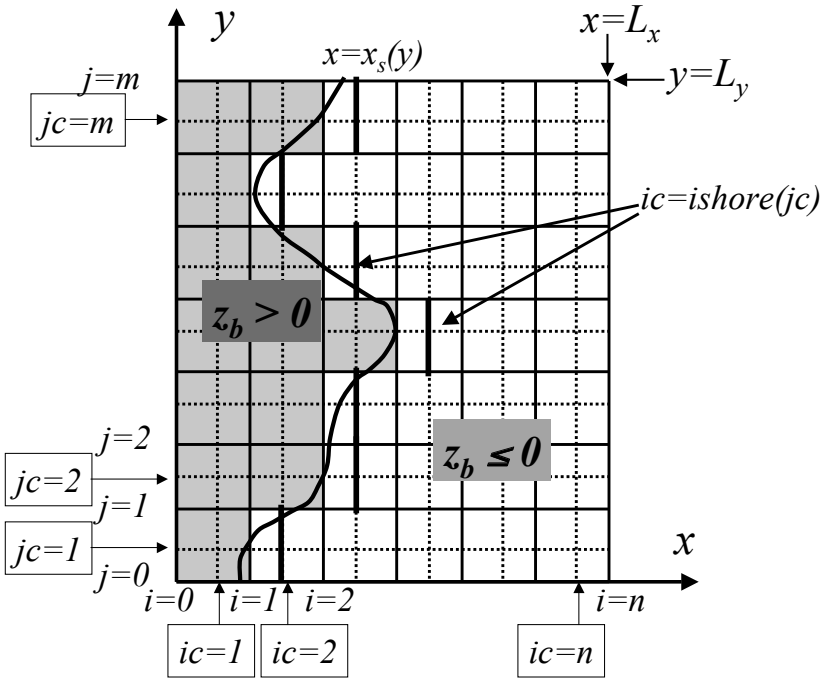

Figure 2.2.1: Geometry of the modelling domain and the staggered grid.

2.2 Q2Dmorfo model

2.2.1 Grid, equilibrium profile and bathymetry

The model uses a Cartesian frame of reference, where the y-axis is parallel to the mean shoreline and the x-axis is pointing offshore, and a rectangular domain ($0 < x < L_x, 0 < y < L_y$), L_x and L_y being the cross-shore and the alongshore domain lengths. A staggered grid is applied with x cell grid size, Δx, and y cell grid size, Δy (Fig. 2.2.1). The bed level is defined by $z_b(x, y)$. The shoreline position $x_s(y)$ is determined by interpolating in the cross-shore direction between the last dry cell ($z_b \geq 0$) and the first wet cell ($z_b < 0$), indicated by $ishore(y)$ in Fig. 2.2.1.

The model assumes that the beach has an equilibrium profile, which can be an analytic profile or can be read from an external file. For the former case, the model can be used with the modified Dean profile

$$z_{be}(x) = -b\left((x + x_0)^{2/3} - x_0^{2/3}\right), \tag{2.2.1}$$

where x_0 is a small shift to avoid an infinite slope at the shoreline and $b = (3/2)\beta {x_0}^{1/3}$, β being the slope of the swash zone (used by Falqués & Calvete, 2005). Alternatively, the model can be used with the double slope profile without bars

$$z_{be}(x) = -a_1 \left(1 - \frac{\beta_2}{\beta_1}\right) \tanh\left(\frac{\beta_1 x}{a_1}\right) - \beta_2 x, \tag{2.2.2}$$

were β_1 is the slope near the shoreline and β_2 is the slope defined at the depth a_1 (used by Yu & Slinn, 2003).

The initial bathymetry, z_b, can be read from an external file or it can be constructed as an alongshore repetition of a cross-shore profile following an initial defined shoreline. Various initial perturbations can be added to the bathymetry (e.g. random small scale perturbations, alongshore rhythmic perturbations, and a localized large scale perturbation). In general, it is recommended to create the bathymetry externally, taking care that the profiles are similar to the equilibrium profile.

2.2.2 Wave transformation

The wave module takes into account refraction and shoaling over the curvilinear contours by assuming monochromatic waves with $T = T_p$ (peak period), $H = H_{rms}$ (root-mean-square wave height) and a wave angle θ. The waves are propagated from the offshore boundary (H_0, T_0, θ_0) by solving in cascade a set of three decoupled equations: the dispersion relation, the equation for wave number irrotationality and the wave energy conservation equation:

$$w^2 = gk \tanh(kD), \tag{2.2.3}$$

$$\frac{\partial k_y}{\partial x} = \frac{\partial k_x}{\partial y}, \tag{2.2.4}$$

$$\frac{\partial}{\partial x}\left(c_g H^2 \frac{k_x}{k}\right) + \frac{\partial}{\partial y}\left(c_g H^2 \frac{k_y}{k}\right) = 0. \tag{2.2.5}$$

Here, ω is the radian frequency, g is the gravity acceleration, $\vec{k} = (k_x, k_y) = k(-\cos\theta, \sin\theta)$ is the wave number vector (where θ is the angle between wave crests and the y-axis), c_g is the group celerity, and $D = -z_b + \eta$ the local depth. Here, z_b is the bed level and η represents the sea surface level. As default, η is set to 0. These equations assume steady conditions and ignore wave diffraction, and wave energy dissipation by bottom shear stresses and wave breaking. From the computed wave field, we extract the breaker wave height, H_b, and the corresponding wave angle, θ_b, to feed the sediment transport equations. The breaking point is defined as the most onshore position where $H \leq \gamma_b D$, where γ_b is the saturation ratio of H/D in the surf zone and the value $\gamma_b = 0.5$ is used. The details about how Eqs. (2.2.3)-(2.2.4)-(2.2.5) are solved numerically can be found in van den Berg (2012).

2.2.3 Bed evolution and sediment transport

The changes in the bed level are computed with the sediment mass conservation equation

$$\frac{\partial z_b}{\partial t} + \frac{\partial q_x}{\partial x} + \frac{\partial q_y}{\partial y} = 0 \quad , \tag{2.2.6}$$

where t is the time and $\vec{q} = (q_x, q_y)$ is the depth-integrated sediment flux, which includes the bed porosity factor. This is the main governing equation and it is solved throughout the whole domain. The shoreline position, $x_s(y,t)$ is computed from the modelled depth $D = -z_b + \eta$ interpolating between the last wet cell and the first dry cell and is assumed to be a uni-valued function of y. This uni-value limitation implies that spit dynamics can not be modelled, which will have implications in Chapter 3.

Fuzzy shoreline

The model treats the shoreline as a transition zone; i.e. a fuzzy shoreline, which can be physically interpreted as the swash zone. Due to its global implications, the fuzzy shoreline is not a single algorithm but rather a general treatment for every sediment transport equation. This means that all the variables and functions change smoothly from certain values corresponding to the wet cells to other values corresponding to the dry cells. For example, the wave-driven alongshore transport is assumed to have a standard cross-shore distribution in the surf zone and decays to zero across the swash zone; i.e. taking into account the width of the swash zone. In addition, the factor in front of the cross-shore transport is assumed to have a certain distribution in the surf and shoaling zones and it is imposed to decay exponentially to zero across the swash, in this case an extra distribution is required for the dry cells (the mathematical details are described later in this section). This rather simple concept facilitates the numerical implementation of the sediment transport equations.

Evolving cross-shore direction

The cross-shore direction is defined for every grid point by taking into account the curvature of the shoreline and its associated bathymetric contours (Fig. 2.2.2). This helps to better describe the dynamics of largely perturbed beaches or with curvilinear shapes. The local normal direction to the bathymetric contours is represented by an averaged orientation, ϕ, evaluated as

$$\sin\phi = \frac{\frac{\partial \bar{z}_b}{\partial y}}{\sqrt{(\frac{\partial \bar{z}_b}{\partial y})^2 + (\frac{\partial \bar{z}_b}{\partial x})^2}}, \tag{2.2.7}$$

where the spatially averaged bed level $\bar{z}_b$ is computed within a rectangular box $L_l \times L_c$. Here, $L_l = 100$ m and $L_c = 50$ m are used. For the coastline angle, ϕ_s, the boxes do

not take into account the dry cells in order to avoid the influence from the dry beach. Following the model convention, the normal and tangential vectors to the bathymetric lines are $\hat{n} = (\cos\phi, -\sin\phi)$ and $\hat{t} = (\sin\phi, \cos\phi)$, respectively.

Sediment flux decomposition

The depth integrated sediment flux $\vec{q}$ is decomposed as

$$\vec{q} = \vec{q_L} + \vec{q_N} + \vec{q_D}, \tag{2.2.8}$$

where the first term, $\vec{q_L}$, represents the littoral drift driven by breaking waves and is evaluated by first computing the total sediment transport rate Q. As default, the CERC formula (Komar, 1998) is chosen,

$$Q(y') = \mu H_b^{5/2} \sin(2\alpha_b). \tag{2.2.9}$$

Here, H_b is the (rms) wave height at breaking and $\alpha_b = \theta_b - \phi_s$ is the angle between wave fronts at breaking and the coastline. Here, y' (instead of y) indicates that the variables H_b, θ_b and ϕ_s associated to each point correspond to the position found following the direction normal to the local coastline (instead of the global x direction, see Fig. 2.2.2). The μ constant is related to the non-dimensional K constant of the original CERC formula by

$$\mu = \frac{K}{16(s-1)(1-p)}\sqrt{\frac{g}{\gamma_b}}, \tag{2.2.10}$$

where s and p are the relative density and porosity of sediment, respectively. By setting $s = 2.65$, $p = 0.4$ and $\gamma_b = 0.5$, the range $K \sim 0.2 - 1.6$ suggested by Komar (1998) gives a range $\mu \sim 0.06 - 0.45$ $\mathrm{m}^{1/2}\mathrm{s}^{-1}$. The total Q is then redistributed across the profile with a normalized shape function, which is assumed to be similar to an alongshore current profile:

$$f(x') = \frac{4}{\sqrt{\pi}L^3} x'^2 \, e^{-(x'/L)^2}, \tag{2.2.11}$$

where x' is the distance to the shoreline and $L = 0.7X'_b + X'_{sz}$, with X'_b being the width of the surf zone and X'_{sz} being the width of the swash zone. The cross-shore coordinate x', and the distances X'_b and X'_{sz} are calculated in the direction normal to the local coastline by using the corresponding ϕ (Fig. 2.2.2). The cross-shore distribution $f(x')$ (Eq. 2.2.11) is based on alongshore current measurements reported by Komar (1998) for a wide range of beach profiles. Finally, we impose that the transport $\vec{q_L}$ is directed tangent to the local bathymetric lines,

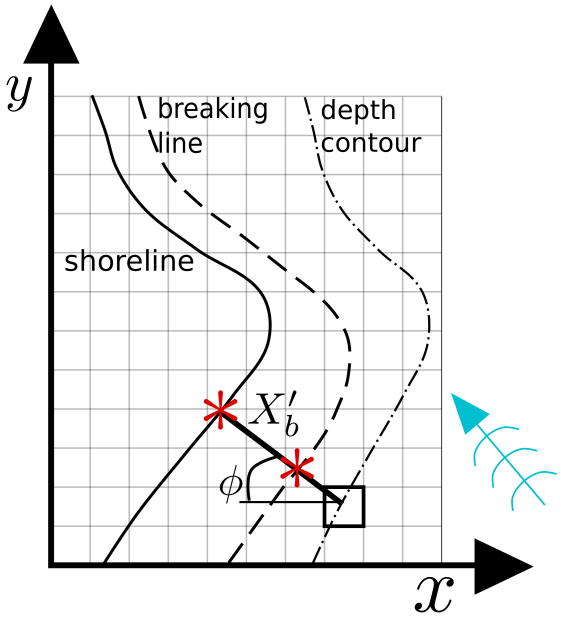

Figure 2.2.2: Sketch representation of the local cross-shore direction and the alongshore transport computation. The first asterisk indicates the position of ϕ_s and the second asterisk indicates the position of H_b and θ_b for the signaled grid cell.

$$\vec{q_L} = Q(y')f(x')\hat{t}. \tag{2.2.12}$$

The second term in Eq. (2.2.8), $\vec{q_N}$, stands for the transport that drives the bathymetry to a certain cross-shore equilibrium profile, i.e. it parametrises the cross-shore transport processes, and reads

$$\vec{q_N} = -\gamma_N(\nabla z_b \cdot \hat{n} + \beta_e)\hat{n}. \tag{2.2.13}$$

As can be seen, it is proportional to the difference between the equilibrium slope β_e, at the local depth $D = -z_b + \eta$, and the actual slope in the local shore-normal direction. An implicit assumption of this approach is that the equilibrium profile must be monotonic (without bars). The cross-shore diffusivity factor γ_N is related to the influence of orbital velocities and turbulence produced by incoming waves on the sea bed. Its order of magnitude has been estimated from the expression of momentum mixing (Battjes, 1975) and it is scaled with a power of wave height at breaking,

$$\gamma_N(x) = \nu_N \gamma_b^{-1/6} H_b^{11/6} X_b^{-1/3} \psi(x), \tag{2.2.14}$$

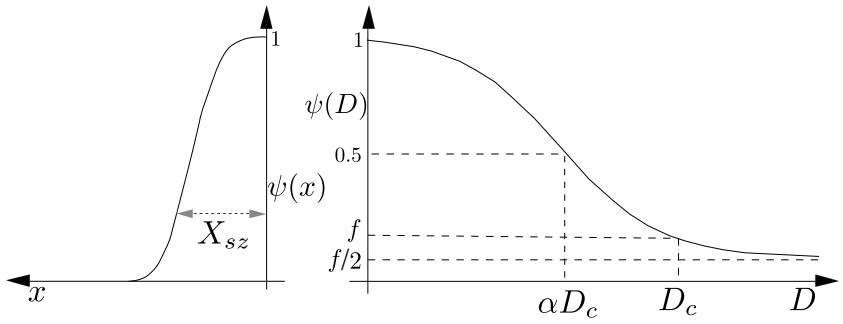

Figure 2.2.3: Sketch of the shape function ψ (Eqs. 2.2.15 and 2.2.16), which controls the cross-shore transport magnitude and is a proxy of the cross-shore behavior of wave stirring. A large residual value value f has been used in this sketch to allow a clear visualization.

where ν_N is a non-dimensional parameter that requires calibration. The factor γ_N varies throughout the bathymetry with a shape function ψ, which has a maximum at the shoreline and then decays offshore and onshore (Fig. 2.2.3). In the wet cells the expression

$$\psi(D) = \frac{1 + b + \tanh((\alpha D_c + z_b)/L_d)}{1 + b + \tanh(\alpha D_c/L_d)} \tag{2.2.15}$$

is adopted, which becomes 1 at the shoreline and decays to a given value f at $D = D_c$ (here, $f = 0.02$ and is controlled by the parameter b). The model instantaneous depth of closure, D_c, is computed as a fraction of the depth at which the sediment particles are first mobilized by the waves, D_m ($D_c = f_c D_m$, where the parameter f_c has to be calibrated). The residual value of ψ at deep water is controlled by the parameter α. The default α value is set to 0.46 so that $\psi(\infty) \sim f/2 = 0.01$. The decay rate of ψ is controlled by L_d and it is set to $L_d = 0.5\alpha D_c$. In the dry cells, $\psi(x)$ decays to 0 in the onshore direction as

$$\psi(x) = \exp\left(-\left(\frac{x - x_s}{X_{sz}}\right)^4\right), \tag{2.2.16}$$

where $x - x_s$ is the distance to the shoreline and the width of the swash zone X_{sz} controls the decay distance.

The third term in Eq. (2.2.8), $\vec{q_D}$, is an alongshore diffusive transport that represents the tendency of small bumps to be flattened by breaking waves and it tends to stabilize the numerical solution by diffusing the small-scale morphodynamic noise,

$$\vec{q_D} = -\gamma_D(\nabla z_b \cdot \hat{t})\hat{t}. \tag{2.2.17}$$

In all the applications of the present thesis, the alongshore diffusivity factor γ_D is equal to the cross-shore factor γ_N (Eq. 2.2.14) with the same shape function ψ (Eqs. 2.2.15-2.2.16).

2.2.4 Numerical implementation and boundary conditions

The bed evolution Eq. (2.2.6) is discretised using an explicit second order Adam-Bashforth scheme in time and a standard finite difference method in space (see van den Berg, 2012, for details). The values applied here for the grid size and the time step (of morphological evolution) are: $\Delta x = 6$ m, $\Delta y = 50$ m and Δt is varied depending on the application (e.g. in Chapter 3 $\Delta t = 0.001$ d). A ratio $\Delta x/\Delta y < 0.25$ for $\theta_0 < 89°$ is required to prevent that the waves exit the grid cells trough a lateral boundary (van den Berg *et al.*, 2012). Due to the slow changes in the bed level it is not necessary to compute the wave field at every time step. We found that updating the wave field each $\Delta t_w = 0.1$ d (i.e. every 100 steps of bed evolution) does not affect the morphological evolution, even under extreme conditions such as storms.

Offshore and lateral boundaries are open, i.e. the sediment in the domain is not necessarily constant. At the offshore boundary ($x = L_x$), a linear extrapolation of the inner bathymetry is assumed. The condition imposed at the onshore boundary ($x = 0$) is that the cross-shore sediment transport equals 0 ($q_x = 0$). At the lateral boundaries ($y = 0, L_y$), the profile is assumed to relax to the equilibrium profile, following the position of the global shoreline, with an exponential decay given by the decay distance λ,

$$\frac{\partial(z_b - z_{be})}{\partial y} = \pm\lambda^{-1}(z_b - z_{be}) \tag{2.2.18}$$

where z_{be} is the bed level of the equilibrium profile. Once the bathymetry outside the boundaries is imposed, the alongshore, normal, and diffusive transports are computed as in any other point. In the previous model version, only the alongshore transport was computed at the lateral boundaries. This caused problems when a shoreline sand wave train crossed the lateral boundaries.

2.2.5 Application 1: comparison with the previous model version

The present model version is compared with the previous one to ensure that the changes are implemented correctly. Also, this test is necessary to ensure that the model overcomes the limitation of the 13°-angle shoreline deviation and the previous problems in the lateral boundaries. The former is crucial for the application to the ZandMotor in Chapter 3.

Table 2.2.1: Default parameter setting of the Q2Dmorfo model trougout this thesis unless stated otherwise.

Symbol	Paramater	Value
γ_b	breaking ratio coefficient	0.5
ν_N	cross-shore diffusivity coefficient	0.05
ν_D	alongshore diffusivity coefficient	0.05
Δx	cross-shore grid size	6 m
Δy	alongshore grid size	50 m
Δt	time step	0.01 d
D_c	depth of closure	7 m

Model setup

A default experiment is defined in order to compare the results of the previous model version van den Berg *et al.* (2012) and those of the present version. The parameter setting can be seen in Table 2.2.1. The size of the simulation domain is $L_x = 1.8$ km by $L_y = 30$ km with 600 m of dry beach. The bathymetry is constructed with a modified Dean profile, the value b in Eq. (2.2.1) is such that a 10-m depth is found at 700-m offshore. For the initial bathymetry, a Gaussian-shaped beach nourishment (i.e. shoreline perturbation) with a cross-shore width of 25 m and an alongshore width of 2 km is placed at $y = 3$ km. For the wave forcing, constant conditions are imposed at the offshore boundary with $H_s = 1.4$ m, $T_p = 6$ s, and $\theta = 60°$. Finally, although the present model version computes the depth of closure directly from the wave conditions, for this test a D_c of 7 m is imposed to be consistent with the previous version.

Shoreline evolution

At the beginning both simulations evolve similarly (Fig. 2.2.4). After 75 days, the beach nourishment decays from a 25-m amplitude to an 18-m amplitude, exhibiting erosion down drift (of the nourishment) in both model runs. After 5 years, a sand wave train develops with a wavelength of about 3 km. The first two crests are located almost in the same position but the third and fourth develop faster in the previous model version. Remarkably, the present version computes smoother shorelines. The shoreline computed with the previous version shows short scale variations (see dashed red line at $y = 3000$ m in Fig. 2.2.4). This numerical noise could be the reason behind the faster development of the third and fourth crests.

For further analysis, the first five bumps are analysed individually. Each crest location is found by the most offshore shoreline point of each bump. The x-position of the crest with respect to the mean shoreline defines the amplitude A of each bump and the y-position defines the spacing between consecutive crests. The migration celerity can be inferred from the slope of the y-position. The results are shown in Fig. 2.2.5. The previous model crashes

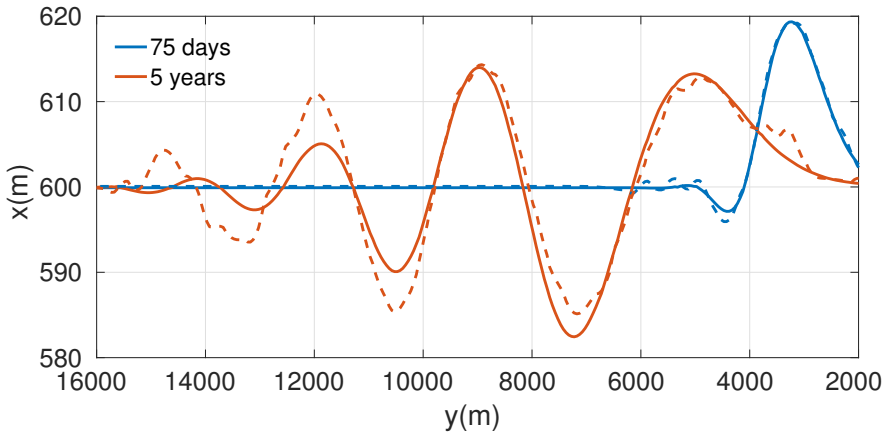

Figure 2.2.4: Shorelines simulated by the present model verion (solid lines) and the previous model version (dashed lines).

after seventeen years of simulation reaching a maximum amplitude of 162 m. This is not related to the 13-degree limitation. The shoreline erodes at an unrealistic rate when the sand wave is passing trough the lateral boundary, once the shoreline reaches the onshore boundary the model crashes. This is because the previous model version did not included diffusive transport in the lateral boundaries. The present model version includes diffusive transport at the lateral boundaries and allows for a longer simulation time. After twenty-five years a maximum amplitude achieved is 340 m at this point the valley of that bump reaches the onshore boundary. Only the third, fourth and fifth bump can be considered fully self-organized since the second bump is largely influenced by the initial perturbation (see the amplitudes in the middle panel of Fig. 2.2.5). Notice that in the previous model version the amplitudes of the considered self-organized features is almost the same after 15 yr while this never occurs in the new model version. Also, the spacing (wavelength) of the crests found in both models tends to increase since the migration celerity is larger for the newer bumps (see the bottom panels).

In general, the location-of-the-crest curves show small scale variability when using the previous model version due to small-scale instabilities in the shoreline related to the implementation of the sediment transport exchange between the dry beach and wet beach (see left-bottom panel in Fig. 2.2.5). In contrast, the shoreline computed with the new model version evolves smoothly. The other important difference between the models is the behaviour of the third, fourth and fifth bumps (the ones considered fully self-organized). After twelve years their amplitude is practically the same in the previous model version while in the new model version the amplitude is never the same, even though the model runs for eight more years. Finally, the final amplitudes are two times larger than those in the previous model version. The results of this application confirm the suitability of the changes included in the new version of the model.

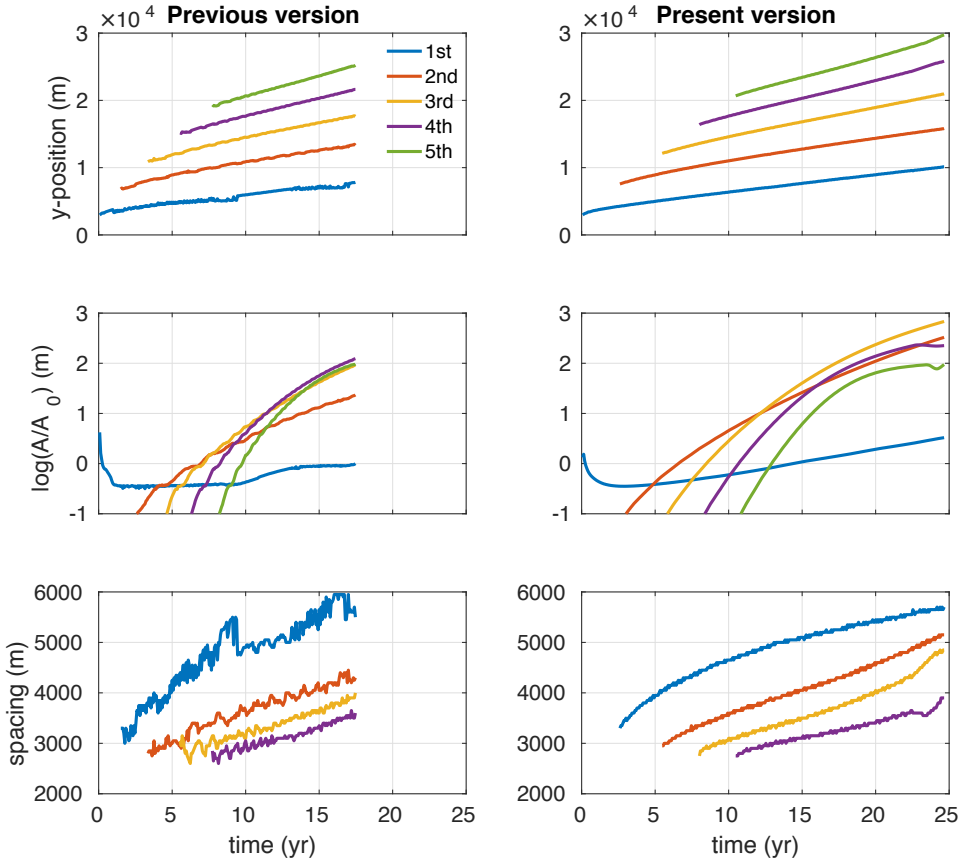

Figure 2.2.5: Crest locations (top panels). Logarithm of the amplitude normalized with the amplitude of the initial perturbation (middle panels). Spacing between crests (bottom panels, e.g, blue line is the spacing between the first bump and the second bump) corresponding to the previous model version (left panels) and to the present model version (right panels).

2.2.6 Application 2: sea-level rise as a cause of beach erosion

The sea-level rise related to climate change is a global concern and is expected to have an important effect on the future shape of the coasts. The most direct impact of a higher sea-level is the retreat of the coast. Normally, this is assessed with the Bruun theory, better known as the Bruun rule after Schwartz (1984). In the present thesis, the Q2Dmorfo model has been modified to handle sea-level variations. Here, the Q2Dmorfo model is compared with the prediction of the Bruun theory in a highly idealized scenario to ensure the correct variable sea-level implementation.

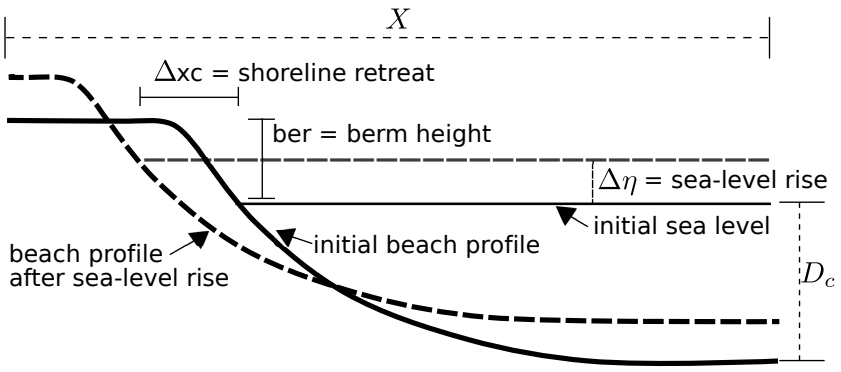

Figure 2.2.6: Bruun rule sketch.

Bruun rule

The Bruun rule is the most widely used method for determining shoreline response to sea level rise. It assumes the concept of an equilibrium profile for which the active portion (until the depth of closure) rises with rising sea level. The sand required to raise the profile is transported from the dry beach and is equal in volume to the material deposited on the near-shore bottom causing shoreline retreat (erosion). According to it the shoreline retreat follows

$$\Delta x_c = -(\Delta\eta \frac{X}{ber + D_c}), \tag{2.2.19}$$

where X is the distance from the active berm to D_c, $\Delta\eta$ is the sea level rise, and ber is the berm height (Fig. 2.2.6).

Model setup and shoreline response

The model setup is the same as in the previous subsection with a berm height of 1 m but without any type of perturbation (a rectilinear shoreline). A sea-level rise rate of 1 m/yr is imposed during the first year. After, this sea level of 1 m is conserved during the second year. For the present tests the sea level, η, is variable and the wave incidence is shore normal. Elsewhere in this thesis η is set to 0.

Preliminary tests showed that sediment infiltrates into the domain trough the lateral boundaries (i.e. the sediment was not conserved). This problem does not show up with constant sea level. The wrong assumption was that the shoreline position outside the domain (far away) is located at the initial shoreline position and this does not hold under sea-level rise conditions. Another test assuming that the shoreline position outside the domain follows

the Bruun rule prediction did not work either. The reason is that the modelled shoreline inside the domain takes some time to reach the retreat predicted by the Bruun rule whilst the lateral boundary condition is applied instantaneously. This time lag also caused artificial lateral sediment fluxes. Of course, the Bruun rule can be applied only if the alongshore-transport gradients are not important. Hence, for this test the lateral boundaries have been closed, that is $q_y(j = 0, j = m) = 0$.

After these modifications, the model obtains a beach profile that has a berm width similar to the swash zone width of X_{zs} =30 m (blue lines in Fig. 2.2.7). The retreat is stabilized at around 70 m while the Bruun rule estimation is of 50 m (40% model overestimation). The reason for this mismatch is that the whole simulated beach profile does not follow the shift in the dry area. The berm is different from the equilibrium one and the active depth is a little bit larger than the depth of closure.

The model can be forced to better reproduce the Bruun rule. To this end two model setup configurations are tested: i) using a large swash zone width (X_{zs}) to force sediment transport in the whole dry beach and keeping the D_c of 7 m, and ii) the same but using a D_c of 20 m to force a faster response of the deep active area of the beach profile (closing the offshore boundary, $q_x(i = n) = 0$). The justification of using an unrealistic large swash zone width is to take into account also the wind-driven sand transport and the high setup during storms. In the first test, the Bruun rule estimates a shoreline retreat of 145 m while the model stabilizes at 120 m (18% model under estimation). In the latter case, the Bruun rule estimates a shoreline retreat of 114 m while the model stabilizes at 112 m (2% model under estimation).

The model is able to reproduce the Bruun rule only in a very idealized case: by forcing the whole model domain to be active and by closing the lateral and offshore boundaries. Furthermore, although the Bruun rule is widely used, these simple simulations show that the beach response to sea-level rise is complicated and it can vary importantly depending on the response of the dry beach and the actual depth of closure. This agrees with the recommendation of the Scientific Committee on Ocean Research, Working Group (1991) to use the Bruun rule only for order-of-magnitude projections of shoreline recession.

2.3 1Dmorfo model

2.3.1 Governing equations

The same Cartesian coordinate system of the Q2Dmorfo model is assumed, with x in the cross-shore direction, y in the alongshore direction and z along the vertical. The model is based on the one-line sediment conservation formulation (also explained in Chapter 1)

$$\frac{\partial x_s}{\partial t} = -\frac{1}{\bar{D}} \frac{\partial Q}{\partial y}, \tag{2.3.20}$$

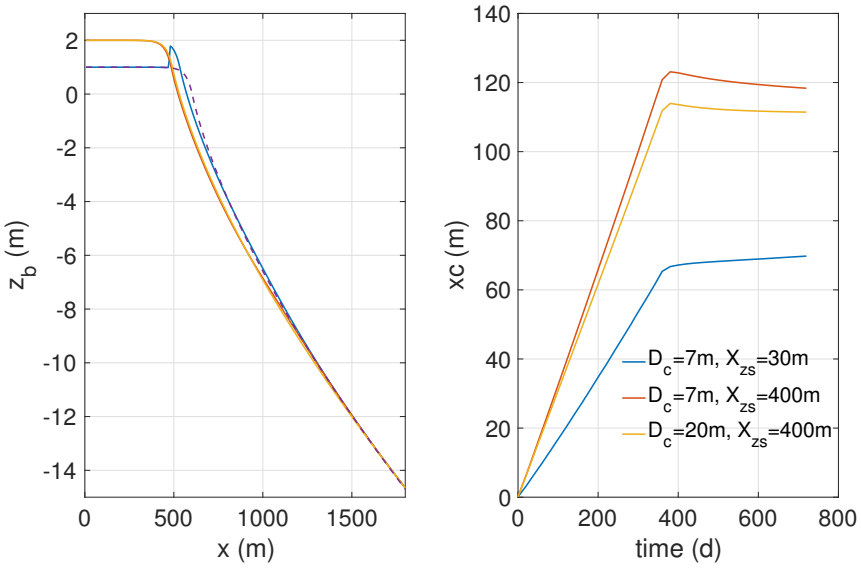

Figure 2.2.7: Initial beach profile (dashed line) and beach profiles after 2 years of simulation (left) and the shoreline retreat xc troughout time (right).

where $\bar{D}$ is the averaged active depth of the profile, and alongshore sediment transport rate, Q, is computed with the CERC equation (Eq. 2.2.9) and requires the computation of $H_b(y,t)$ and $\alpha_b(y,t)$.

The wave transformation considers that the bathymetric perturbations related to the coastline have a finite offshore extension and takes into account curvilinear depth contours. This is achieved by using the dispersion equation, the conservation of the wave front equation, and the wave energy equation (Eqs. 2.2.3-2.2.5). The model is forced uniformly offshore ($x = x_\infty$) with $H(x_\infty, y, t) = H_\infty(t)$ and $\theta(x_\infty, y, t) = \theta_\infty(t)$.

2.3.2 Basic reference state

The linear stability analysis requires a basic reference state, i.e. a state where the shoreline undulations are absent. Given an alongshore uniform topography $D = D_0(x)$ with $D_0(0) = 0$ and given an uniform offshore wave input, a steady and alongshore uniform solution for the wave field is found. The wave number $k_0(x)$ is directly computed from Eq. (2.2.3). The uniform topography allows for Eq. (2.2.4) to be cast into the Snell law

$$\frac{d}{dx}(k_0 \sin(\theta_0)) = 0 \tag{2.3.21}$$

and Eq. (2.2.5) gives

$$\frac{d}{dx}(c_{g_0}\cos(\theta_0){H_0}^2) = 0, \tag{2.3.22}$$

from where the wave incidence angle, $\theta_0(x)$, and wave height, $H_0(x)$, are found. The uniform wave field means that H_b and θ_b are alongshore uniform, therefore also the sediment transport rate Q is uniform. This immediately gives the next solution hereinafter considered the basic reference state

$$x_s = 0, k = k_0(x), \theta = \theta_0(x), H = H_0(x). \tag{2.3.23}$$

with the position of the breaker line given by $H_0(x_b^0) = \gamma_b D_0(x_b^0)$.

2.3.3 Perturbed dynamics

Now a perturbed state is considered by imposing an infinitesimal-amplitude undulation on an initially rectilinear shoreline defined as:

$$x_s(y,t) = \frac{A}{2}e^{\sigma t + iKy} + c.c. \tag{2.3.24}$$

where A is the amplitude, K is the shoreline perturbation wave number ($\lambda = 2\pi/K$) and $\sigma = \sigma_r + i\sigma_i$ is the complex growth rate. The expression of the shoreline perturbation is expressed in Fourier modes (Eq. 2.3.24) for convenience. The model aims at providing σ_r for a given K, from which the characteristic growth time ${\sigma_r}^{-1}$ and the migration celerity $V = \sigma_r/K$ can be computed. A positive growth rate σ_r means that the shoreline perturbation of the corresponding wavelength λ grows.

Regarding the unperturbed state, the main inputs of the model are the cross-shore equilibrium beach profile, $z_b(x) = -D_0(x)$, and the given wave parameters offshore, i.e. significant wave height, peak period and angle. Regarding the topographic perturbation $h(x,y,t)$, the main inputs are its alongshore wavelength, λ, its cross-shore shape function, $g(x)$ (which is link between the shoreline and the bathymetry is discussed in depth in the next section), and the depth of its offshore reach, D_c. Thus, the perturbed bathymetry associated with the sand wave defined in Eq. (2.3.24) is given by

$$D(x,y,t) = D_0(x) - h(x,y,t) = D_0(x) - \beta_s g(x) x_s(y,t) \tag{2.3.25}$$

To compute the growth rate (σ), Eq. (2.3.24) is inserted into the one-line sediment conservation equation (Eq. 2.3.20). The effect of the constant μ used in Q has an effect only

on the time scale, but the sign of the growth rate is insensitive to the magnitude of this parameter.

Computing the left hand side of Eq. (2.3.20) is straightforward from Eq. (2.3.24), but estimating the right hand side requires first the computation of the perturbed wave field defined by

$$\begin{aligned} k &= k_0(x) + \hat{k}(x)' e^{\sigma t + iKy} + c.c. \\ \theta &= \theta_0(x) + \hat{\theta}(x)' e^{\sigma t + iKy} + c.c. \\ H &= H_0(x) + \hat{H}(x)' e^{\sigma t + iKy} + c.c. \end{aligned} \tag{2.3.26}$$

The perturbed wave number can be computed from the linearised dispersion relation (Eq. 2.2.3)

$$\frac{\hat{k}'}{k_0} = \frac{2p}{2p + \sinh(2p)} \frac{\hat{h}}{D_0} \tag{2.3.27}$$

where $p = k_0 D_0$. The linearised eikonal equation (Eq. 2.2.4) is

$$\frac{dS}{dx} - iK(\tan\theta_0)S = -i\frac{K}{\cos\theta_0}\hat{k}' \tag{2.3.28}$$

where $S(x) = k_o\hat{\theta}'\cos\theta_0 + \hat{k}'\sin\theta_0$ is proportional to the phase $\Phi = -(i/K)S$. This can be solved numerically as an initial value problem with $S(x_\infty) = 0$ from offshore up to the coastline. Once $\theta(x)'$ is known, the linearized wave energy equation (Eq. 2.2.5)

$$\frac{d\Psi}{dx} - iK(\tan\theta_0)\Psi = i\frac{Kc_g H_0^2}{\cos\theta_0}\hat{\theta}' \tag{2.3.29}$$

can also be solved as an initial value problem like Eq. (2.3.28), where $\Psi(x) = 2c_g H_0 \hat{H}'\cos\theta_0 + \hat{c_g}' H_0^2 \cos\theta_0 - c_g H_0^2 \hat{\theta}' \sin\theta_0$.

Once the perturbed wave transformation is known, the wave variables at the perturbed breaking line can be evaluated. The perturbed breaking condition $H(x_b^0 + x_b') = \gamma_b D(x_b^0 + x_b')$ allows to determine the perturbed breaking line

$$x_b' = \frac{H'(x_b^0, y, t) + \gamma_b h(x_b^0, y, t)}{\gamma_b \frac{dD_0}{dx}(x_b^0) - \frac{dH_0}{dx}(x_b^0)} \tag{2.3.30}$$

The perturbed wave breaking variables

$$\theta'_b(y,t) = \theta(x_b^0 + x'_b, y, t) - \theta_0(x_b^0))$$
$$H'_b(y,t) = H(x_b^0 + x'_b, y, t) - H_0(x_b^0)) \tag{2.3.31}$$

are computed as

$$\theta'_b = \theta'(x_b^0, y, t) + \frac{d\theta_0}{dx}(x_b^0)x'_b$$
$$H'_b = H'(x_b^0, y, t) + \frac{dH_0}{dx}(x_b^0)x'_b \tag{2.3.32}$$

Using the linearised relationship

$$\alpha_b = \theta_b - \phi \simeq \theta_b - \frac{\partial x_s}{\partial y} \tag{2.3.33}$$

together with the linearisation of Eqs. (2.2.9)-(2.3.20), the morphodynamic governing equation becomes

$$\frac{\partial x_s}{\partial t} = \frac{2\mu \left(H_b^0\right)^{5/2}}{\bar{D}} \left(\left(\frac{\partial^2 x_s}{\partial y^2} - \frac{\partial \theta'_b}{\partial y} \right) \cos\left(2\theta_b^0\right) - \frac{5}{4H_b^0} \frac{\partial H'_b}{\partial y} \sin\left(2\theta_b^0\right) \right) \tag{2.3.34}$$

Finally, by inserting the perturbed expressions in the perturbed governing equation (Eq. 2.3.34, the complex growth rate σ can be computed as

$$\sigma = -2K \frac{\mu}{\bar{D}} \left(H_b^0\right)^{5/2} \left(\left(K + i \frac{2\hat{\theta}'_b}{A} \right) \cos\left(2\theta_b^0\right) + \frac{5i\hat{H}'_b}{2AH_b^0} \sin\left(2\theta_b^0\right) \right). \tag{2.3.35}$$

The real part of σ indicates the rate at which the perturbation will either grow or decay

$$\epsilon(K) = -\frac{\sigma_r(K)}{K^2}, \tag{2.3.36}$$

and a wavelength-dependent celerity can be defined from the imaginary part of σ

$$V(K) = -\frac{\sigma_i(K)}{K}. \tag{2.3.37}$$

2.3.4 Bathymetric perturbation function

The feedback between the morphology and the wave field dictates the beach response. In the morphodynamic models where the coastline evolves as a result of the changes in bathymetry driven by wave-induced sediment transport, such as the Q2Dmorfo model, the dynamics of the shoreline and the bathymetry are linked in a natural way (van den Berg *et al.*, 2012). However, in models based on the one-line concept such as the 1Dmorfo model, a link must be explicitly defined between shoreline and bathymetric perturbations. This link could be, in principle, defined from observations. However, given the lack of detailed observations of shoreline sand waves, such information is not available nowadays. Hence, the link must be inferred from physical principles. Considering that sand waves evolve at large time scales O(1 – 10 yr) in comparison with the short-term event scale of storms, the assumption of a bathymetric perturbation corresponding to a cross-shore shift of the equilibrium profile (following the shoreline displacement) has been used in the past by Ashton *et al.* (2001). Some studies assumed this profile shift but imposing a zero perturbation beyond the closure depth D_c (Falqués & Calvete, 2005; Kaergaard & Fredsoe, 2013*a*). Falqués & Calvete (2005) also considered a perturbation in the bed level which could decrease exponentially or linearly from a maximum value at the shoreline up to 0 at D_c. So, the shape perturbations used in the existing studies can be divided in two classes: type $P1$, based on profile shift assumptions, and type $P2$, based on a prescribed decay of the bed level perturbation.

Here, the representative perturbations

$$P1 : g(x) = \frac{1}{\beta_s}\frac{\partial D_0}{\partial x} \tag{2.3.38}$$

and

$$P2 : g(x) = 1 - \frac{x}{x_c} \tag{2.3.39}$$

are examined, where x_c is the cross-shore distance at which D_c is found, after which the perturbation is forced to 0, $g(x > x_c) = 0$. By inserting the shape function $P1$ in Eq. (2.3.25) and considering Eq (2.3.24), it is readily seen that it corresponds to horizontally shifting the profile by the same amount as the shoreline displacement (blue and red lines in Fig. 2.3.8b). The shape function $P2$ is based on a linear decay of the bed level perturbation (yellow line in Fig.2.3.8b) which is a limit of the exponential perturbation (when the decay distance is very large) used by Falqués & Calvete (2005).

The perturbation shapes can have serious implications in the perturbed bathymetric contours. For a high gradient profile ($D1$, see Fig. 2.3.8a), the bathymetric contours perturbed with $P1$ and with $P2$ are very similar until 10-m depth (Fig. 2.3.8c). In contrast, for a low gradient profile ($D2$, see Fig. 2.3.8a) the perturbed contours differ substantially. Notoriously, the contours perturbed with $P2$ reach a maximum at a certain distance from the coast at $D \approx 2$ m, and decrease to 0 at $D \approx 6$ m (Fig. 2.3.8d).

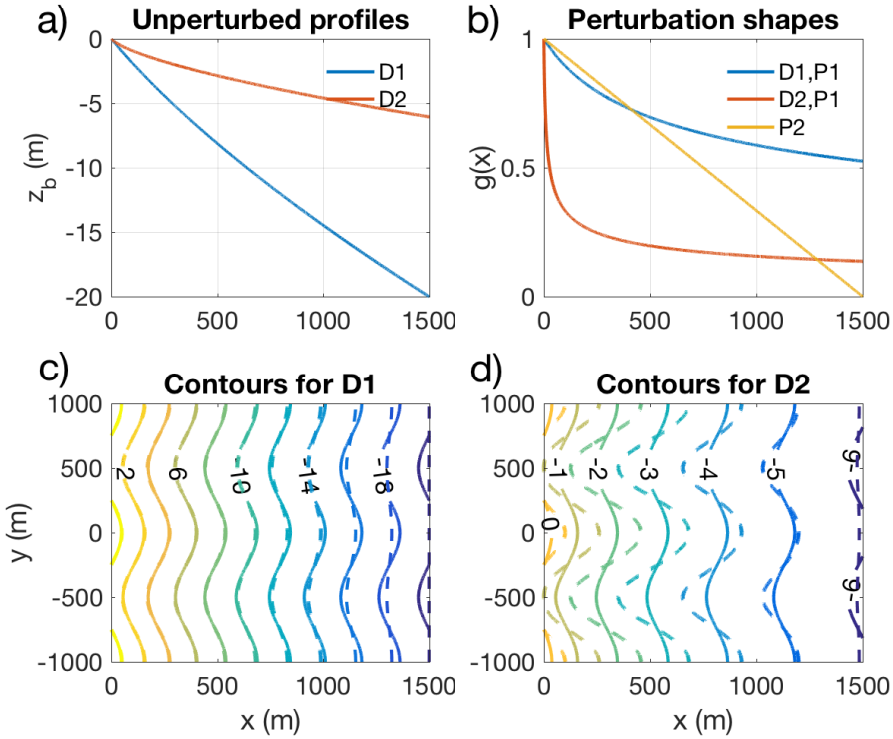

Figure 2.3.8: a) Modified Dean profiles using $b = 0.19$ m$^{1/3}$ and $b = 0.047$ m$^{1/3}$, with $\beta_s = 0.02$ for both profiles. b) Shape $g(x)$ of the perturbations $P1$ (blue line for the high bathymetric gradient profile $D1$ and red line for the low bathymetric gradient profile $D2$) and $P2$ (yellow line for both profiles). The lower panels show the depth contours with a perturbation $\lambda = 1$ km using $P1$ (solid lines) and $P2$ (dashed lines), corresponding to the profile $D1$ (c) and to the profile $D2$ (d).

2.3.5 Application 1: role of the bathymetric perturbation

The relative cross-shore amplitude of the depth contours with respect to the amplitude of the shoreline, constant for all contours for $P1$ and variable for every contour when using $P2$, strongly influences the wave transformation. Thereby, the alongshore sediment transport patterns and the resulting growth rate (positive in case of shoreline instability, negative in case of shoreline stability) also depends a lot on the bathymetric perturbation. The main purpose of this first model application is to illustrate this dependency by showing the growth rate curves (perturbation wavelength vs growth rate) for each of the perturbed bathymetries seen in Fig. 2.3.8. Since this model is applied to real conditions in Chapter 5, it is important to first understand the role of the bathymetric perturbations. In particular, its association to the high-angle wave instability mechanism or to the low-angle wave instability mechanism must be investigated. The objective is not to perform a systematic study but to

do a qualitative exemplification of the role played by the bathymetric perturbation on the instability mechanisms. To this end, only a low-gradient profile and a high-gradient profile are used to create four general perturbed states (following the profile shift perturbation $P1$ and the linear bed-level decay of the perturbation $P2$, shown in Fig. 2.3.8). Here, the wavelength of the perturbation range from $\lambda = [100\text{ m} - 30\text{ km}]$. Finally, the growth rate of these perturbed states is computed for three wave conditions: almost normal waves ($H = 1$ m, $T = 1$ s, $\theta = 5°$), oblique waves ($H = 1$ m, $T = 1$ s, $\theta = 45°$), and very oblique waves ($H = 1$ m, $T = 1$ s, $\theta = 65°$).

Given that the aim is to explain the qualitative behaviour of the growth rate curves rather than its quantitative behaviour, σ_r is normalized as

$$\sigma_{ref} = \max[\ |\min(\sigma_r)| * (-sign\,(\max\,(\sigma_r)))\ \ ,\ \ \max(\sigma_r)\ ]. \tag{2.3.40}$$

When an instability occurs, the curve σ_r/σ_{ref} has positive values and the preferred wavelength is where $\sigma_r(\lambda)/\sigma_{ref} = 1$. For the oblique wave condition ($\theta = 45°$), the predicted curves show the expected behaviour of HAWI theory (i.e. a growth rate curve with a single maximum value at a certain wavelength, see Fig. 2.3.9b). The damping of short wavelengths in HAWI is controlled by the focusing/defocusing of wave energy induced by the undulating contours (van den Berg *et al.*, 2014). For relatively long wavelengths, in comparison with the offshore reach of the bathymetric perturbation, the focusing is always near the sand-wave crests (i.e. the prograding section) and the defocusing near the embayments. In this case, only one maximum is found at wavelengths $\lambda = 3, 12, 16, 24$ km. After that, the curve decays to 0 with a λ^{-2} factor. For the very oblique wave condition ($\theta = 65°$, Fig. 2.3.9c), the behaviour of the curves is similar except for the combination $D2$-$P1$ where three local maxima can be seen. This behaviour was also found by Uguccioni *et al.* (2006). The reason is that for very oblique waves, the rays can cross the shoals corresponding to several crests instead of only one. So, the focusing/defocusing becomes more complex with the result that the energy focal point is not necessarily located at the crests. For this reason, the instability curve is sensitive to small changes in the wavelength of the perturbation. Low-gradient profiles are the most prone to this phenomenon. Nevertheless, for the bathymetry $D2$-$P2$ only one maxima occurs. The reason may be related to the fact that the more perturbed offshore contours produce larger refraction and it becomes harder for the rays to cross more than one shoal. Indeed, by forcing the model with $\theta = 85°$ several maxima can be found for both perturbations and for both profiles (not shown here).

When diffusion is predicted for every wavelength, the curve σ_r/σ_{ref} has only negative values. In this case, the normalization of the curve is done with the lowest σ_r value (following Eq. 2.3.40). The diffusion of the shorter-perturbation wavelengths is several orders larger than that of the larger-perturbation wavelengths. For this reason, the curves $D1$-$P1$, $D1$-$P2$, and $D2$-$P1$ seem to be a straight line touching 0 while in fact they approach to 0 (Fig. 2.3.9a). This occurs only for shore-normal waves ($\theta = 5°$) except for the special case $D2, P2$. In fact, this instability mechanism is different from the HAWI one. Idier *et al.* (2011) found that under certain conditions a critical high-wave-angle threshold is not necessary for destabilization of the shoreline. This instability is now known as low-angle wave instability (LAWI, see Idier *et al.*, 2011). Idier *et al.* (2017) described two conditions for LAWI to occur. The first is that the cross-shore amplitude of the undulations in the bathymetry should be

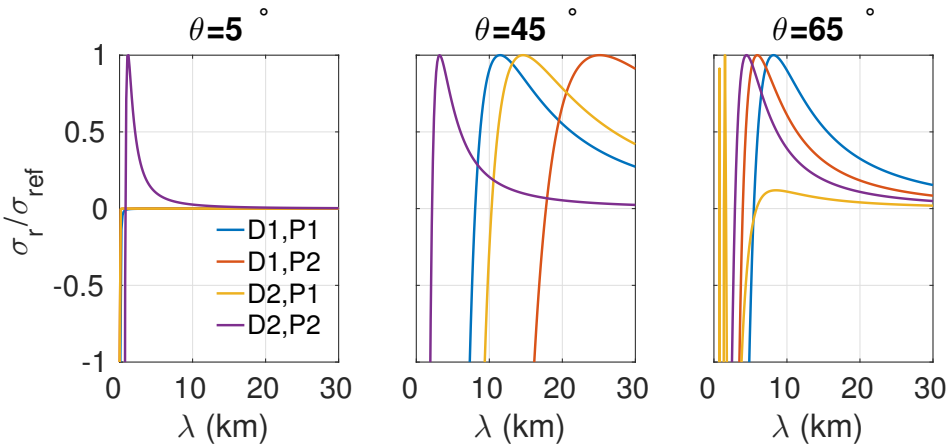

Figure 2.3.9: Growth rate curves normalized for the four bathymetries described in Fig. 2.3.8c-d. For wave incidence $\theta = [5°, 45°, 65°]$.

larger than the cross-shore amplitude of the undulation in the shoreline. The second is that the region where this occurs has to be located offshore the surf zone. So, it is dependent on the wave conditions and the bathymetric perturbation. It can be seen that these conditions are met by $D2$-$P2$.

2.3.6 Application 2: 1Dmorfo comparison with Q2Dmorfo in Denmark

Srd. Holmsland Tange, located in the west coast of Denmark, has been used to test the theory for the formation of KSSW (Kaergaard & Fredsoe, 2013*a*; Falqués *et al.*, 2017; Idier *et al.*, 2017) after Kaergaard *et al.* (2012) described in detail the observed shoreline undulations and the associated bathymetric contours. The present application has two purposes: i) to investigate the capacity of the Q2Dmorfo model to describe these undulations by comparing the results in the linear regime (using the 1Dmorfo model) with those in the non-linear regime (using the Q2Dmorfo model) and ii) to substantiate with this site the existence in nature of the counter-intuitive $P2$ bathymetric perturbation.

Here, the KSSW observed in Denmark are described and the discrepancies between two previous linear model findings are explained (Kaergaard & Fredsoe, 2013*b*; Falqués *et al.*, 2017). After that, a comparison between the 1Dmorfo model and the Q2Dmorfo model is done. For this the 1Dmorfo model is applied to this site with perturbations $P1$ or $P2$ (i.e. two different cross-shore links are used), but the cross-shore link in the Q2Dmorfo model is a result of its cross-shore transport formulation. Since the bathymetric shape perturbation cannot be imposed in the sediment transport formula of the Q2Dmorfo model, and in order to imitate the configuration of the 1Dmorfo model, the initial state of the former has been

constructed with the equilibrium profile plus a shoreline sand wave of small amplitude and a cross-shore shape following the perturbations $P1$ or $P2$. Then, the initial temporal evolution of the amplitude is used to compute the growth rate and compare it with the linear model. Finally, the consistence of the bathymetric perturbations in nature with $P2$ is discussed.

Site: Srd. Holmsland Tange

Kaergaard *et al.* (2012) described field measurements in Srd. Holmsland Tange (see Fig. 2.3.10a). Particularly, km-scale shoreline sand waves were reported with a wavelength $\lambda \simeq$ 5-6 km, an amplitude (cross-shore distance between the crest of a shoreline undulation and the adjacent embayment) of $\simeq$ 100 m, and a migration rate of 0.37 km/yr. Kaergaard *et al.* (2012) hypothesized that the undulations were correlated with the HAWI mechanism since an important amount of wave energy arrives with a very oblique wave incidence. This hypothesis was reinforced by the weak correlation between the offshore position of alongshore bars and the shoreline undulations. Later on, Kaergaard & Fredsoe (2013*b*) used the average wave conditions ($\theta = 42°$, $H_s = 1.8$ m, $T_p = 6.1$ s) measured 14-km offshore to model the shoreline undulations and assuming a D_c of 5-7 m. They found that these wave conditions would diffuse the undulations (negative growth rates). In order to find an unstable regime (i.e. positive growth rates), they forced the model with a wave angle of 55° (13° more than the measured average) and found a shoreline wavelength of 5-9 km. More recently, Falqués *et al.* (2017) modelled this same site and argued that a reasonable range for D_c is 9-13 m. Using both the averaged wave conditions and the real wave series, they examined the sensitivity to D_c. For the wave series, a $D_c = 11 - 15$ m was required to obtain the observed wavelength while for the constant wave conditions, a $D_c = 7.5-15$ m was required. The disagreement between the studies of Kaergaard & Fredsoe (2013*b*) and Falqués *et al.* (2017) is partly due to the different models and assumptions, e.g. the former used smaller depth of closures and took into account the directional spreading. Nevertheless, the key difference is related to the cross-shore link between the shoreline and the bathymetric contours. Kaergaard & Fredsoe (2013*b*) used a cross-shore shift ($P1$) and Falqués *et al.* (2017) used a linear decay of the bed-level perturbation ($P2$).

Comparison between 1Dmorfo and Q2Dmorfo

Here, the Srd. Homsland Tange site is modelled with the 1Dmorfo and the Q2Dmorfo models. Given that the main difference between previous works is related to the link between the shoreline and the bathymetry, two assumptions are examined: the cross-shore shift of the profile (perturbation $P1$) and the vertical linear decay of the perturbation from the shoreline to the depth of closure (perturbation $P2$). This is straightforward in the 1Dmorfo model. However, the cross-shore transport is fixed in the Q2Dmorfo model, which assumes that the beach profile tends to the equilibrium one, i.e. a cross-shore shift in the long-term. Since this can not be changed, only the initial bathymetries follow the perturbation $P1$ or the perturbation $P2$ in the Q2Dmorfo simulations. After a while, the Q2Dmorfo bathymetry will look like that corresponding to a $P1$ perturbation. Three wave conditions are used: $\theta = [30°, 42°, 60°]$, $H_s = 1.8$ m, $T_p = 6.1$ s. As unperturbed basic profile, the observed one is used (Fig. 2.3.10b) and a D_c of 12 m is assumed following the findings of

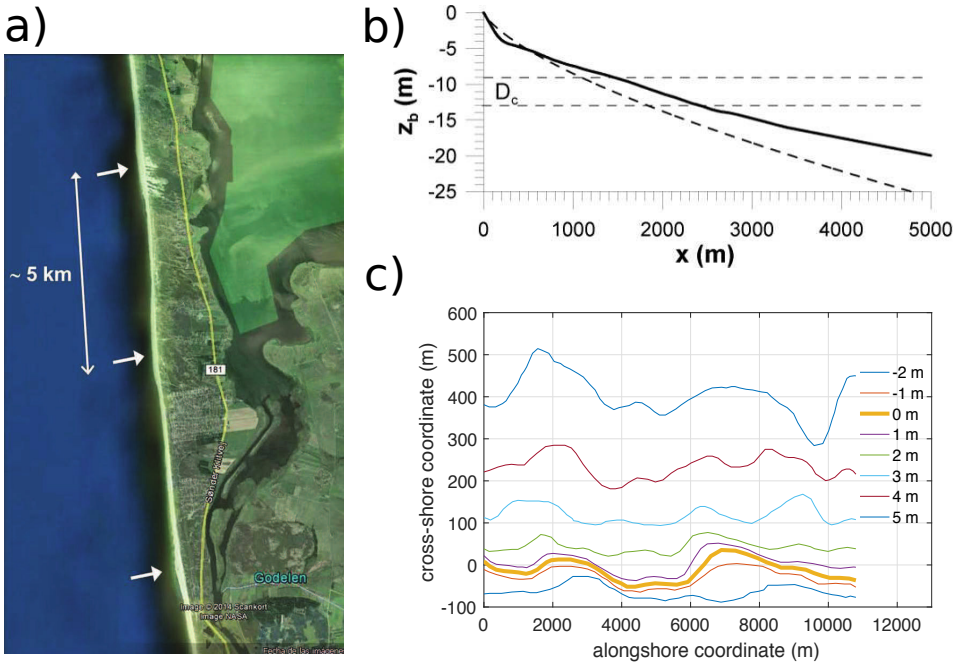

Figure 2.3.10: a) Satellite image of Srd. Holmsland Tange downloaded from Google Earth, b) Cross-shore profile digitized (solid line) from Kaergaard & Fredsoe (2013*b*) and its Dean-profile adjustment (dashed line), c) Depth contours digitized from Kaergaard *et al.* (2012).

Falqués *et al.* (2017). The 1Dmorfo model allows a quick computation of the growth rate for several wavelengths but the Q2Dmorfo requires larger computational effort. This is why the Q2Dmorfo simulations are done only for perturbations with wavelengths 2,4,6,8,10 km and until the first 100 d. The amplitude of the initial perturbations is of 6 m. Thus, the comparison is the closest possible by focusing the Q2Dmorfo model analysis to the initial evolution time and to small perturbation amplitudes, i.e. the assumptions of the 1Dmorfo model.

The growth rate σ_r of the shoreline undulations in the non-linear model is obtained following

$$A_2 = A_1 e^{\sigma_r * (t_2 - t_1)} \tag{2.3.41}$$

where A_1 is the initial amplitude and A_2 is the final amplitude. Two growth rates are computed: $\sigma_r(t_1 = 0$ d, $t_2 = 50$ d) (asterisks in Fig. 2.3.11) and $\sigma_r(t_1 = 50$ d, $t_2 = 100$ d) (circles in Fig. 2.3.11).

For $P1$, the growth rates computed with both models have similar behaviour and are within the same order of magnitude. Although no positive σ_r is observed (see left panels in

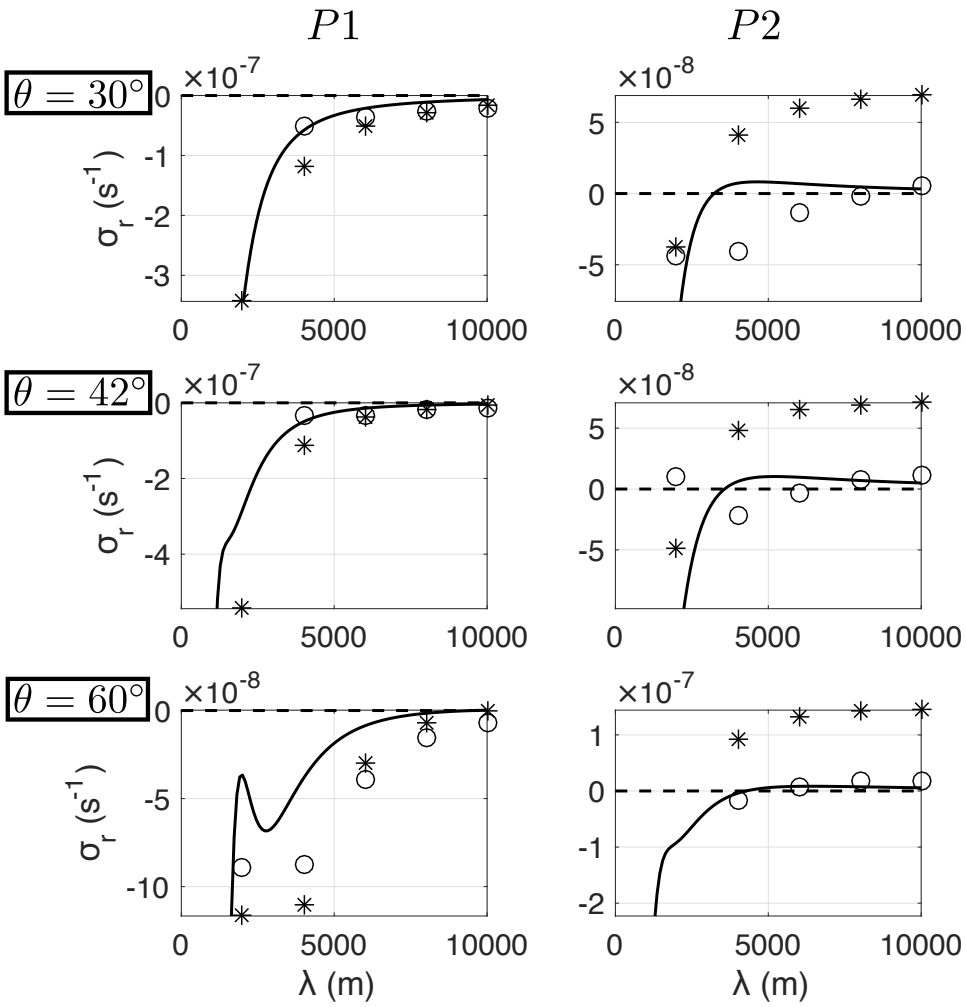

Figure 2.3.11: The growth rate computed with the 1Dmorfo model (solid line). The growth rate computed with the Q2Dmorfo model using $t1 = 0$ d - $t2 = 50$ d ($*$) and using $t1 = 50$ d - $t2 = 100$ d ($\circ$) The left/right panels correspond to the simulations with the perturbation $P1/P2$. The top/middle/bottom panels correspond to the simulations forcing the model with θ =30°/42°/60°.

Fig. 2.3.11), tests analysing longer wavelengths indicate a preferred 14-km wavelength with positive σ_r (not shown here) for $\theta = 60°$ and still negative σ_r for the other wave angles. These results do not agree with the observations, indicating that the perturbation $P1$ does not appear to work in this specific site. For $P2$, the growth rate predictions are clearly different not only between models but also between the growth rates computed at different times with the Q2Dmorfo model. This is because initially the cross-shore transport has a large influence given that the profiles are not in equilibrium. As a result, the amplitude

initially increases for any angle (see asterisks in Fig. 2.3.11) and later on exhibits smaller and even negative growth rates (see circles in Fig. 2.3.11). The similarity between the 1Dmorfo model and the Q2Dmorfo model using $\theta = 60^\circ$ is a coincidence, and occurs during the transition of the bathymetry from $P2$ to $P1$. So, the $P2$ results are consistent with the observations only for the 1Dmorfo model computations.

Using $P2$ the 1Dmorfo model predicts a preferred wavelength around 5 km which agrees with the observations at Srd. Holmsland Tange for the averaged wave conditions. The robustness of this wavelength is confirmed by the slight variations of the predicted wavelength (around 5 km) using different incident wave angles (see right panels in Fig. 2.3.11). The disagreement of the predictions using $P1$ and the good correlation of the results using $P2$ indicate that the low-angle wave instability mechanism is acting in Srd. Holmsland Tange. Regarding the counter-intuitive existence of the perturbation $P2$ in nature, it can be readily seen in Fig. 2.3.10c that the cross-shore amplitudes of the 4-m- and 5-m-depth contours are larger than the amplitude of the shoreline undulation. This is the essential characteristic of the P2-type perturbation. The fact that the Q2Dmorfo model cannot reproduce the LAWI mechanism is discussed in the next section.

2.4 Discussion and conclusions

An extension of the previous Q2Dmorfo model of van den Berg *et al.* (2012), which can model the dynamics of km-scale shoreline sand waves, has been presented. The main changes are the introduction of a "fuzzy shoreline algorithm" and the modification of the direction of the cross-shore sediment transport, which now points in the local cross-shore direction. As a result, the model satisfactorily describes the dynamics of sand waves at larger times and with larger amplitudes, compared to those described by van den Berg *et al.* (2012). The wavelengths are similar but the growth rates are smaller for the fully self-organized sand waves. The smaller growth rate is in better agreement with the linear stability model predictions by Falqués & Calvete (2005). Interestingly, the longer simulation time allows to observe a clearer tendency to growth saturation.

The sea-level rise implementation in the Q2Dmorfo model reproduces the Bruun rule prediction under specific conditions: i) a bathymetry in equilibrium, ii) normal wave incidence, iii) closed lateral boundaries (i.e. one-dimension dynamics), and iv) large values of X and D_c. There are two reasons for these constraints: i) the Bruun rule does not take into account alongshore sediment transport gradients and ii) the present lateral boundary conditions are not properly implemented for a shoreline dependent on variable sea level. Therefore, the model can now handle scenarios more complex than the Bruun rule but its use has to be limited to enclosed systems such as a pocket beach. The key element that allows to only model highly idealized conditions is the present lateral boundary condition of assuming that the shoreline position far away the domain follows the Bruun rule prediction. The Q2Dmorfo model takes some time to retreat and reach the Bruun rule prediction while the lateral boundary condition is applied instantaneously. This causes lateral sediment fluxes. An alternative not yet tested is to add a delay-time variable for the Bruun rule prediction. This variable could be computed by testing the model under one-dimension dynamics and comparing it with the Bruun rule prediction. This way, the lateral sediment

fluxes could be diminished. The reason for requiring large values of X and D_c to obtain a good comparison between the Bruun rule and the model is that such values activate the whole profile and accelerate the time to reach the equilibrium profile, i.e. the assumptions of the Bruun rule.

A linear stability model, the 1Dmorfo model, has also been presented focusing on the role of the bathymetric perturbations associated to the shoreline perturbation, i.e. the cross-shore link between the shoreline and the bathymetry. Particularly, two types have been discussed, the widely (and traditionally) used cross-shore shift of the profile, $P1$, and the linear bed-level decay of the perturbation, $P2$. The former is related to the high-angle wave instability mechanism (Falqués & Calvete, 2005) while the latter is related to the low-angle wave instability mechanism (Idier *et al.*, 2011). The analysis of the observations in Srd. Holsmland Tange show that the perturbation $P2$ exists in nature. Indeed, its essential characteristic is observed there (i.e. the cross-shore amplitude of the depth contours is larger than the one of the shoreline). Also, the 1Dmorfo prediction of that site, assuming a $P2$ perturbation, agrees with the wavelength of the shoreline undulations presented by Kaergaard *et al.* (2012).

The comparison between the 1Dmorfo and the Q2Dmorfo models show very good agreement when using $P1$. However, important differences occur when using $P2$. The cross-shore transport is fixed in the Q2Dmorfo model and cannot be changed as in the 1Dmorfo model. Therefore, the Q2Dmorfo simulations assume only an initial perturbation $P2$, which evolves in time towards a perturbation $P1$. The excess (lack) of sand in the profiles located in the crests (embayments) with respect to the defined equilibrium profile is transported to (from) the shoreline, resulting in accretion due to cross-shore transport. This is why the Q2Dmorfo model (as it is) cannot reproduce the low-angle wave instability mechanism. A plausible solution could be to define an alongshore-variable equilibrium profile as a function of two extreme profiles: one corresponding to the embayment and one corresponding to the crest. The local equilibrium profile would be interpolated according to the local shoreline position. This is a behaviour-based solution supported by the reasoning that the waves experienced by the profiles in the crest and the embayment are different due to refraction. A more promising solution is to define a process-based cross-shore transport, i.e. independent from an equilibrium profile. Either way, these solutions are out of scope the present thesis and are only described here as possible solutions to be tested in the future.

Chapter 3

Mega-nourishment modelling and model validation

3.1 Introduction

In The Netherlands, coastal protection is a high-level priority as reflected in its coastal policy of maintaining the coastline position at its 1990 position (de Ruig & Hillen, 1997). As a consequence, innovative large-scale solutions have been implemented such as the construction of a hook-shaped mega-nourishment, called Sand Engine (ZandMotor in Dutch, from now on referred to as ZM), in July 2011 (Stive *et al.*, 2013). The ZM is expected to diffuse mainly due to the alongshore transport, which acts as the main distributor of sand along the adjacent coast, and to feed a large beach stretch instead of local erosional hot spots only. The ZM consists of 17 Mm^3 of sand and affects depth contours until 8 m depth, driving the local profiles far away from their previous state (de Schipper *et al.*, 2016). Therefore, cross-shore diffusion is also expected. According to Stive *et al.* (2013) and de Schipper *et al.* (2014), the envisioned lifetime of the ZM is of the order of 15-20 yr.

At the Dutch coast, Ruessink & Jeuken (2002) analysed data of dune-foot position dating back to as early as 1850, detecting the presence of small amplitude SSW and discussed the HAWI mechanism as a possible explanation. Falqués (2006) made an analysis of the Dutch coast with a shoreline instability model, finding that with the present wave climate the shoreline was stable but that slightly increasing the percentage of obliquely incident waves the coast could become unstable. Moreover, van den Berg *et al.* (2011) studied the triggering of shoreline sand waves by nourishments. Even if a coastline is stable, its evolution can still be affected by the HAWI mechanism as it can cause a decrease in diffusivity and an alongshore migration of shoreline perturbations (van den Berg *et al.*, 2011).

This chapter is largely based on Arriaga *et al.* (2017): Arriaga, J., Rutten, J., Ribas, F., Ruessink, B. & Falqués, A. 2017 Modeling the longterm diffusion and feeding capability of a mega-nourishment. *Coast. Eng.* **121**, 1–13

In the present chapter, the Q2Dmorfo model (described in chapter 2.2) is used to investigate the evolution of the ZandMotor following two primary objectives: (i) to take advantage of the intense ZM monitoring to calibrate and validate the Q2Dmorfo model and (ii) to assess the long-term behaviour of the ZM, including its diffusion, migration, feeding capability to adjacent beaches and its potential to trigger SSW. First, the ZandMotor site is described, both the morphology and wave forcing. Afterwards, the Q2Dmorfo model is calibrated using the data one year after the hook connects to the beach. Subsequently, the model is validated with data after three years of evolution. Later, long-term simulations of thirty years (taking into account the validation period) are performed using historic-wave data extracted from a 32-m-depth buoy. Finally, a discussion focusing on the role of HAWI in the ZM evolution is presented.

3.2 Site description and model bathymetry

The ZM is a hook-shaped mega-nourishment of 17 M m^3, with an initial alongshore length of 2.4 km and an offshore extension of 1 km, constructed from March 2011 to July 2011 within the 17 km-long beach section (Delfland coast) bounded by the harbours of Scheveningen and Hoek van Holland (Fig. 3.2.1a). Furthermore, the design contained a small lake to prevent the freshwater lens in the dunes to migrate seaward (Stive *et al.*, 2013). Fig. 3.2.1b shows the massive quantity of sand, this picture was taken in January 2012 after the hook attached to the beach.

3.2.1 Waves and tides

The governing offshore wave climate has a yearly mean wave height (H_s) of about 1.3 m and a yearly mean wave period (T_p) of about 6 s. There is a clear seasonal variability: from November to January the mean wave height is 1.7 m and from April to August it is about 1 m (Wijnberg & Terwindt, 1995). Waves mainly approach the coast from the south-west-west and the north-north-west (Wijnberg & Kroon, 2002) (Fig. 3.2.1c). For this work, the significant wave height (H_s) peak period (T_p), and angle (θ_0) were extracted every 3 h from the Europlatform buoy located at 32 m depth ignoring the waves directed seaward (Fig. 3.2.1c). Since the offshore wave climate is rather alongshore uniform at the Dutch coast (Wijnberg & Terwindt, 1995) this buoy is representative of the local wave climate even though it is located to the west of the ZM. The waves are transformed from the buoy to the offshore model boundary using Snell law and energy conservation. The tide in the Delfland coast is semi-diurnal with a mean range of 1.7 m (Wijnberg & Terwindt, 1995).

3.2.2 Morphology

The sediment in this area has a median grain size of 250 μm (Wijnberg & Terwindt, 1995) and the median grain size of the ZM is 280 μm (de Schipper *et al.*, 2016). The equilibrium profile, required by the model (β_e in Eq. (2.2.13) and z_{be} in Eq. (2.2.18)), is extracted

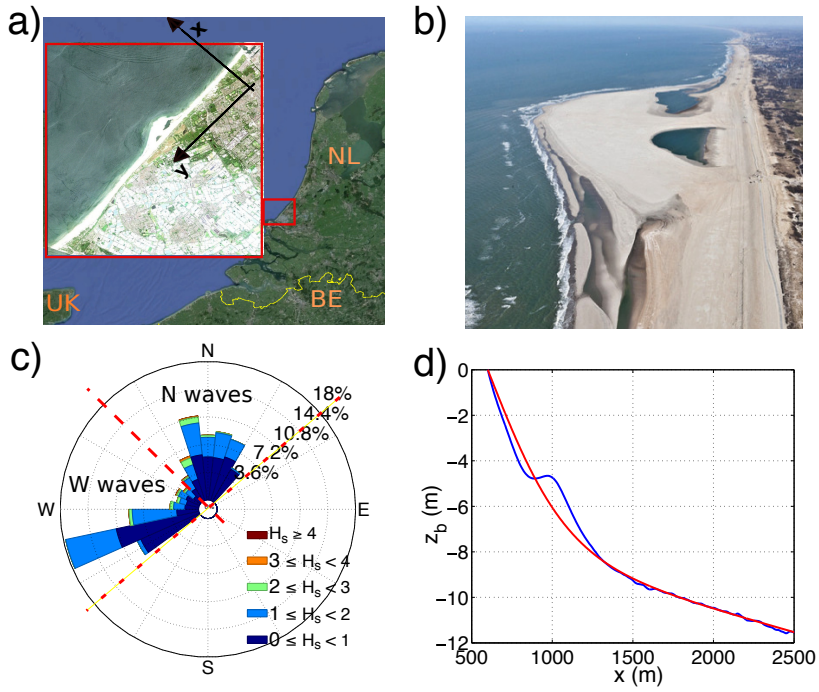

Figure 3.2.1: (a) ZandMotor location, with the model coordinate system, (b) ZM picture provided by Jantien Rutten, (c) directional distribution of H_s at the Europlatform buoy (32 m depth), and (d) time-and-space-averaged bed elevation, z_b, versus distance x in the ZM area (blue line) and the adjusted profile (red line) of Yu & Slinn (2003).

from the long-term JarKus data set by averaging the profiles spatially and temporally. The JarKus annual profiles usually start in the dune area and end at about 800 m seaward with 250 m alongshore spacing. Every 5 yr, coastal profiles are surveyed up to about 2500 m seaward with 1 km alongshore spacing. The alongshore spatial distance for the derivation of the averaged profile is of 10 km around the ZM, and the temporal period chosen is from 1990 to 2009 (de Ruig & Hillen, 1997). The equilibrium profile for the model is obtained from the averaged profile (Fig. 3.2.1d) by adjusting the Yu & Slinn (2003) profile equation (Eq. 2.2.2). Also, the sensitivity of the model to using different equilibrium beach profiles was analysed, (varying from an area 1 to 10 km around the ZM and from 5 to 40 yr before the ZM construction), and no appreciable changes were observed.

In the framework of the ZM project, bathymetric surveys were performed every month in the first year after the installation, and every two months in the subsequent years. The bathymetries extend 1.5 km offshore and 4.5 km alongshore. The grid resolution is 2 m and 25 m in the cross-shore and alongshore coordinates, respectively. The initial bathymetry for the model simulations corresponds to the survey of 17 January 2012 (Fig. 3.2.2a), once the initial hook-shape had connected to the adjacent beach (Fig. 3.2.2a), creating a second

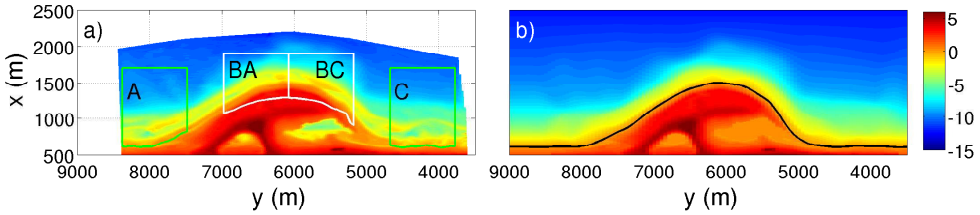

Figure 3.2.2: (a) Bathymetric survey from 17 January 2012 with volume control boxes and (b) input bathymetry of the model with the bars filtered out and the lagoons adjusted.

enclosed water body. The initial model bathymetry is made by combining bathymetric data from the intensively surveyed area of the ZM with the equilibrium profile extracted from the Jarkus data set for the remainder of the modelled domain. In the bathymetries of the ZM area, we filter out the bars using the volume approach (Kaergaard *et al.*, 2012) to meet the model assumption of a monotonic equilibrium profile. First, for each depth the bed level is integrated over a vertical range, the resulting volume is converted to distance from a fixed location on the beach, obtaining a clean profile with the volume conserved and without bars (see thick dashed line in Fig. 3.3.3). Second, the surveyed dry beach area is added, with the inner water bodies treated as 0.1 m high dry beach. Third, the contours in the model domain outside of the ZM area are constructed following the equilibrium profile assuming a straight shoreline (i.e. the overall position of the shoreline previous to the ZM construction). Finally, the bathymetry is interpolated from the overlapped contours (Fig. 3.2.2b).

3.3 Calibration and validation

3.3.1 Model calibration

The Q2Dmorfo model described in chapter 2.2 is calibrated with the ZM data (see chapter 3.2.2), starting with the measured bathymetry from 17 January 2012 (Fig. 3.2.2). The three most influential parameters are calibrated by comparing the modelled and the measured bathymetries after 400 d (to take seasonality into account), and by forcing the model with the wave data from the Europlatform buoy. The first parameter, μ, controls the magnitude of the alongshore sediment transport (Eq. 2.2.9), the second parameter, f_c, controls the depth where the cross-shore and diffusive transports (Eqs. 2.2.13 and 2.2.17) drop to ~ 0 (i.e. it controls the active depth for sediment transport), and the third parameter, ν controls the magnitude of the cross-shore and diffusive transports (i.e. it controls the relaxation time to equilibrium). In this contribution, the calibration process is simplified by using the same values for ν in both transport terms, diffusive and cross-shore, that is $\nu = \nu_N = \nu_D$, as in van den Berg *et al.* (2012). Similarly, the same value of f_c has been used for both transport terms. Thereby, $\gamma_D = \gamma_N$. The range of values used for the calibration are $\mu = [0.01; 0.04; 0.07; 0.10]\ m^{1/2}s^{-1}$, $\nu = [0.01; 0.03; 0.05]$ and $f_c = [0.05; 0.15; 0.25; 0.35; 0.45]$.

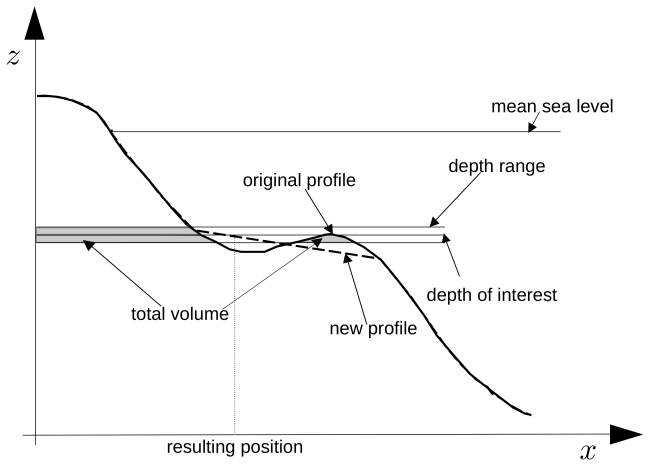

Figure 3.3.3: Sketch of the volume approach. Thick solid line corresponds to the original profile. Thick dashed line corresponds to the profile after filtering out the bar with the volume approach.

Larger μ values are not included because preliminary model simulations showed that they largely over-predicted the ZM diffusion. Also, the values for f_c and ν are chosen because they are physically meaningful and still prevent numerical instabilities. Too low values lead to the growth of small scale morphological noise and numerical instabilities. From observations, it is clear that a factor $f_c > 0.50$ is not plausible (e.g. using $f_c = 0.50$, the active depth would be 9.31 m for $H_{rms} = 1$ m and $T_p = 6$ s). On the other hand, if there are areas of significant alongshore sediment transport convergence and there is not enough capacity to redistribute it cross-shore, "unphysical" islands tend to grow and the simulations blow up. Finally, a very high ν value is equivalent to an unrealistic instantaneous shift of the profile as in the one-line models. This gives a constraint on the ratio μ/ν.

The model performance is evaluated with the root-mean-square skill score, $RMSSS = 1 - RMSE(Y,X)/RMSE(B,X)$, of the modelled contours (until 10 m depth). In the definition of the $RMSSS$, $RMSE$ stands for the root-mean-square error, X is a set of n measurements, $x_1, x_2, ..., x_n$, Y is a set of corresponding predictions, $y_1, y_2, ..., y_n$, and B is the prediction of no change (i.e. the initial survey), also called baseline prediction (Sutherland *et al.*, 2004). The contours of the bathymetric survey are extracted using the volume approach (Fig. 3.3.3). The root-mean-square errors are weighted over the depth contours with a coefficient of 0.9^D (D being the water depth) so that the coastline and shallow contours have more weight than deeper contours. Perfect agreement (i.e. $RMSE(Y,X) = 0$) gives a $RMSSS$ of 1. If the model prediction is further away from the measured condition than the baseline prediction, the $RMSSS$ becomes negative.

In general, after 400 d the $RMSSS$ improved with decreasing f_c (Fig. 3.3.4a). For $f_c = 0.05$ the simulations became unstable for $\mu \geq 0.04$ $m^{1/2}s^{-1}$ and low ν values, which

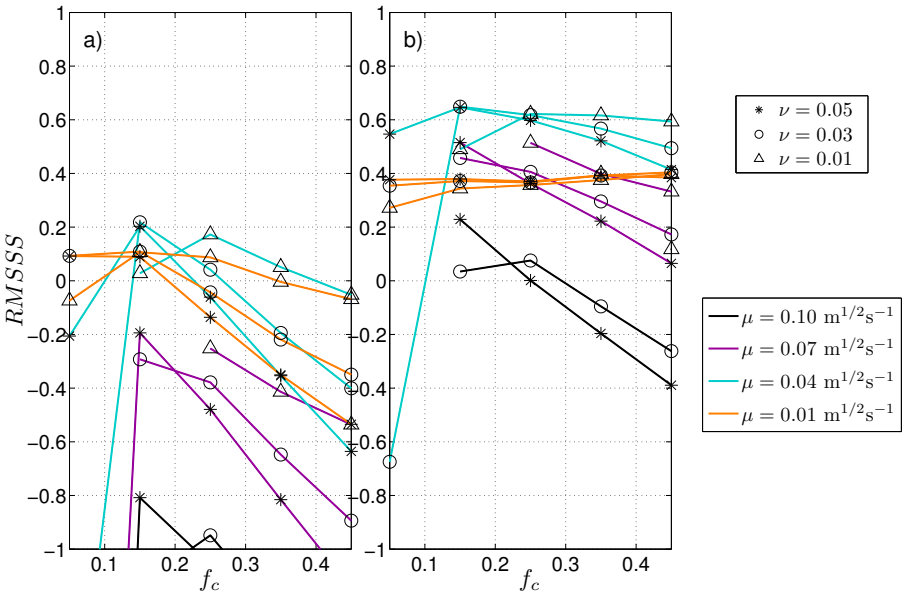

Figure 3.3.4: Root-mean-square skill score of the bathymetric lines (a) after 400 d and (b) after 1150 d, as a function of f_c, μ, and ν.

can be explained by a lack of capacity to redistribute the accumulated sediment in the cross-shore direction. The best $RMSSS$ was obtained for $f_c = 0.15$ and $\mu = 0.04\ m^{1/2}s^{-1}$. When using these values, the $RMSSS$ was similar for $\nu = 0.03$ and $\nu = 0.05$. We have chosen the latter to ensure the simulations stability in energetic situations.

3.3.2 Model validation

To validate the model, the $RMSSS$ is also computed after 1150 d for the same range of parameter values of the previous section, confirming that the calibrated parameter values have the best performance (Fig. 3.3.4b). In particular, after 400 d, $\mu = 0.01$ m$^{1/2}$s^{-1} and $\mu = 0.04$ m$^{1/2}$s^{-1} have similar performance but after 1150 d their performance gap increases and $\mu = 0.04$ m$^{1/2}$ clearly reproduces the observations more accurately. This can be explained by the initially fast cross-shore dynamics in the model (see Section 3.3.3), adapting rapidly (i.e. faster than in reality) the profile (hence, the contours) to a quasi-equilibrium state. This adaptation initially disguises the role of μ.

The $RMSSS$ of the calibrated model after 1150 d is about a factor 3 larger than after 400 d (Fig. 3.3.4). The skill score of the calibrated model increases continuously in time because $RMSE(B, Y)$ experiences a continuous increase (Fig. 3.3.5) due to the ZM diffusive

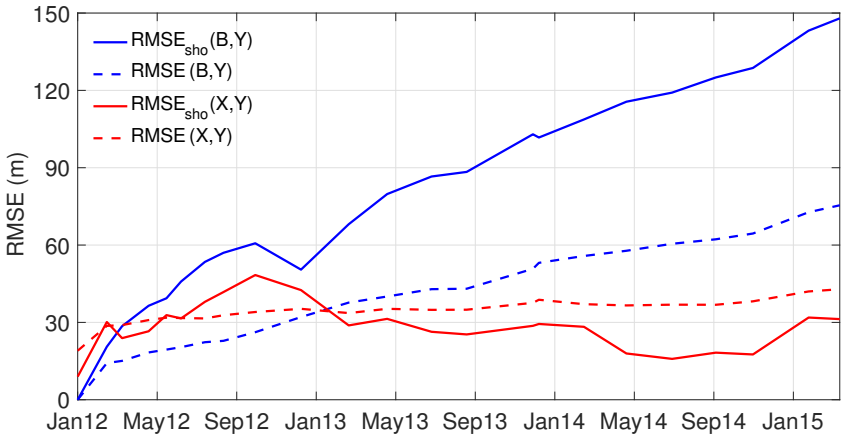

Figure 3.3.5: Comparison of $RMSE$ of the no-change prediction (blue lines) and $RMSE$ of the calibrated model (red lines). The solid lines correspond to the shoreline and the dashed lines correspond to the bathymetric lines until 10 m depth.

nature whereas $RMSE(X,Y)$ hardly grows (Fig. 3.3.5). In fact, the $RMSSS$ increases for every set of parameter values, so that a sub-optimal set of tuning calibration parameters (μ, f_c, ν) may eventually reach high $RMSSS$ values. Therefore, we have to interpret the $RMSSS$ values carefully. The Q2Dmorfo is based on the one-line approach and, as such, is expected to represent better the shoreline than the bathymetric lines. Indeed, the root-mean-square error of the shoreline, $RMSE_{sho}(X,Y)$, shows an initial increment then a decay and a subsequent stabilization while oscillating around 30 m (Fig.3.3.5). The modelled shoreline differs from the observed one in the north-east side (Fig. 3.3.6a) because the model does not take the interaction between the lagoon and the sea into account. Also, small scale undulations in the bathymetric lines (related to processes such as surfzone dynamics) are not captured in the simulations and are a persistent error source in the quantification (Fig. 3.3.6b).

To further validate the model results, we also compared how the volumes of sand changed over 1150 d in three control boxes (CB) representative of the ZM tip (B) and the adjacent beaches (A, to the SW, and C, to the NE, see Fig. 3.2.2a). Here, CB-B is expected to loose sand while the CB-A and the CB-C are expected to gain sand. A quantification of the performance is given with the following averaged volume error

$$E_* = \frac{\sqrt{\frac{1}{N}\sum_{i=1}^{N}(V_*(i)_{sim} - V_*(i)_{mes})^2}}{max(V_{*mes}) - min(V_{*mes})} \tag{3.3.1}$$

where V_* stands for the volume in box *, i for the survey number, N for the number of

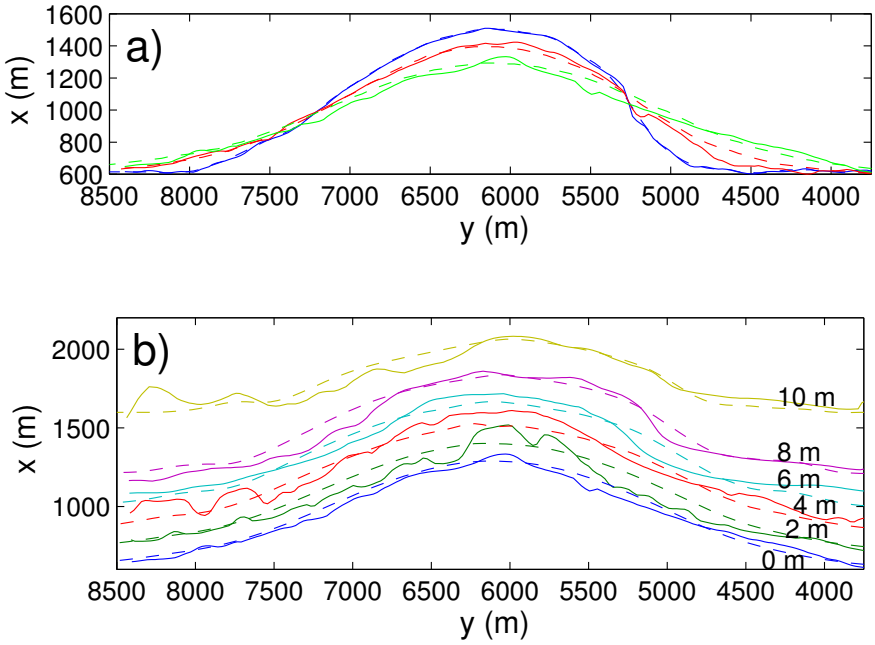

Figure 3.3.6: (a) Shoreline position on January 2012 (blue), after 400 d, on March 2013 (red), and after 1150 d, on March 2015 (green). (b) Bathymetric lines every 2 m until 10 m depth after 1150 d. Measured (solid line) and modelled (dashed line).

surveys, *sim* for simulations and *mes* for measurements. Overall, the diffusion of the ZM over the adjacent beaches is well represented by the model (Fig. 3.3.7). The modelled loss of sand in the tip (CB-B) resembles the measured one ($E_B = 0.09$). The initial offset in volume is a result of the linear interpolation used in the construction of the modelled bathymetry (the modelled wet area had 0.5 % less sand than the survey). To reveal more detail, the tip area, CB-B, is decomposed into its south-west (Fig. 3.3.7BA) and north-east (Fig. 3.3.7BC) sides. The CB-BC has a lower error ($E_{BC} = 0.07$) than the CB-BA ($E_{BA} = 0.17$), and their behaviour is consistent with their respective tip sides ($E_C = 0.06$ and $E_A = 0.19$). The model generally underestimates the volume in CB-A except for the last survey, while for CB-C the differences are small throughout time except for the under-feeding observed in the last survey. In general, the modelled volume change (Fig. 3.3.7, right axis) of CB-B, CB-BA and CB-BC follow the measured trend with small differences of magnitude while the modelled and measured volume changes of CB-A and CB-C (the ones being fed) show more significant differences. The long-term trend in the total volume behaviour is well captured.

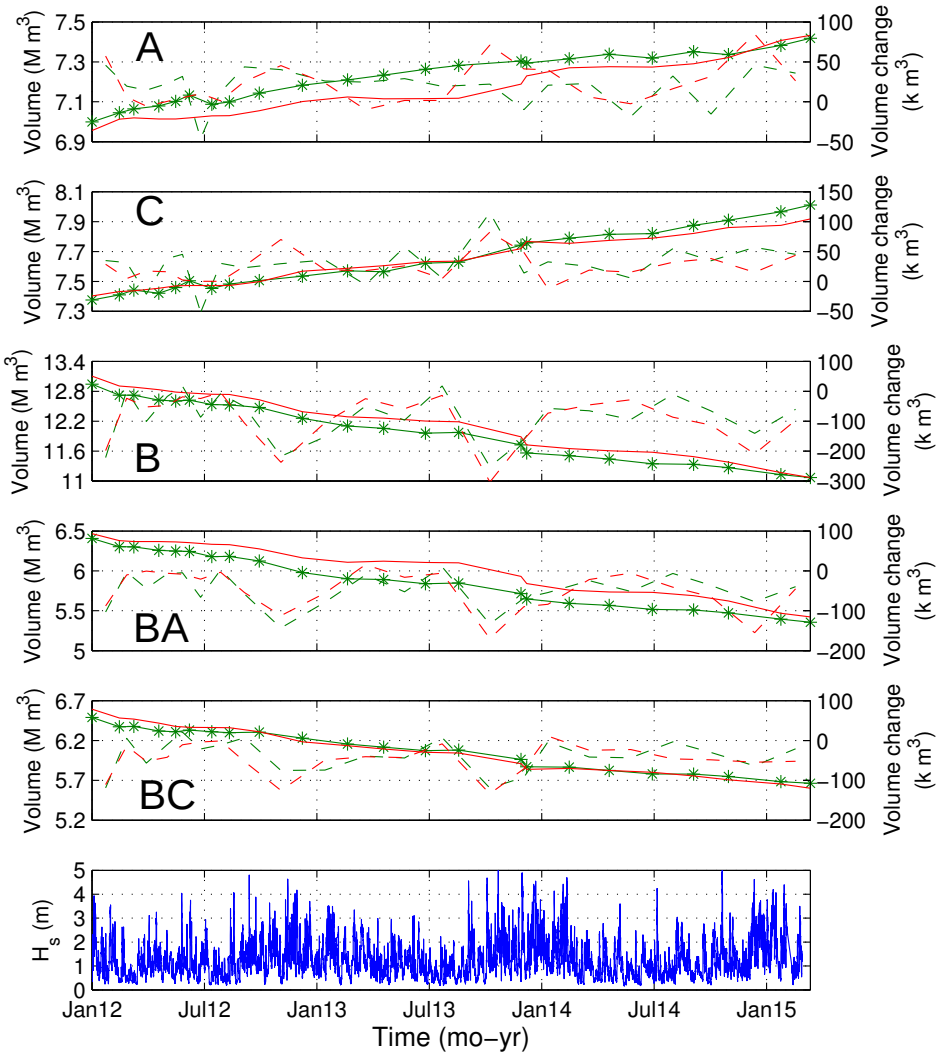

Figure 3.3.7: Modelled (red) and measured (green) total volume (solid lines) and volume change (dashed lines) in the control boxes defined in Fig. 3.2.2a. The asterisks indicate the surveyed data points. The significant wave height is plotted in the lower panel.

3.3.3 Computation of shoreline diffusivity

The diffusivity of the ZM, both in reality (ϵ_{obs}) and in the simulations (ϵ_{Q2D}), is here examined using the concept of shoreline diffusivity which is easily formulated within the framework of the one-line approximation for shoreline dynamics. By assuming a certain alongshore sediment transport simplification/parametrisation and neglecting the feedback of

bathymetric changes into the wave propagation, the Pelnard-Considère equation is obtained (Pelnard-Considère, 1956)

$$\frac{\partial x_s}{\partial t} = \epsilon \frac{\partial^2 x_s}{\partial y^2} \tag{3.3.2}$$

where ϵ is the diffusivity coefficient, which depends on the wave condition and the depth of closure (see Eq.3.3.6).

An analytic solution of Eq. (3.3.2) is derived by approximating the initial shoreline, $x_s(y,0)$, to a Gaussian shape (e.g. after 1150 d the surveyed shoreline has a 18.6 m mean square error with respect to a Gaussian shape) and then expanding it as a Fourier integral, leading to

$$x_s(y,0) = A_0 e^{-((y-y_a)/L)^2} = A_0 \frac{L}{\sqrt{\pi}} \int_0^\infty e^{-k^2 L^2/4} \cos(k(y-y_a))dk \tag{3.3.3}$$

where A_0 is the initial amplitude, L is the initial Gaussian width and y_a is the alongshore location of the crest. Using the boundary conditions: $x_s(-\infty,t) = x_s(\infty,t) = 0$, and performing some computations, the analytic solution of Eq. (3.3.2) can be cast into:

$$x_s(y,t) = A(t) \exp\left(-\frac{(y-y_a)^2}{L^2 + 4\epsilon t}\right) \tag{3.3.4}$$

where the amplitude is

$$A(t) = \frac{A_0}{\sqrt{1 + 4\epsilon t/L^2}} \tag{3.3.5}$$

The classical diffusivity coefficient, ϵ_{cla}, obtained using the CERC formula for the alongshore transport in Eq. (3.3.2), is

$$\epsilon = \epsilon_{cla} = 2\mu \frac{H_b^{5/2}}{D_c} cos(2\theta_b). \tag{3.3.6}$$

To evaluate ϵ_{cla} a constant D_c of 8 m is assumed. This depth-of-closure value is inferred from the measured contours and is consistent with the analysis of de Schipper *et al.* (2016). To compute the instantaneous H_b and θ_b in Eq. (3.3.6), waves are propagated from the buoy until the breaking point with the Snell law and the energy conservation, assuming parallel contours to a straight shoreline. Then, we average the resulting instantaneous diffusivity coefficient over the three years of evolution, giving $\epsilon_{cla} = 0.0052$ m^2/s.

By using Eq. (3.3.5), time dependent values of the modelled and observed diffusivity, ϵ_{Q2D} and ϵ_{obs}, can be inferred from the corresponding $A(t)$. The initial amplitude, A_0, and width, L, are obtained by fitting the Gaussian function to the initial shoreline, $x_s(y,0)$, and the subsequent amplitudes, $A(t)$, to the instantaneous shoreline, $x_s(y,t)$. Notice that ϵ_{Q2D} and ϵ_{obs} represent the effective diffusivity between the initial state and time t. ϵ_{obs} decreases in time and stabilizes after ∼200 d (April 2013) to 0.0022 m^2/s (Fig. 3.3.8a). Until this moment the diffusion may not only be driven by alongshore transport (the assumption behind Eq. (3.3.2)) but also by cross-shore transport, since the perturbed profile is far from the characteristic local equilibrium profile. Similarly, ϵ_{Q2D} stabilizes to 0.0021 m^2/s but the model over-predicts the initial cross-shore transport contribution (Fig. 3.3.8a). During the

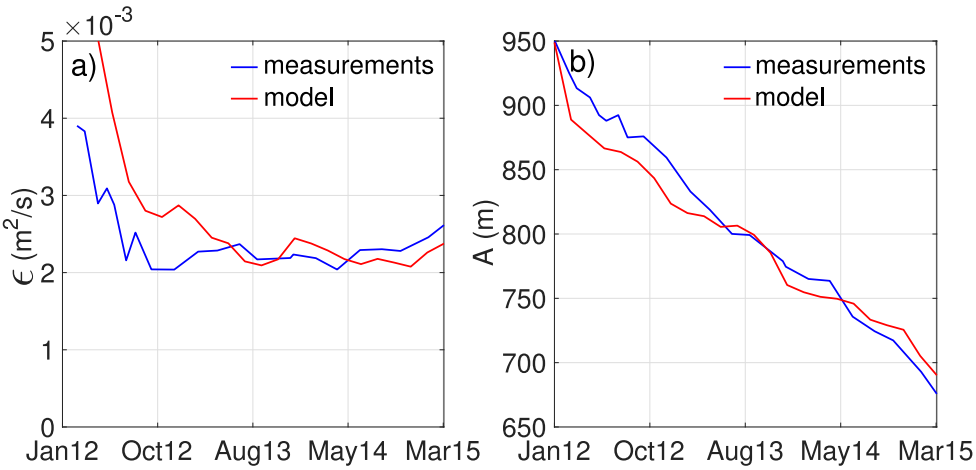

Figure 3.3.8: (a) The diffusivity coefficients and (b) the amplitudes, based on the measurements (blue line) and on the Q2Dmorfo simulations (red line), versus time.

first days the modelled amplitude decays by 40 m (Fig. 3.3.8b), suggesting a misrepresentation of the cross-shore transport when the initial profiles are far from the defined equilibrium profile. However, the time evolution of the modelled cumulative diffusivity presents a change in slope around 200 d (Fig. 3.3.8a), which agrees with the stabilization time of the measurements, and after 500 d the model catches up with the measurements. A lower ν value could reduce the cross-shore transport over-prediction but numerical instabilities may then arise during energetic events.

3.4 Long-term evolution and feeding capability

3.4.1 Wave climate scenarios

For the long-term analysis, a total simulation time of 30 yr has been chosen which is safely longer than the envisaged time of 15-20 yr (de Schipper *et al.*, 2014; Stive *et al.*, 2013). Considering the validation time of 3 yr, the long-term modelling is performed over 27 yr. To account for variability in the future wave climate (hereafter referred to as WC), five different WC scenarios have been designed based on the available wave data prior to the last validated simulation (01 March 2015). First, a time interval of m yr is defined and then is repeated until reaching the 27 yr duration. The chosen intervals are $m = 1, 3, 5, 10, 20$ yr, so that when $m = 1$ the interval is from March 2014 to March 2015 and repeats itself 27 times, for $m = 3$ the interval is from March 2012 to March 2015 and repeats itself 9 times, etc.

Table 3.4.1: Statistics of the modelled wave climate scenarios, where H is computed in H_s terms and T in T_p terms.

WC	m	$\bar{H}_W(m)$	$\bar{H}_N(m)$	$\bar{T}_W(s)$	$\bar{T}_N(s)$	$\bar{\theta}_W$	$\bar{\theta}_N$	$\frac{P_T 10^8}{(W/m)}$	$\frac{P_W}{P_N}$	$\%\theta_{oblique}$
1	1	1.48	1.00	5.87	5.90	60.2	45.2	1.93	2.71	61.6
2	3	1.42	1.06	5.77	5.94	61.7	45.9	1.92	2.02	61.9
3	5	1.41	1.10	5.76	6.00	61.4	45.3	2.01	1.80	60.9
4	10	1.40	1.13	5.78	6.00	60.1	44.9	2.02	1.66	59.4
5	20	1.39	1.13	5.82	6.01	59.8	44.2	1.90	1.62	58.0

The WC characteristics, evaluated at the buoy depth of 32 m, are analysed by first separating the waves coming from the west i.e. $\theta_0 < 0°$ with respect to the global shoreline orientation (hereafter referred to as W waves) from the waves coming from the north i.e. $\theta_0 > 0°$ with respect to the global shoreline orientation (hereafter referred to as N waves). Then, the averaged H, T and θ are computed for W and N waves. Also, the alongshore component of the wave energy flux is calculated as

$$P = \frac{1}{8}\rho g H^2 C_g \sin\theta \tag{3.4.7}$$

where ρ is the water density. The accumulated module of P is computed as $P_T = \sum(|P|)$, and the wave power asymmetry is evaluated as the ratio P_W/P_N. Finally, the percentage of oblique waves (angle larger than $|45°|$), $\%\theta_{oblique}$, is computed.

The average conditions of the five WC are similar (Table 3.4.1). In general, the W waves are more oblique and more energetic than the N waves. The dominant W wave energy flux is consistent with the known net alongshore sediment transport direction from SW to NE (van Rijn, 1997). The maximum $\bar{H}$ difference among the five different WC is 0.134 m for $\bar{H}$ (for the W waves), while for $\bar{T}$ is 0.11 s (for the N waves), and for θ is 1.72° (for the N waves). The resemblance in wave statistics gives small differences in P_T but the wave power asymmetry shows a decay with larger m values (e.g. $P_W(m = 1) = 2.71P_N$ and $P_W(m = 20) = 1.62P_N$). A similar tendency is observed in $\%\theta_{oblique}$, which decreases with increasing m, indicating an increment of wave obliquity in recent years.

3.4.2 Diffusion and feeding properties

The long-term simulations performed show that the ZM is expected to exhibit continuous diffusion during more than 30 yr (Figs. 3.4.9 and 3.4.10). Therefore, the wave obliqueness of the WC scenarios is not large enough to trigger the formation of self-organized large-scale shoreline-sand waves. The long-term effective diffusivity is inferred by using the modelled ZM amplitude, $A(t)$, and Eq. (3.3.5) with A_0 and L corresponding to the first long-term simulation (01 March 2015). After some initial variability (during about 5 yr), the effective diffusivity stabilizes and the averaged value of the last 5 yr is shown in Table 3.4.2. The least diffusive wave climate is WC2, and the most diffusive is WC5, with a 40 m difference in amplitude after 27 yr.

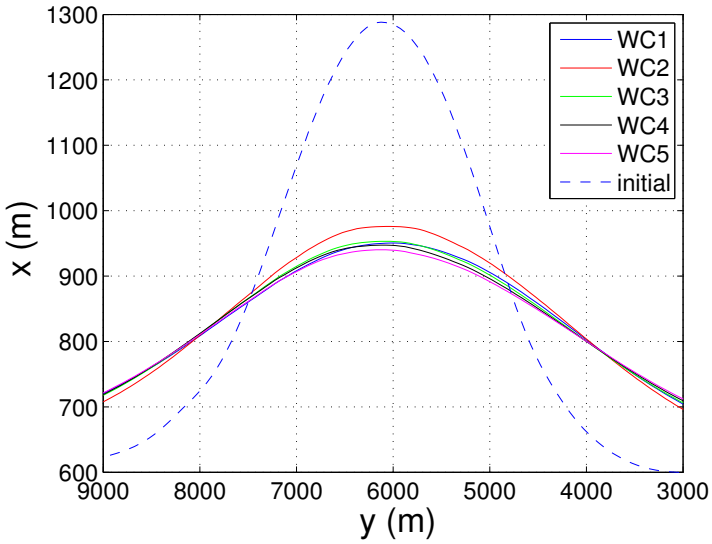

Figure 3.4.9: Shoreline modelled on March 2015 (dashed line) and shorelines predicted for the WC 30 yr after construction (solid lines).

The one-line approximation using the classic diffusive coefficient, ϵ_{cla}, computed in Section 3.3.3, predicts a significantly larger decay. As shown in Fig. 3.4.10, after 10 yr the amplitude predicted by the classical one-line approach would be 31% smaller than the one predicted by the Q2Dmorfo model. Using $\epsilon_{Q2D} = 0.0021$ m^2/s (calculated with the first 3 yr evolution), the one-line approach follows reasonably well the amplitude although after the first five years starts to diverge (Fig. 3.4.10). The lifetime of the ZM can be defined as the time period required for its amplitude to decrease to a given factor of its amplitude after construction, and here we choose a factor 0.2. Using $\epsilon_{cla} = 0.0052$ m^2/s the lifetime is ~ 35 yr, while using $\epsilon_{Q2D} = 0.0021$ m^2/s the lifetime is ~ 90 yr. These values are substantially larger than the envisioned lifetime of 15-20 yr (de Schipper *et al.*, 2014; Stive *et al.*, 2013).

The diffusion of the ZM produces a widening of the perturbation (Fig. 3.3.6), which implies feeding sand to adjacent beaches, measured here in terms of average linear meter gained at the beach:

$$\overline{\Delta x}_s(t) = \frac{1}{y_2 - y_1} \int_{y_1}^{y_2} (x_s(y,t) - x_s(y,0))dy \tag{3.4.8}$$

The NE section ranges from $y_1 = 2100$ m to $y_2 = 4600$ m and the SW section from $y_1 = 7600$ m to $y_2 = 10100$ m. These 2.5-km long sections avoid the mainly diffusive area of the ZM tip and the influence area of the harbours. Also, they are located at the same distance from the maximum amplitude position of the initial shoreline ($y = 6100$ m for 01 March 2015, as shown in Fig. 3.3.6). According to the model results, shown in Fig. 3.4.11, the NE section becomes wider than the SW section (about 100 m and 80 m, respectively,

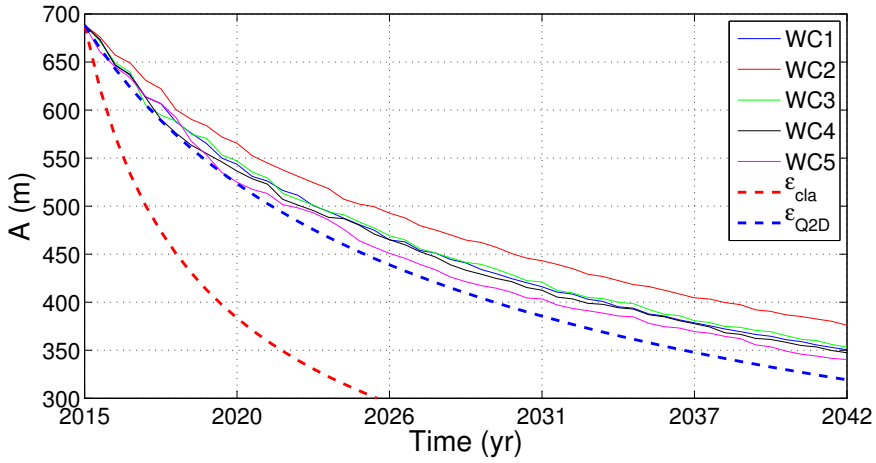

Figure 3.4.10: Modelled amplitude of the ZM during 27 yr, starting from March 2015.

after 27 yr). Both sections show notorious less feeding for the WC2 (coherent with the less diffusive behaviour of that scenario). The feeding asymmetry, FA, is defined as the relative difference in $\overline{\Delta x}_s$ in NE and SW beaches and is evaluated as

$$FA = 2\frac{\overline{\Delta x}_{sNE} - \overline{\Delta x}_{sSW}}{\overline{\Delta x}_{sNE} + \overline{\Delta x}_{sSW}} \tag{3.4.9}$$

The one-line approach can not reproduce accurately the feeding magnitude nor the feeding asymmetry of the ZM (Fig. 3.4.11), using ϵ_{cla} the feeding is over-predicted by about 30 % after 10 yr and from then on it predicts retreat (also, see Fig. 3.4.12). By using ϵ_{Q2D}, the one-line approach predicts much better the model results. Table 3.4.2 shows the averaged FA over the last 5 yr of simulations, the WC2 produces the largest FA while the remaining WC produce similar FA. The predictions of the shoreline sections using the WC3 for the Q2Dmorfo model and the one-line approach are shown in Fig. 3.4.12. The alongshore migration rate, V, of the shoreline perturbation was computed by finding the spatial lag for which the correlation between subsequent modelled shorelines, with a 20 d time step, is maximum. The obtained V over the 27-yr period are small and north-east directed with a certain scatter for the different WC (Table 3.4.2), confirmed by the displacement of the crest position, y_c (Fig. 3.4.13a). The wave power asymmetry, P_W/P_N, is the wave property that best correlates with the migration rate, i.e. the larger P_W/P_N the larger V (to the NE).

The shoreline shape asymmetry, SA, is here quantified as the relative difference between the beach areas (measured with $\overline{\Delta x}_s$) between the northern and southern sides of the tip with the same Eq. (3.4.9) of FA. However, to account for migration and widening of the perturbation we used dynamic integral limits $y_1 = y_c - L_g, y_2 = y_c$ for the northern side and $y_1 = y_c, y_2 = y_c + L_g$ for the southern side, where y_c is the moving crest position and L_g is the width of the evolving fitted Gaussian. SA diminishes slightly for WC5, is rather stable for WC2, WC3 and WC4, and increases for WC1 (Fig. 3.4.13b). Table 3.4.2 shows the mean

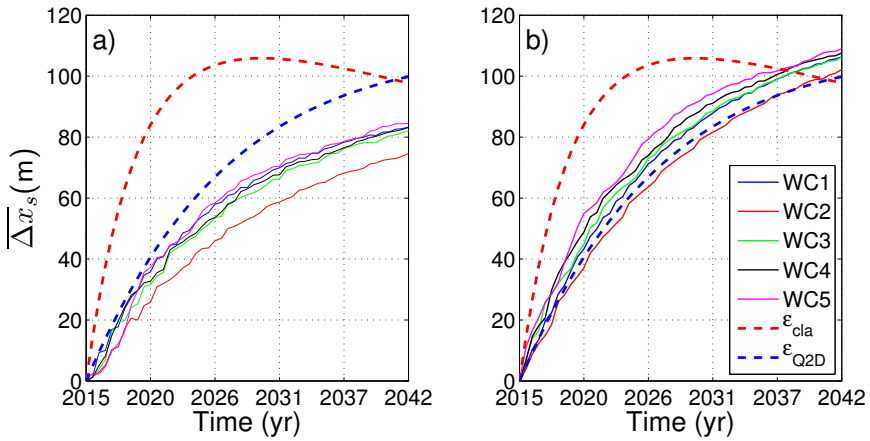

Figure 3.4.11: Beach linear meter gained in the defined sections along the coast (a) south-west and (b) north-east to the ZM during 27 yr, starting from March 2015.

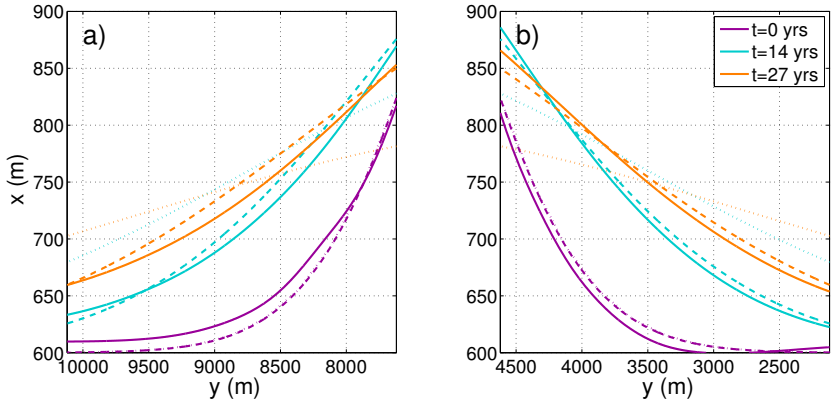

Figure 3.4.12: (a) Coastlines of the south-west section and (b) north-east section predicted by the Q2Dmorfo model using WC3 (solid lines), and by using the one-line approach with ϵ_{Q2D} (dashed lines) and ϵ_{cla} (dotted lines).

SA over the last 5 yr of evolution. A negative SA denotes a larger shoreline slope in the NE than in the SW. The SA, just as V, correlates best with the wave power asymmetry.

Table 3.4.2: Morphologic parameters of the ZM behaviour for the five WC, computed over the last five years of simulation.

WC	ϵ m^2/s	V m/yr	FA	SA
1	0.0016	-4.3	0.24	-0.016
2	0.0013	-3.4	0.31	-0.010
3	0.0016	-2.2	0.26	-0.007
4	0.0017	-1.8	0.26	-0.006
5	0.0018	-1.1	0.25	-0.003

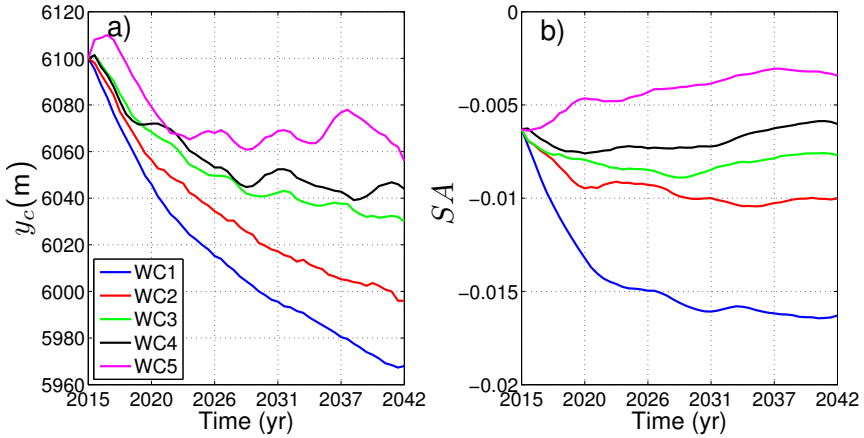

Figure 3.4.13: (a) Position of the ZM crest, y_c, and (b) the shoreline shape asymmetry, SA, during 27 yr, starting from March 2015.

3.5 Discussion

3.5.1 Calibrated parameter values

The model uses a series of parameters for the simulation of the alongshore and cross-shore sediment transports. In particular, the three empirical parameters are related to (i) the factor in the wave-driven alongshore transport (parameter μ), (ii) the depth of closure D_c (parameter f_c), and the diffusivity factor in $\vec{q_N}$ and $\vec{q_D}$ (parameter ν). The non-dimensional K parameter, directly related with the μ parameter in the CERC formula, has been evaluated with the 400 initial days of ZM evolution and the obtained optimal value is $K = 0.14$ (using H_{rms} in the CERC formula, Eq. 2.2.9). This value is unexpectedly small, somewhat smaller than the lower limit reported by Komar (1998). However, the value of K is generally highly uncertain (see, e.g. Cooper & Pilkey, 2004) and for example, Wang *et al.* (1998) reported an even smaller value of $K = 0.08$. Thus, the ZM calibration provide a valuable opportunity

of evaluating the effective K coefficient for such a large sand body.

Also, the annual alongshore sediment transport is computed (Q_{annual}) with the calibrated CERC formula to asses the quantity of sand being transported and also to compare it to previous studies. The computation has been done by transforming the waves with the Q2Dmorfo model over an unperturbed bathymetry (i.e. rectilinear contours parallel to the coast, without the ZM) and assuming no morphological change for the waves from 1990 to 2014. The annual Q_{annual} displays a high annual variability (Fig. 3.5.14). During the 24-yr period there is a net quantity of sand transported to the SW direction of 45,376 m^3 (annual mean of about 1,900 m^3), which is quite small compared with the largest Q_{annual} obtained for 2010 (some 250,000 m^3). Therefore, this indicates that there is no dominant sediment transport direction. This is in contrast with the results reported by van Rijn (1997), who analysed the wave climate of the period 1980-1993 and found that the sediment transport was clearly directed towards the NE in that area. In agreement with our findings, he found significant annual variability (e.g. using the wave climate of 1989 instead of that of 1994, the transport changed a factor 20). The discrepancy could be due to the differences in the study period and the wave station location. Wave-direction data is only available for us from the EURO-platform since April 1989, whilst van Rijn (1997) employed data from 1980 to 1993.

The depth of closure, D_c, is typically defined as the largest depth where bed level changes, during a certain time period (typically one year), are above a certain threshold of bottom change U_{zb} (Hallermeier, 1978; Komar, 1998). Choosing $U_{zb} = 0.1$ m, using the ZM bathymetric measurements, we find $D_c = 9.2$ m, which agrees with the D_c computed with the Hallermeier formula (using the 12 h exceeding wave height). The Q2Dmorfo model uses an instantaneous D_c value that is computed from the instantaneous wave conditions as a fraction, f_c, of the depth where sediment starts to be mobilized by waves. The calibration procedure finds $f_c = 0.15$, so that the resulting D_c, averaged for the observed 12 h exceeding waves, is 9.5 m. In contrast, Hinton & Nicholls (1998) determined a $D_c = 5$ m for an area nearby the ZM, on the basis of a large bottom threshold, $U_{zb} = 0.5$ m. This was motivated by the vertical accuracy of 0.25 m of the JarKus data. Using the same threshold on the ZM measurements a D_c of 6.5 m is found. The D_c values reported by de Schipper *et al.* (2016) for the ZM of 7-8 m are slightly smaller than our inferred D_c. Thus, despite that D_c is usually understood as a statistical measure whereas our D_c is an instantaneous value, our calibrated formulation and simulations agree quite well with the literature and the measurements.

The Q2Dmorfo model could be a useful tool to test the design of mega-nourishments, in which case the different parameters of the model should be previously calibrated. As we have discussed in the previous paragraph, the Hallermeier formula can be used as a proxy for the depth of closure to then obtain a value for f_c. The two factors μ and ν in front of the transports should be calibrated for the specific site before applying the model. Also, if the beach of interest has similar geophysical properties as the ZM beach, the values for the parameters used in this contribution may be a good proxy. However, it is important to keep in mind that the Q2Dmorfo model does not include processes that could play a role in the long-term behaviour of the ZM: surf-zone hydrodynamics, tides and aeolian sand transport.

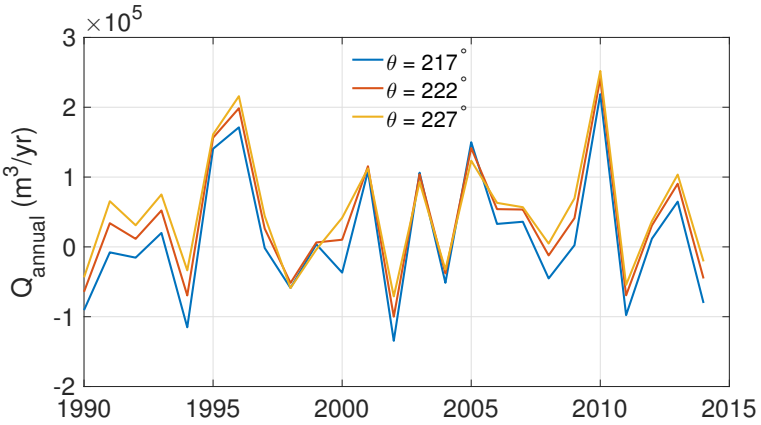

Figure 3.5.14: Net annual alongshore sediment transport computed with the Q2Dmorfo model over an unperturbed bathymetry, where $Q > 0$ means transport towards SW direction. The local shoreline orientation is of 222° and the sensitivity of the transport to a variation in orientation of ±5° is also shown.

3.5.2 The role of HAWI in the ZM evolution

Given that the wave climate on this stretch of coast has a large proportion of high-angle waves (i.e. offshore wave incidence angle larger than 45°) the ZM project provides a unique opportunity of checking high-angle wave instability (HAWI) theory. Ashton & Murray (2006*b*) presented a one-line approach where the feedback of the bathymetric changes into the wave propagation is simplified, neglecting the curvature of the depth contours. They obtained a diffusion equation similar to Eq. (3.3.2) where the diffusivity ϵ can be negative for high-angle waves. We have computed the averaged diffusivity for the first three years with this approach and we have obtained $\epsilon = -0.0030$ m^2/s, i.e. the coastline would become unstable so that self-organized large-scale shoreline sand waves might form. In contrast, both the measurements during the first three years and our model predictions for 30 yr of the ZM, with $\epsilon = 0.0014 - 0.0022$ m^2/s, are diffusive. Apparently, the simplifications in the approach of Ashton & Murray (2006*b*) over-predict the occurrence of HAWI. Indeed, in their approach only 50% of high-angle waves is required for a negative diffusivity whereas Q2Dmorfo model requires a percentage of about 80% (van den Berg *et al.*, 2012) which also agrees with Kaergaard & Fredsoe (2013*b*). Thus, the observed Dutch wave climate featuring only about 60% of high-angle waves could explain why the ZM is, in fact, diffusive. However, van den Berg *et al.* (2012) considered a constant offshore wave height. Here, using real time-varying wave conditions the percentage of oblique waves during storms might have more influence in the ZM behaviour than the percentage of oblique waves in calm conditions. So, we have further analysed the energetic waves ($H > 2$ m) in WC4, $\sim 80\%$ of the W high-energetic waves are above the threshold while only $\sim 30\%$ of the N high-energetic waves are above it. Therefore, the ZM could show an anti-diffusive behaviour during the SW energetic events.

HAWI is induced by a positive feedback between the undulations in the depth contours and the associated perturbations in wave refraction and shoaling while damped by the undulations in the coastline. For relatively low wave incidence angles, the instability source is negligible, the stabilizing effect dominates and the shoreline perturbation diffuses with a diffusivity that is nearly independent on the angle. This is quite well reproduced by the classical one-line approach. In contrast, for relatively high wave angles the diffusivity depends on wave angle and eventually becomes negative above some threshold. Therefore, the significant influence of the wave angle on the diffusivity found with Q2Dmorfo model suggests that the ZM is far from the purely diffusive situation described by the classical one-line approach and 'near' the HAWI threshold. For example, by jumping from 58% (WC5) to 62% (WC2) of high-angle waves the diffusivity drops by 16%. Furthermore, the over-prediction of the diffusivity by a 2.5 factor by the classical one-line approach is clearly a result of neglecting wave obliquity. Indeed, by forcing the real wave climate to have normal incidence (the period and wave height still vary) we find a diffusivity of $\epsilon = 0.0053$ m^2/s, which is near the classical theory with $\epsilon_{cla} = 0.0052$ m^2/s, confirming the important role of wave incidence on the diffusivity. According to Falqués (2003) (see Fig. 5 of that paper), this 2.5 factor means that HAWI would be reached by increasing wave obliquity roughly by 18%. Thus, as already suggested by Falqués (2006), the Dutch coast is near the HAWI threshold.

Finally, a perfect diffusive behaviour would show a constant ϵ, while the diffusivity of the modelled shorelines drops from 0.0021 m^2/s, for the three-year validation period, to 0.0013-0.0018 m^2/s, for the 27-yr long-term period. Initially, the ZM perturbation is pronounced at the shoreline but relatively weak at the depth contours, which results in a relatively strong diffusive behaviour. However, through time, the mismatch between depth contours and shoreline tends to decrease, resulting in stronger de-stabilizing effects. If the diffusivity continues declining, a relict of the ZM may eventually survive. Therefore, feedback processes underlying HAWI are clearly active at the ZM even if stabilizing effects slightly dominate under the present wave climate.

3.5.3 Feeding asymmetry

The idea behind the ZM project is a mega-nourishment that feeds sand to adjacent beaches on a decadal time scale (de Schipper *et al.*, 2016). Both the measurements of the first 3 yr (Fig. 3.3.7) and the long-term simulations of 30 yr (Fig. 3.4.11) indicate that there is an asymmetry between the feeding to the NE beaches and the SW beaches, the latter feeding being smaller. de Schipper *et al.* (2016) already detected an asymmetry in the feeding by analysing the first year of the ZM evolution, and suggested that this is a consequence of the dominant NE alongshore transport direction although in our analysis there is no indication of this dominance. Most important, the changes in shoreline position are governed by gradients in transport, not by the transport itself. Such transport gradients can be interpreted with the following three time-varying characteristics of the perturbation: diffusivity, ϵ, migration, V, and the shoreline asymmetry, SA. The magnitude of the feeding is primarily controlled by ϵ, which decreases the ZM amplitude and increases its width, whilst the feeding asymmetry, FA, may be related to V and SA. Large northward V should produce larger feeding to the NE beaches, and hence a larger FA, but this effect is weakened if the perturbation has negative SA. Note also that the larger the wave power asymmetry, P_W/P_N, the larger SA

and V (Tabs. 3.4.1 and 3.4.2). Table 3.4.2 suggests that V and SA compensate each other, resulting in very similar FA (for WC1, WC3, WC4, and WC5). Note that the arguments in this paragraph rely on an idealization, but in reality the transport gradients are more complex. For instance, a wave climate with a larger percentage of oblique waves, where HAWI processes become more important, adds complexity to the sediment transport. This may explain why FA for WC2 is 20% larger than the FA from the other climate scenarios. Therefore, a model, such as the Q2Dmorfo, is required to predict such details in the long-term.

3.6 Conclusions

A morphodynamic model called Q2Dmorfo has been successfully calibrated and validated with bathymetric measurements of a mega-nourishment constructed in July 2011 on the Dutch coast (Zandmotor, ZM), which is characterized by a bimodal wave climate with a significant percentage of high-angle waves. After being calibrated with the bathymetries measured during 1 yr, the model can properly reproduce the observed ZM evolution during the next 2 yr, not only the shoreline but also the depth contours so that sand volumes are well represented. The calibration of the model provides a value of the non-dimensional K parameter of the CERC formula of $K = 0.14$, which is at the lowest limit of the values reported in the literature.

Long-term model simulations have been performed using five different wave climate scenarios, WC. Results show that the shoreline will behave diffusively, so that the amplitude of the perturbation will have decayed from the initial 960 m (immediately after construction) to about 350 m, 30 yr after the ZM installation. At the same time, the shoreline of the adjacent beaches, 2.5 km at each side, will have shifted seaward (on average) by about 100 m at the NE defined section and about 80 m at the SW defined section. These results are very robust since they are reproduced with the five applied WC. The model predicts small alongshore migration rates (due to the bidirectional WC) and a maintenance of the shape asymmetry, SA, and both parameters correlate with the wave power asymmetry. The diffusivity is smallest for the WC showing the largest percentage of high-angle waves.

An effective diffusivity of the shoreline, due to the alongshore sediment transport, has been evaluated by analysing the shoreline evolution during the first 3 yr, obtaining similar results for the measured and the modelled shorelines, $\epsilon_{obs} = 0.0022$ m^2/s and $\epsilon_{Q2D} = 0.0021$ m^2/s, respectively. In contrast, the classical one-line approach over-predicts the diffusion by a factor of 2.5, $\epsilon_{cla} = 0.0052$ m^2/s. Therefore, the ZM lifetime, here defined as the time needed to reduce the amplitude after construction by a factor 5, predicted by ϵ_{cla} is of only ~ 35 yr instead of the ~ 90 yr computed with the ϵ_{Q2D}. It is found that the alongshore-driven effective diffusivity must be evaluated at least 1 yr after the mega-nourishment construction to avoid the strong influence of cross-shore transport at the initial states when the perturbed profiles are far from equilibrium. Although the measurements over the first three years and the model predictions for 30 yr show a diffusive behaviour of the ZM, the significant reduction in coastline diffusivity compared with the classical one-line approach, attributable to wave obliquity, confirms that the Dutch coast is not far from high-angle wave instability.

A morphodynamic model like the Q2Dmorfo, which includes more physical processes than the one-line approach but still allows performing long-term simulations, is especially suited to predict the shoreline evolution of mega-nourishments. In particular, the model can be a useful tool for the design of mega-nourishments since it can accurately reproduce the diffusion, the alongshore migration, and the feeding asymmetry to adjacent beaches.

Chapter 4

Diffusion of mega-nourishments

4.1 Introduction

The ZandMotor (ZM) is the largest beach nourishment in the world and one of the few human actions that have the purpose of mitigating the effects of climate change and the associated sea-level rise (Stive *et al.*, 2013). In Chapter 3 of this thesis, the Q2Dmorfo model was calibrated with 3-yr measured morphological data, starting from 17 January 2012, and was used to predict the ZandMotor evolution in the long term. The results shed light in the diffusion dynamics of the mega-nourishment (MN) and other propertires such as its migration and the feeding of sand to adjacent beaches. For example, the lifetime predicted by the model is at least three times larger than the expected one (i.e. in the initial design). This is attributed to the diffusion effect of the incoming oblique waves (Arriaga *et al.*, 2017). However, the role of the shape and size of the mega-nourishment was not investigated. Also, due to the variability in wave characteristics of the real wave climate used in the simulations, it was not possible to pinpoint the diffusion contribution of the different types of wave conditions. The same occurred for more complex nourishment traits such as the sand feeding asymmetry to adjacent coasts and the shape asymmetry.

Tonnon *et al.* (2018) designed analytic mega-nourishments (from now on referred to as AMN) assuming a trapezoidal shoreline, and the associated bathymetry followed an equilibrium profile. They principally used the UNIBEST model (based on the one-line concept) to study the evolution of the AMNs. The validation was done by comparing its results with the Delft3D but the actual modelled perturbations had different volume sizes in the two models. This was attributed to the fact that the UNIBEST assumes a uniform cross-shore shape and the Delft3D applies more volume in deeper water for larger nourishments. Therefore, it was difficult to control the sand volume in the AMN design.

This chapter is the basis of the article in preparation Arriaga *et al.* (2018*b*): Arriaga, J., Ribas, F., Falqués, A., Rutten, J. & Ruessink, B. 2018*b* Long-term performance of mega-nourishments: role of the initial shape and the wave climate. *Coast. Eng.* In preparation

The synthesizing of the wave climate has been used in previous studies to reduce the complexity of the forcing and understand more easily the associated large-scale morphological responses (Ashton & Murray, 2006*a*; van den Berg *et al.*, 2011; Kaergaard & Fredsoe, 2013*b*). The most extreme case is to consider only one wave condition as representative of the real wave climate (see the application of the West coast of Denmark in Kaergaard & Fredsoe, 2013*b*). However, this means that there is only one wave direction, which is very unrealistic when the wave climate is bimodal and can result in large artificial migration celerity of nourishments, as noted by van den Berg *et al.* (2011). In the context of high-angle wave instability modelling, four wave conditions with the same wave height and period have often been used to analyse the percentage of oblique waves needed to generate shoreline sand waves: two assumed to favour shoreline stability, $\theta = 30°$ and $\theta = -30°$, and two assumed to favour shoreline instability $\theta = 60°$ and $\theta = -60°$ (van den Berg *et al.*, 2012; Kaergaard & Fredsoe, 2013*b*). Nevertheless, the focus of these studies was theoretical and did not take into account a real wave climate (from now on referred to as RWC) as a starting point for building the synthetic wave climate (from now on referred to as SWC).

In this Chapter, a new way to design an AMN is explored that allows to take into account orientation, shape, and size (Section 4.2.1). This is validated by comparing its evolution with the one of the real ZM by forcing both with a 50-yr real wave climate based on 5-yr historical data (see Section 3.4). Once validated, the roles of the orientation, shape and volume, in the mega-nourishment evolution, are investigated (Section 4.3). Independently, the best procedure to create a SWC is investigated taking into account (i) the method to extract the representative wave condition of a wave series divided into sectors, (ii) the optimal number of sectors that represent a RWC, (iii) and the duration of each wave condition (Section 4.2.2). The real ZandMotor from January 2012 is used as the initial bathymetry (Fig. 3.2.2 in Section 3.2). Afterwards, the sensitivity of the ZM evolution to the probability of occurrence of the oblique wave sectors is investigated (Section 4.4). The simulations are performed with the Q2Dmorfo model.

4.2 Methodology

The simulations of the analytic mega-nourishment are done with the 50-yr real wave climate constructed from repeating ten times the wave data from 2010 to 2015 of the Europlatform buoy (see Section 3.4 for more details). The synthetic wave climate is extracted from the same wave data and the initial bathymetry used in those simulations is the measured ZandMotor in January 2012.

The morphological characteristics of the mega-nourishment that are computed in the long-term simulations are its diffusivity, its feeding capacity to adjacent coasts, its alongshore migration, and its shape asymmetry. The computation of the diffusivity assumes that the shoreline has a Gaussian shape (the details of the computation are explained on Section 3.3.3). The feeding performance of the mega-nourishment is measured by defining monitoring areas of equal size, located at both sides of the mega-nourishment. Then the beach linear metre is computed for every survey in each area (following Eq. 3.4.8). The area limits are such that they have a width of 2.5 km and begin where the perturbation initially affects the shoreline (see Fig. 4.2.1). The feeding asymmetry is defined by Eq. 3.4.9 (but instead of

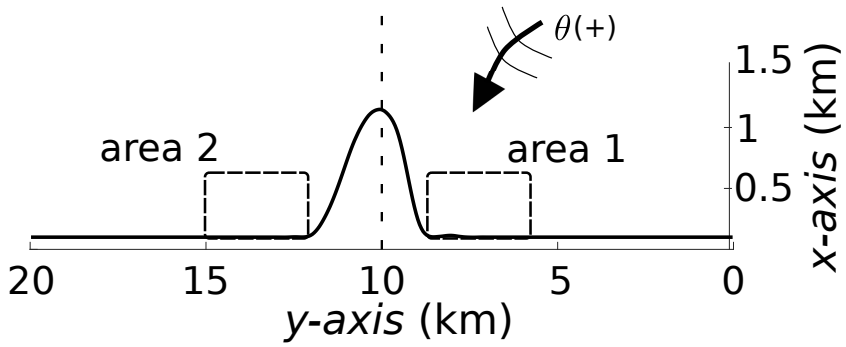

Figure 4.2.1: Sketch of the simulations. The wave angle θ indicated has a positive sign and the shape asymmetry is negative. The areas defined to compute the feeding asymmetry are marked with a dashed rectangle.

NE and SW, the equation refers to area 1 and area 2). Strictly speaking, the migration of the perturbation is complicated to compute because the shape of the shoreline changes continuously. Therefore, as an indication, the alongshore Gaussian displacement with respect to its initial location is computed by minimizing the error between a symmetric Gaussian and the shoreline. The shape asymmetry is computed with the same equation of the feeding asymmetry but the limits of the areas are defined by the lateral boundaries and the center of the adjusted Gaussian (i.e. from the dashed line in the middle of the mega-nourishment in Fig. 4.2.1 to the lateral boundaries of the domain). This implicitly assumes that the mega-nourishment influence is limited to the areas where there are shoreline changes. The SA is negative when the tip is oriented towards the negative y direction (as in Fig. 4.2.1).

The used model setup is practically the one obtained after the calibration of Section 3.3. The three most important parameters are (i) the factor in the wave-driven alongshore transport (parameter μ =0.04 $m^{1/2}s^{-1}$), (ii) the diffusivity factors $\vec{q_N}$ and $\vec{q_D}$ (parameter ν =0.05), (iii) and the depth of closure D_c (parameter $f_c = 0.15$). In some preliminary simulations the SWC had long periods of fair weather and then the f_c value of 0.15 could cause large amounts of sediment accumulation near the shore and, as a consequence, numerical instabilities arose. However, simulations with a slightly larger f_c value (of 0.20), not tested in Section 3.3.1 (only the values of 0.15, 0.25, 0.35 and 0.45 were tested), showed that using $f_c = 0.20$ the Brier skill score is lower at first but the performance improves in time and is even slightly better after three years than that obtained using $f_c = 0.15$. Therefore, a f_c value of 0.20 is chosen in this application. The alongshore length of the simulations, L_x, is of 20 km and the cross-shore length is of 4 km, with the mean shoreline (before applying the perturbation) located at x =600 m. Finally, the fact that the SWCs largest waves are lower than the storm waves found in the RWC allows to use a smaller time step. So, Δt =0.001 s is set in the SWC simulations and Δt =0.006 s is set in the AMN simulations. The rest of the setup values are those used in Chapter 3.

4.2.1 Design of an analytic mega-nourishment

The general form of a two-dimensional elliptical Gaussian function is used to perturb a bathymetry in equilibrium. The parameters of the Gaussian function are optimized with the submerged bathymetry of the ZandMotor from January 17 of 2012. The resulting dry beach is set to a constant berm thus arriving to a pseudo analytic perturbation. This is validated by comparing its evolution with the evolution of the real ZandMotor, both are forced with the RWC.

Construction of the analytic mega-nourishment

The perturbation of the ZM is obtained by subtracting the measured bathymetry from the idealized equilibrium bathymetry previous to the construction. The latter consists of a straight shoreline with parallel depth contours following the profile of Yu & Slinn (2003) adjusted to the real profile. Afterwards, the wet area is used to optimize the 2D-Gaussian function

$$f(x,y) = A\exp(-(a(x-x_0)^2 - 2b(x-x_0)(y-y_0) + c(y-y_0)^2)), \tag{4.2.1}$$

where

$$a = \frac{\cos^2\Theta}{2\sigma_x^2} + \frac{\sin^2\Theta}{2\sigma_y^2}$$

$$b = -\frac{\sin 2\Theta}{4\sigma_x^2} + \frac{\sin 2\Theta}{4\sigma_y^2}$$

$$c = \frac{\sin^2\Theta}{2\sigma_x^2} + \frac{\cos^2\Theta}{2\sigma_y^2}.$$

Here, x_0 and y_0 determine the center position, σ_y (σ_x) is the standard deviation of the alongshore (cross-shore) decay of the perturbation, Θ is the rotation angle, which controls the initial shape asymmetry (note that the initial ZM orientation Θ is negative), and A determines the height of the perturbation and therefore modules the perturbation in the alongshore and in the cross-shore. To reduce the number of variables in the optimization process, x_0 is fixed to the shoreline and y_0 explores a small distance near the center of the ZM. The rest of the Gaussian parameters are varied to optimize the depth RMSE of the measured ZM wet area. Once the best parameter values are obtained, the analytic perturbation is added to the idealized equilibrium bathymetry. However, the dry beach has 160% more sand than the dry beach of the ZM (all the volume differences are computed with respect to the ZM) and resembles a hill with a maximum height over 30 m. In order to have a consistent dry-sand volume, the berm (height of the dry beach) is set to 2 m. This berm height is obtained from averaging the dry beach height of the real ZM. The RMSE of this first approximation is 0.41 m: the dry volume difference is 5.7% and the wet volume difference is -7%. A last step is taken to diminish the dry and wet volume differences by slightly varying the Gaussian parameters obtained before. In particular, the amplitude (A) and both shape variables (σ_x, σ_y) are slightly varied but maintaining the aspect ratio ($\sigma_x/\sigma_y = cte$). This last step gives a slightly higher RMSE of 0.44 m: a dry volume difference of 0.1% and a wet volume difference of -0.01%. This is a reasonable compromise between the RMSE and

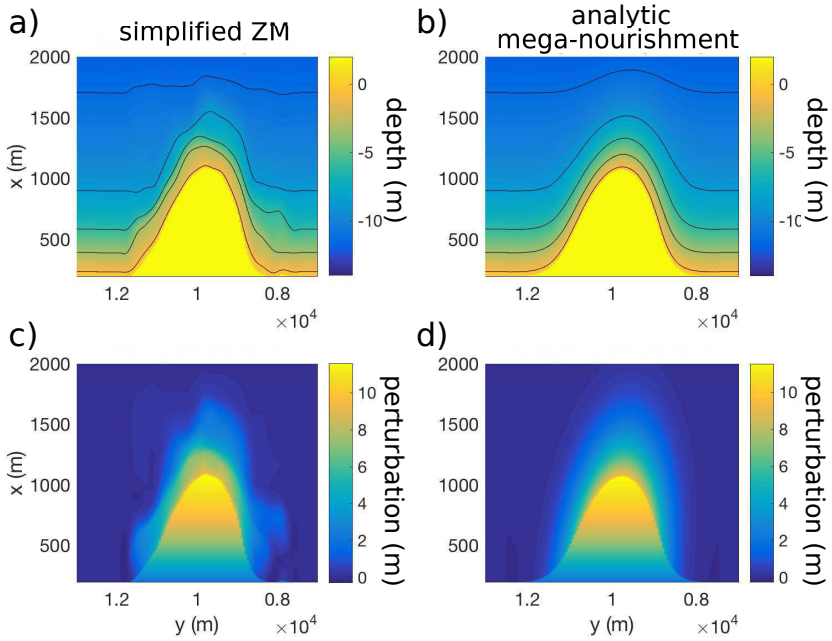

Figure 4.2.2: Simplified ZandMotor with the dry beach set to 2 m (a) and the analytic mega-nourishment (b). The associated perturbations can be seen in the lower panels.

the discrepancy in volume. The obtained values are $A = 36$ m, $\Theta = -53°$, $\sigma_x = 660$ m and $\sigma_y = 520$ m.

To further investigate the implications of assuming a constant berm, another initial bathymetry is modelled, corresponding to the measured ZandMotor but changing the dry beach to a berm height uniform of 2 m (Fig. 4.2.2a). The resulting most offshore dry point is located at 1080 m in the real bathymetry and at 1070 m in the analytic bathymetry. The associated bathymetric contours present similar amplitudes and reach similar offshore distances.

Validation of the analytic mega-nourishment

The performance of the previously obtained analytic perturbation (defined as case 3) is evaluated by comparing its evolution with the evolution of the original ZM (defined as case 1) and with the simplified ZM where the berm is set to 2 m (defined as case 2). These three perturbations are forced with the 5-yr RWC.

The amplitude decay of the three mega-nourishments present small differences (Fig. 4.2.3, left panel). The amplitude is almost identical during the first 5 years. Afterwards, case 1 slightly deviates from the other two cases. This long-term discrepancy appears to be caused

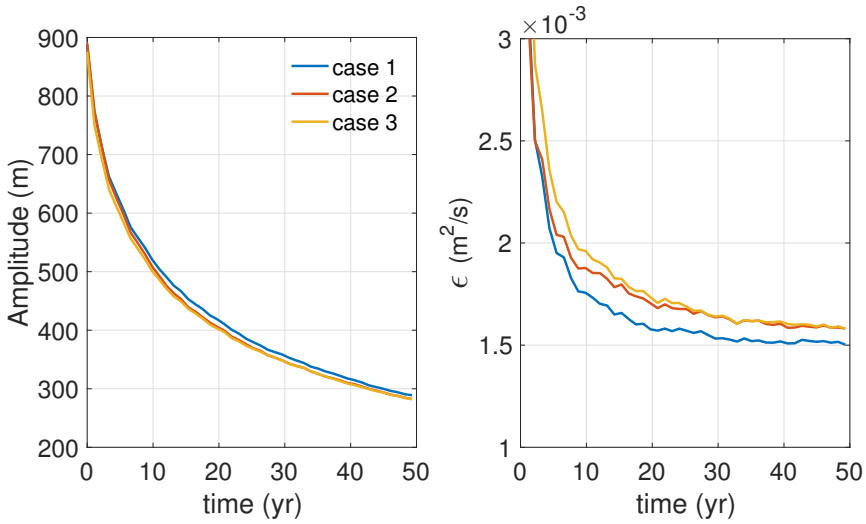

Figure 4.2.3: Predicted amplitude of the mega-nourishments (left panel) and the corresponding mega-nourishment diffusivity (right panel) over 50 yr. Case 1 is the ZM, case 2 is the simplified ZM with a uniform berm height, and case 3 is the analytic mega-nourishment.

by setting the dry beach to a uniform berm height. The diffusivity allows to identify with better detail the evolution of the perturbation (Fig. 4.2.3, right panel). At the beginning, the diffusivity of case 1 and case 2 are similar. After 5 years, the curve diffusivity of cases 2 and 3 tend to converge. Therefore, the medium-term discrepancy is attributed to the initial bathymetric differences and the long-term discrepancy is attributed to setting the dry beach to a constant berm. These discrepancies are small and the AMN (case 3) is considered to reproduce well the diffusivity of the ZandMotor since, at the end of the simulation, the AMN diffusivity is only 5% larger than the ZM diffusivity.

The diffusion of the mega-nourishment produces a widening of the perturbation and feeds the adjacent beaches, increasing the dry beach area. Fig. 4.2.4 (left panel) shows that the three cases feed more sand to area 1 than to area 2, i.e. the dry beach gained in area 1 is larger than the one gained by area 2. The feeding gap between the AMN (case 3) and the real ZM slightly increases in time, reaching a 6% difference after 50 years. Half of this difference is attributed to setting a constant dry beach (by seeing the differences with respect to case 2). This is more easily observed in the feeding asymmetry (Fig. 4.2.4, right panel). In the short-term the feeding asymmetry (FA) of cases 1 and 2 are practically equal. The three cases show a strong variability during the first 5 years due to the initially fast morphodynamic evolution. This trend will be observed in every simulation of this Chapter. After 20 years the FA of case 2 tends to the FA of case 3. Therefore, as occurs with the diffusivity, the short-tem differences are related to the initial bathymetric discrepancies and the long-term differences are related to using a constant dry beach.

The three perturbations migrate in the same direction (to the NE in the ZM coordinates,

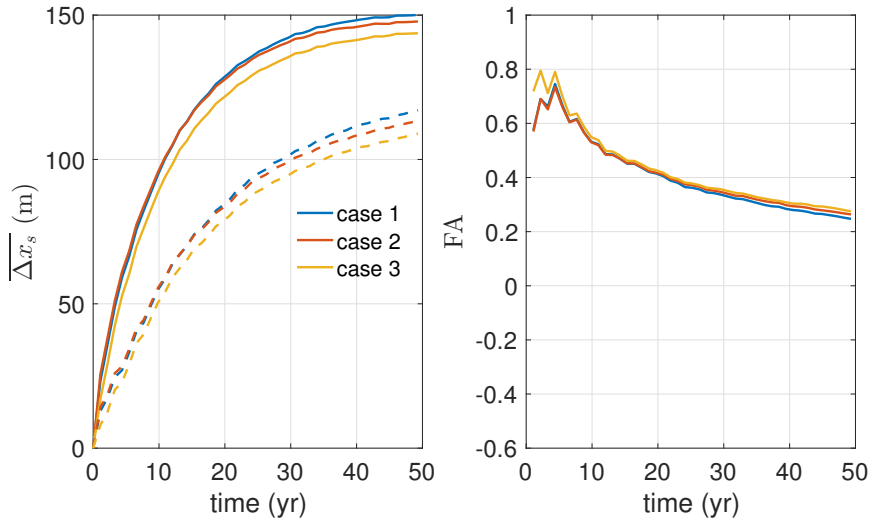

Figure 4.2.4: Beach linear metre gained in the defined sections along the coast area 1 (solid line) and the coast area 2 (dashed line) over 50 yr (left panel) and the associated feeding asymmetry over 50 yr (right panel).

see left panel of Fig. 4.2.5). After 12 years case 1 stops moving and the comparison with the behaviour of case 2 suggests that this is related to the dry beach configuration. The shape asymmetry, SA, is initially large as can be seen in Fig. 4.2.5 (and is also visible in Fig. 4.2.2). Afterwards, it decays fast and stabilizes around -0.01, such small value indicating that the shoreline shape is symmetric. The SA of the three cases does not differ significantly.

4.2.2 Design of a synthetic wave climate

In order to obtain a SWC that resembles the RWC, the shoreline evolution obtained with the former is compared with the one produced by the latter. A sensitivity to the wave statistics, number and duration of the bins, and to the randomness in the bin order is done. Then, the optimal SWC is analysed in detail by monitoring the produced diffusivity, feeding capacity, and shape asymmetry.

The default SWC is built out of the following four sectors: I) -90° to -45°, II) -45°to 0°, III) 0° to 45°, and IV) 45° to 90° (Fig. 4.2.6). The fifth sector (V) represents waves going offshore and therefore periods without morphological changes. The order of application of the sectors is random (hence, chronology effects are not studied) and the default bin duration is of 24 hours. The SWC is built respecting the probability of occurrence of the five sectors (Tab. 4.2.1).

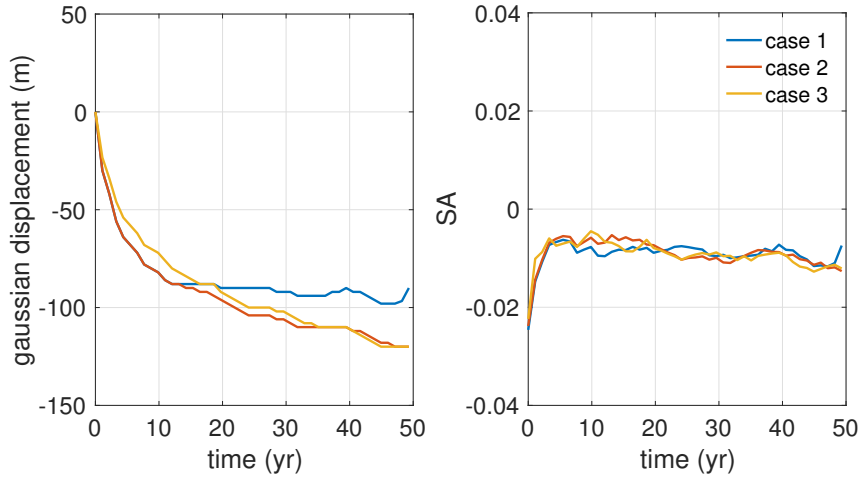

Figure 4.2.5: Gaussian displacement (left panel) and shoreline shape asymmetry, SA, (right panel) over 50 yr.

Table 4.2.1: Wave characteristics of the four sectors representing the real wave climate, where H is the significant wave height, T is the peak wave period, and θ is the wave direction measured with respect to the shore normal. The frequency of occurrence of each sector is written between brackets.

method\sector	I (33%)			II (11%)			III (27%)			IV(29%)		
	H	θ	T	H	θ	T	H	θ	T	H	θ	T
1	1.4	-74.2	5.8	1.3	-21.4	5.7	1.2	27.6	6.3	1.0	63.3	5.8
2	1.8	-76.5	7.0	1.7	-22.0	7.2	1.5	23.9	7.4	1.2	65.5	6.5
3	1.7	-72.3	6.8	1.6	-21.3	7.0	1.4	24.1	7.2	1.2	62.6	6.4
4	1.9	-76.7	7.2	1.8	-22.1	7.4	1.7	23.1	7.6	1.3	65.9	6.7

Sensitivity to wave statistics

From the real wave climate between January 2010 and January 2015, the representative wave characteristics (H, T, θ) are extracted for the four wave sectors (Tab. 4.2.1). Four methods are used: (1) simple average, (2) a weighted average with $H_s^{5/2}$, using the exponent of the CERC equation (Eq. 1.1.1), (3) a weighted average inferred from the wave-alongshore power (Eq. 3.4.7), and (4) a weighted average with H_s^3 (just as in Kaergaard & Fredsoe, 2013*b*). The obtained averaged wave conditions are fairly similar for every method, except for the simple average.

Fig. 4.2.7 shows the RMSE between the shoreline evolution obtained with the four SWC

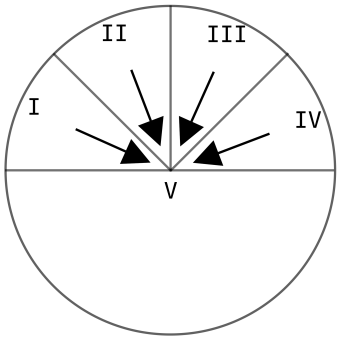

Figure 4.2.6: Rose sketch indicating five different sectors. The V sector represents waves seaward-directed and therefore periods without morphological changes.

and the RWC computed during 30 yr. The simple average (case 1) results in errors larger than 50 m after 10 yr. The wave conditions derived from the alongshore wave power (case 3) give small errors during the first five years but the error continues to increase. The difference between weighting the waves characteristics with $H_s^{5/2}$ (case 2) and with H_s^3 (case 4) is large despite the small difference in the power factor. The error strongly increases at the beginning when using H_s^3 and it stabilizes after 20 yr. The method based on weighting the wave characteristics with the power of the CERC equation has clearly the best performance. Although during the first three years the error is large, after 5 yr the RMSE decays and is stabilized at 10 m, which is in the order of the cross-shore cell size of 6 m. Considering that the initial amplitude of the ZM is around 1000 m, it is fair to say that this wave climate performs very similar to the RWC in the medium to long term.

Sensitivity to number of bins and duration

Here, the assumption that 4 wave sectors is enough to have a good representation of a real wave climate is challenged. For this, the process of creating a SWC is repeated with the previously found best weighting method (using $H_s^{5/2}$) but using several wave sectors (1, 2, 4, 8, 16, 32, 64). Using one bin produces large errors as well as using two sectors (Fig. 4.2.8). Interestingly, using four wave sectors results in a similar RMSE than using 8, 16, 32 and 64 wave sectors. The advantage of using 4 wave sectors comes from its simplicity, bimodality, and the possibility to grant purely diffusive properties to sectors II and III and anti-diffusive properties to sectors I and IV without losing accuracy.

The effect of the bin duration is tested by building SWCs of 6, 12, 24, 48, and 96 hr. Fig. 4.2.9 suggests that low duration values do not affect the morphological prediction but a large bin duration can cause slightly larger RMSE. In this study, a 24-hr bin duration is chosen as default because this is a typical duration of a storm.

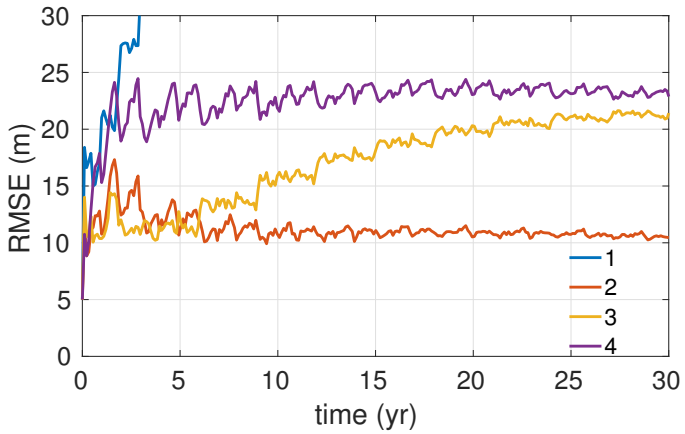

Figure 4.2.7: Root-mean-squared error between the shoreline computed using the RWC and the four SWC during 30 years.

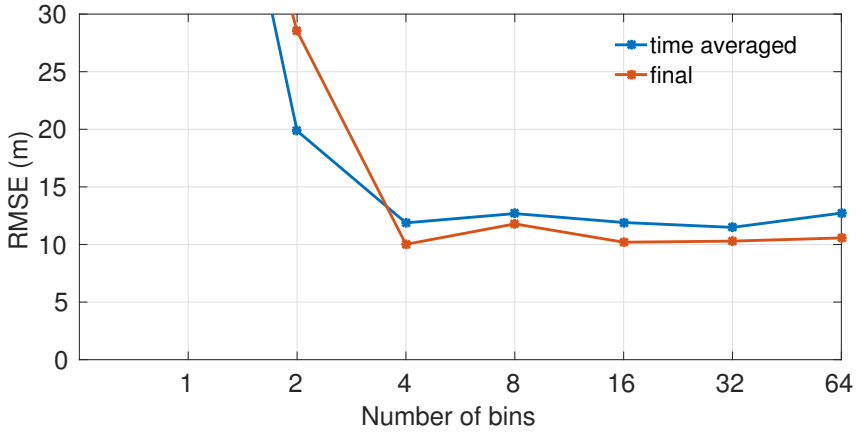

Figure 4.2.8: Time-averaged RMSE over 30 yr and final RMSE of the shoreline computed with SWCs divided in different number of sectors.

Sensitivity to randomness in bin order

Here, the randomness in the order of bin application is analysed in a simple way. Five SWCs are built by using the method 2 to extract the representative wave conditions of four sectors and a 24-hr bin duration with different (random) bin order, respecting the probability of occurrence of the five sectors. Fig. 4.2.10 suggests that the final RMSE has a 2-m variability associated to the randomness. The averaged RMSE has a 3-m variability, suggesting that

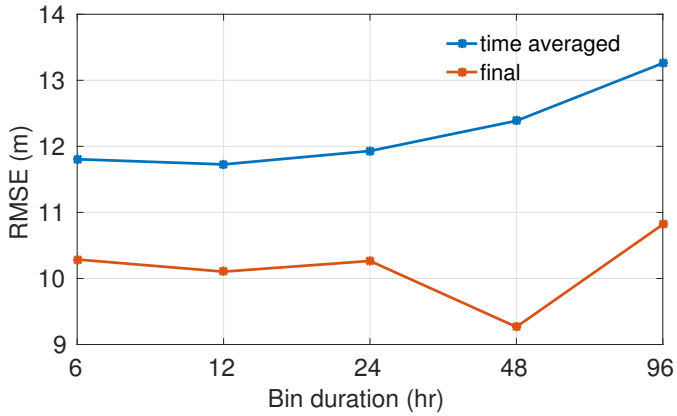

Figure 4.2.9: Time-averaged RMSE over 30 yr and final RMSE of the shoreline computed with SWCs of different bin duration.

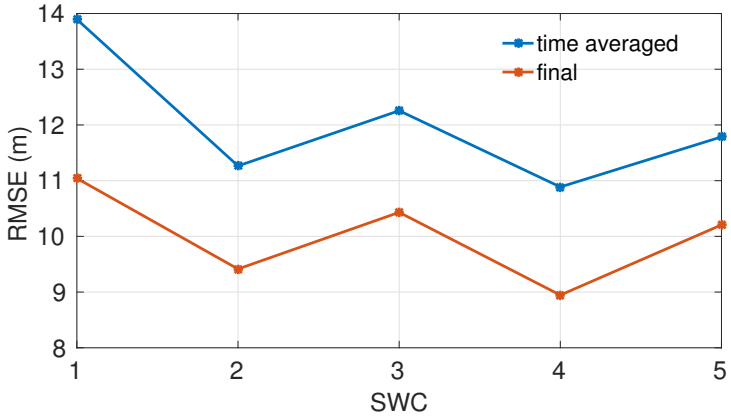

Figure 4.2.10: Time-averaged RMSE over 30 yr and final RMSE of the shoreline computed with SWCs of the same characteristics but different random bin order.

the randomness is more influential in the short term. This variability is lower than the cross-shore cell size of 6 m.

Validation of the SWC

The sensitivity analysis performed above showed that a SWC consisting of four bins (plus the non-morphological change bin) with a 24-hr duration and computing the averages with

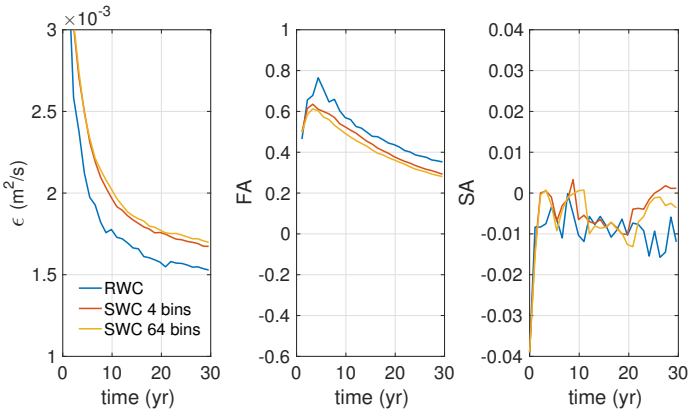

Figure 4.2.11: Diffusivity (left panel), feeding asymmetry (center panel) and shape asymmetry (right panel) during 30 yr produced by the RWC and the SWC using 4 bins and 64 bins.

method 2 ($H_s^{5/2}$ weighting) is the optimal way to reproduce in a simple way the RWC. To validate in detail its performance, the evolution of the ZM over 30 yr is computed with the SWC and with the RWC. The diffusion, feeding asymmetry, migration and shape asymmetry of the optimal SWC are now compared with those of the RWC.

The diffusion produced by the SWCs is 10% larger than the one produced by the RWC (Fig. 4.2.11). Also, the feeding asymmetry is 20% smaller at the end of the simulations and both FA are positive, with the implication that the mega-nourishment side with the initial larger shoreline slope feeds more sand to the adjacent beach. The shape asymmetry is slightly different after 20 years but the small values produced by both the RWC and the SWC mean that the shoreline is almost symmetric. Finally, the diffusivity, FA, and SA of the 64-bins SWC (also shown in Fig. 4.2.11) confirms that using more than 4 bins does not improve the performance of the SWC.

4.3 Effect of varying the mega-nourishment shape

4.3.1 Sensitivity to the initial asymmetry

The effect of the mega-nourishment initial asymmetry into its long-term evolution is studied by changing the rotation angle Θ of the AMN (Eq. 4.2.1), keeping the volume constant. The angle is varied from -60° to 60° with steps of 15°. This slightly changes the volume of the perturbation so in order to maintain the volume constant, A and σ_x are varied (maintaining the same shape ratio, σ_x/σ_y).

Fig. 4.3.12, left panel, shows that a symmetric perturbation would be slightly less dif-

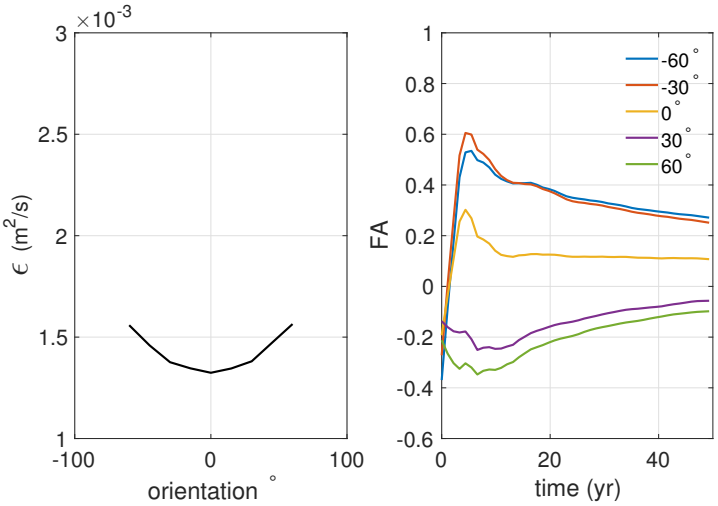

Figure 4.3.12: Diffusivity inferred from 50-yr simulations (left panel) and the FA during 50 years (right panel) for perturbations with different orientations.

fusive than a perturbation with rotation. However this difference is small, the amplitude difference between the scenario with a rotation of 0 degrees and the scenario with a rotation of 60 degrees is of only 10 m after 50 years. Given the scales of the perturbation and the differences between the simulations, it can be considered that the diffusivity is robust to the orientation of the perturbation. However, the initial orientation has a larger impact on the feeding asymmetry (Fig. 4.3.12, right panel). First, the Θ =0° scenario indicates that part of the feeding asymmetry is due to the wave climate (slightly dominated by waves with negative incident angles). Second, the initial orientation can enhance this asymmetry (negative angles) or diminish it (positive angles). The significant differences of the absolute values of FA between positive and negative orientations is again due to the wave climate. The impact of the initial orientation can have long term effects since the FA for positive orientation angles still remains negative (although small) after 50 yr.

Regarding the mega-nourishment migration, the long-term trend is independent of the initial orientation angle (Fig. 4.3.13, left panel). The mega-nourishment moves towards the negative y-axis and with similar rates for the five cases. However, during the first 5 years the migration is controlled by the initial orientation angle. This initial migration is due to the strong diffusion occurring in the side with the largest shoreline slope. The shape asymmetry values are very low for every scenario but the wave climate ends up causing negative SA values in the long term (Fig. 4.3.13 right panel).

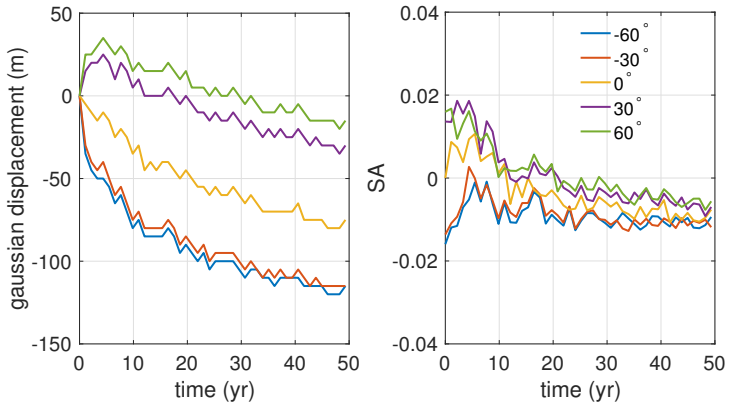

Figure 4.3.13: Gaussian displacement (left) and shape asymmetry (right) for different orientations of the perturbation over 50 yr.

4.3.2 Sensitivity to shape ratio

The original shape ratio of the perturbation, controlled by σ_x/σ_y, is here modified with a factor ranging from 0.25 up to 2 every 0.25 of the original one. Nevertheless, the shoreline slopes of the perturbed beach are highly sensitive to this change (i.e. the asymmetry) even though the perturbation orientation is the same. For this reason, the orientation is set to 0°, which also helps to further isolate the role of the shape ratio. The volume is kept constant by modifying σ_x and A. The symmetric perturbation is wider for smaller shape ratios. For example, the mega-nourishment has an amplitude of about 500 m for the case with a shape ratio 75% smaller than the original one (factor of 0.25).

The amplitude for high factors (above 1.25) reach similar values quite fast and the difference becomes imperceptible after 20 yr. However, the diffusivity is more sensitive to the shape since it also depends on the initial perturbation width. The diffusivity is smaller for larger shape ratios with an exponential decay (Fig. 4.3.14, left panel). The initial variability in the feeding asymmetry is larger for the more concentrated nourishments (higher shape ratio), which is probably due to the initially larger shoreline slopes (Fig. 4.3.14, right panel). The long-term feeding asymmetry tends to be slightly positive even for wide nourishments with a small amplitude.

The Gaussian displacement is negative for every scenario and the displacement rate is larger for more localized nourishments (Fig. 4.3.15, left panel). As occurs with the FA, the variability of the shape asymmetry is larger during the first 5 years for higher shape ratios. This initial noise fades in time tending to similar small values for the five cases (Fig. 4.3.15, right panel).

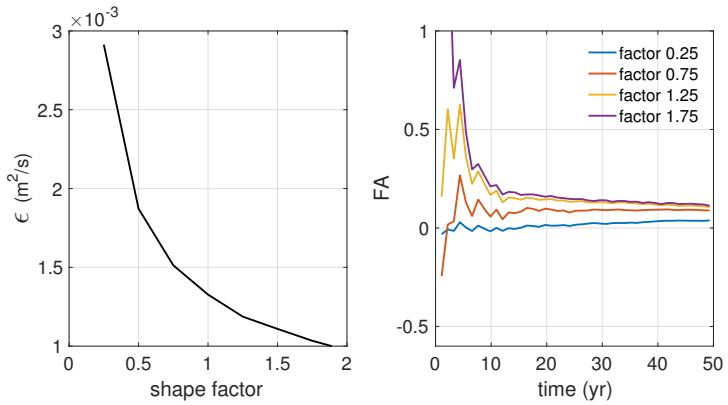

Figure 4.3.14: Diffusivity inferred from 50-yr simulations (left panel) and feeding asymmetry for different shape ratios of the perturbation over 50 yr (right panel).

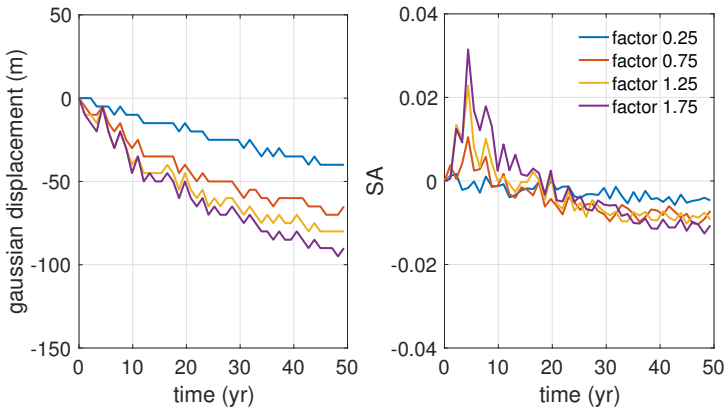

Figure 4.3.15: Gaussian displacement (left) and shape asymmetry (right) for different shape ratios over 50 yr.

4.3.3 Sensitivity to volume

The amplitude of the perturbation A is varied together with σ_x to change the mega-nourishment volume. In this scenarios, the orientation of the perturbation and the shape ratio (σ_x/σ_y) are maintained equal to the ones of the default case. The original volume of the ZM is modified with a factor ranging from 0.25 to 2 every 0.25.

As expected, the initial amplitude of the perturbation is larger for larger volumes. Fig. 4.3.16 (left panel), shows that the diffusivity is larger for lower volumes than the original

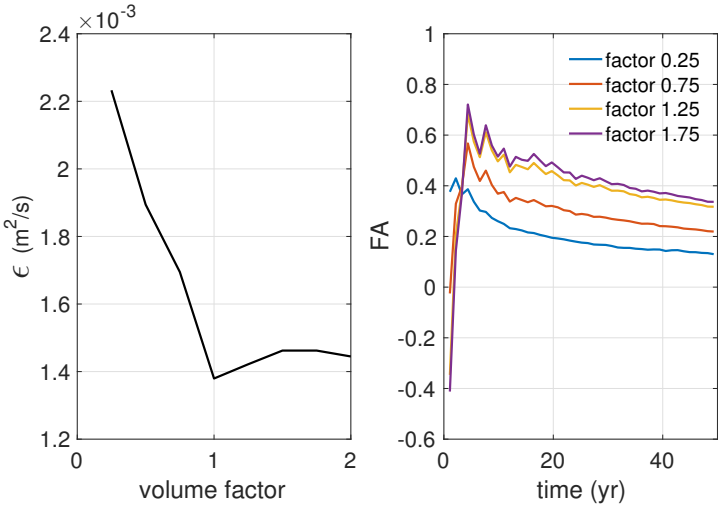

Figure 4.3.16: Diffusivity inferred from 50-yr simulations (left panel) and feeding asymmetry for different volumes of the perturbation over 50 yr (right panel).

volume and stabilizes for larger volumes. The long-term feeding asymmetry is higher for larger volumes (Fig. 4.3.16, right panel).

The smallest nourishment migrates slower than the other three cases (Fig. 4.3.17, left panel) and no clear difference can be seen between the two larger mega-nourishments. The shape asymmetry does not seem to be sensitive to the sand volume since all scenarios present variations around -0.0075 (Fig. 4.3.17, right panel).

4.4 Effect of varying the wave forcing

4.4.1 Design of SWC with different obliquity occurrence

The obtained parameters of the synthetic wave climate in Section 4.2.2 are used to create two different set of simulations, in which the probability of occurrence of the four different wave sectors is varied to study the effect of varying the occurrence of high-angle waves. First, sectors I and IV are considered to belong to the oblique waves category and their combined probability is $p_O = p_I + p_{IV}$. In the real wave climate, $p_O \simeq 0.6$ and this value is varied from 0 to 1 in steps of 0.1 in the first set of simulations. This is done by increasing/decreasing p_I and p_{IV} (keeping their ratio) and decreasing/increasing p_{II} and p_{III} (also keeping their ratio) (see Fig. 4.4.18, above panel). In the second set of simulations, only p_I is increased while the other three are decreased (keeping their ratios), so that p_O changes from 0.6 to 1 every 0.05 (Fig. 4.4.18, lower panel). Therefore, the first set of simulations has a bimodal

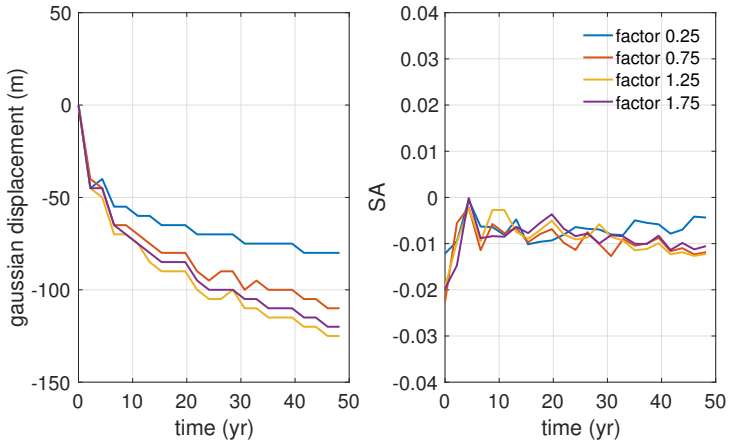

Figure 4.3.17: Gaussian displacement (left) and shape asymmetry (right) for different volumes of the perturbation over 50 yr.

wave climate with different degrees of obliquity whilst the bimodality in the second set of simulations decreases with increasing obliquity. The probability of occurrence of the fifth sector p_V (i.e. the one that does not produce morphological changes), of about 20%, is kept unchanged.

4.4.2 Effect of obliquity occurrence in mega-nourishment dynamics

For wave climates with a large percentage of high-angle waves ($\geq$ 80%), erosion areas are formed at the sides of the mega-nourishment (Fig. 4.4.19), which is the initial stage in the HAWI instability (van den Berg *et al.*, 2011). In the first set of simulations, after 50 years the 100% case of oblique waves shows a maximum erosion of 150 m at y =6.5 km. In the second set of simulations, the run with 100% of oblique waves crashes after 40 years because at this moment all the initial dry beach (of 600 m) is eroded at y =6.5 km. The diffusivity decays linearly with an increasing percentage of wave obliquity in the SWC (Fig. 4.4.20). The decay is slightly larger for the second set of simulations, where only the occurrence of sector I increases. This might be related with the fact that this sector contains more energetic and oblique waves than sector IV. However, for SWCs with a large percentage of high-angle waves ($\geq$ 80%) the inferred diffusivity might be invalid because of the erosion areas formed in the sides of the mega-nourishment, which deviates the shoreline shape from a Gaussian function and thus renders invalid the supposition taken to infer the diffusivity. Indeed, the obtained diffusivity in these cases should be $\epsilon < 0$ (Falqués & Calvete, 2003; Ashton & Murray, 2006*a*).

It can be seen that the feeding asymmetry is larger for the scenarios with larger wave obliquity (Fig. 4.4.21, right panel). This might be related to the fact that the Sector-I waves

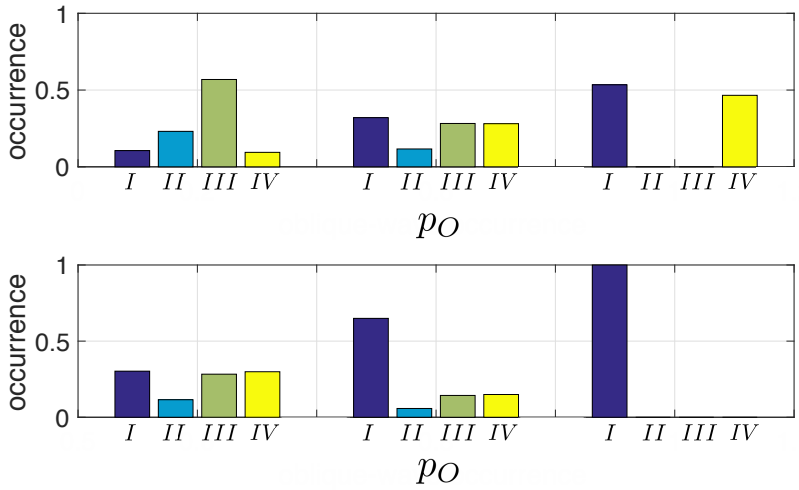

Figure 4.4.18: Probability of occurrence of the four Sectors for defined oblique waves occurrence. The upper panel assumes that Sectors I and IV are modified proportionally and the lower panel assumes that only the probability of occurrence of Sector I increases.

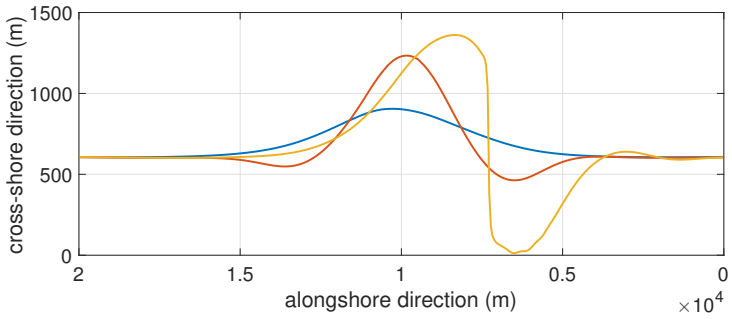

Figure 4.4.19: Shorelines after 40 yr of evolution. The blue shoreline is forced with a 60% oblique bimodal wave climate, the red shoreline is forced with a 100% oblique bimodal wave climate, and the orange shoreline is forced with a a 100% oblique uni-modal wave climate.

are more energetic than the Sector-IV waves. At the same time, the feeding rate is smaller for larger obliquity because the diffusivity decreases (Fig. 4.4.21, left panel). The strange behaviour of FA in the 100% wave obliquity case is due to the erosion areas formed from the beginning at the sides of the mega-nourishment. The long-term migration of the mega-nourishment is controlled by the percentage of oblique waves (Fig. 4.4.22, left panel). For small p_O, the sector III is dominant (Fig. 4.4.18, above panel) and the mega-nourishment strongly migrates to the positive y-axis. For large p_O, sector I is slightly more frequent than

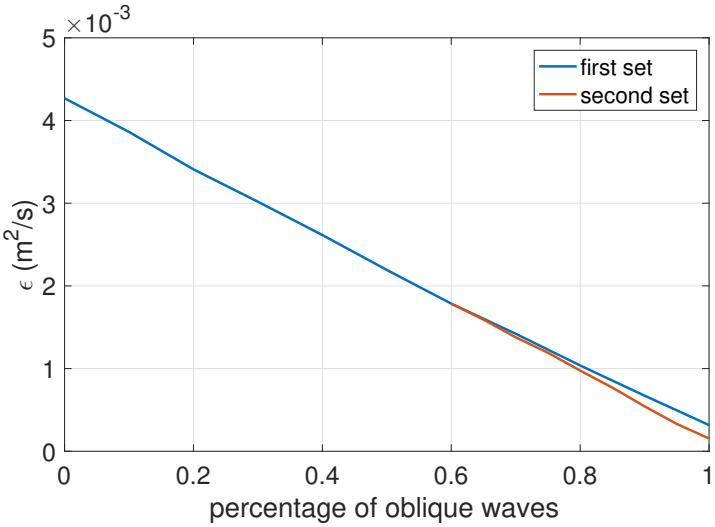

Figure 4.4.20: Averaged diffusivity over the last 5 years of simulations in function of wave obliquity occurrence. The blue line corresponds to the first set of simulations and the red line to the second set of simulations.

sector IV (and the former is more energetic and with a higher incidence angle) so migration to the negative y-axis is observed. Notice that the short-term migration is the same for every climate because it is controlled by the initial mega-nourishment shape asymmetry. The Gaussian displacement and the shape asymmetry present an important correlation in the long term (Fig. 4.4.22). The larger the negative displacement is, the larger the shape asymmetry is.

In the second set of simulations, the behaviour of FA when increasing only the occurrence of sector-I waves is more complex (Fig. 4.4.23). Actually, after only increasing the wave obliquity (p_O) to 70%, the FA remains constant at around 0.5 instead of decreasing as in all the previous situations. For larger oblique percentages (p_O), the FA increases continuously in time. The behaviour of the FA in this set of simulations is more complex because it is not only influenced by the diffusivity and the erosion areas (as for the first set of simulations) but also by an increasingly strong migration of the mega-nourishment. Indeed, the mega-nourishment strongly migrates to the negative y-axis for cases with more than 80% of oblique waves (Fig. 4.4.24, left panel) because the wave climate is dominated by sector-I waves. The Gaussian displacement and the SA show again a strong correlation (Fig.4.4.24, right panel) so the SA is very large for the very oblique wave scenarios. Notice that both the migration and SA experience strong increments when increasing the percentage of obliqueness from 80% to 100%.

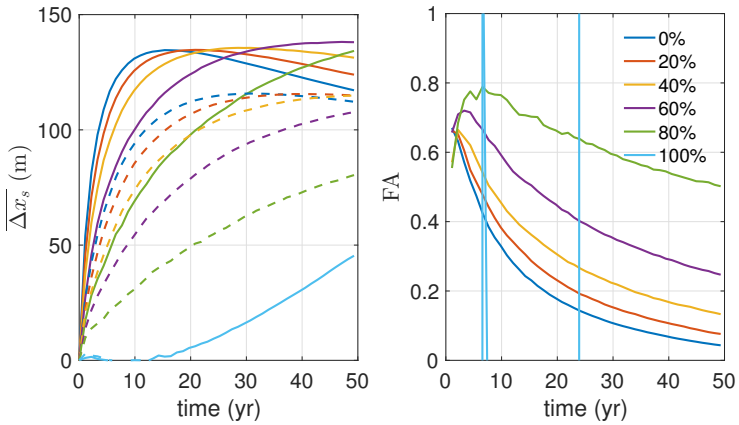

Figure 4.4.21: Beach linear metre gained in the defined sections along the coast area 1 (solid line) and the coast area 2 (dashed line) over 50 yr (left panel) and the associated feeding asymmetry over 50 yr (right panel). These curves correspond to the percentage of oblique waves of the first set of simulations.

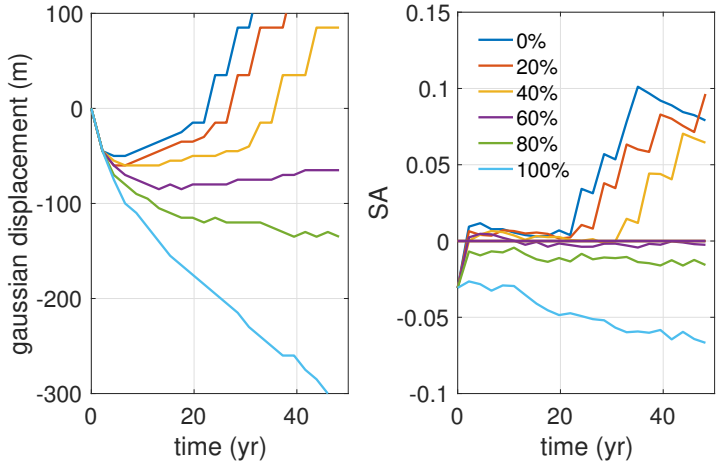

Figure 4.4.22: Gaussian displacement (left panel) and shoreline shape asymmetry (right panel) for the first set of simulations over 50 yr.

4.5 Discussion and conclusions

The 50-yr evolution of an analytic mega-nourishment, constructed with a 2D-Gaussian bed level perturbation, has been compared with the evolution of the ZandMotor. Both cases have

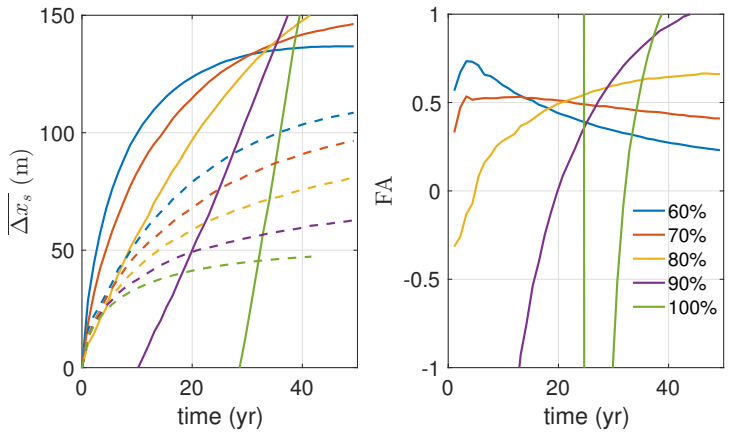

Figure 4.4.23: Beach linear metre gained in the defined sections along the coast area 1 (solid line) and the coast area 2 (dashed line) over 50 yr (left panel) and the associated feeding asymmetry over 50 yr (right panel). These curves correspond to the percentage of oblique waves of the second set of simulations.

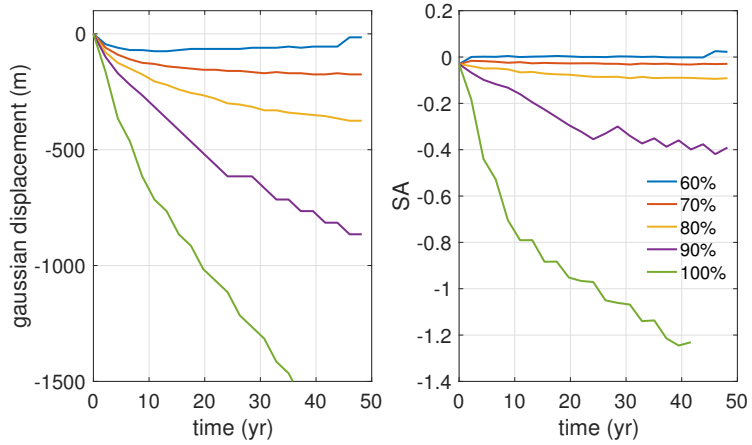

Figure 4.4.24: Gaussian displacement (left panel) and shoreline shape asymmetry (right panel) for the second set of simulations over 50 yr.

been computed with the Q2D-morfo model and the same real wave climate. Since the AMN has the same berm height in the dry beach, a simplified ZM with the same berm height has also been modelled. In order to quantify the performance of the mega-nourishments four characteristics have been examined: the diffusivity, the feeding capacity, the alongshore Gaussian displacement, and the shape asymmetry. The diffusivity of the AMN and the

simplified ZM is 10% larger than the one of the real ZM after 20 years of simulation and this difference was maintained over the next 30 years. The feeding asymmetry of the AMN is 20% larger than the one of the ZM during the first 3 years. Afterwards, the three FA curves reach similar values with only a 5% difference. The shape asymmetry of the 3 perturbations do not show significant differences. However, the Gaussian displacement of the real ZM starts deviating after 20 years from the other two cases. In general, the short-term differences are attributed to the discrepancies in the wet beach while the long-term differences are attributed to the assumption of a constant berm height in the AMN. Therefore, these findings show that a 2D-Gaussian perturbation can be used to mimic real mega-nourishments such as the ZandMotor and that the dry beach design is relevant for the long-term behaviour of the mega-nourishment.

The role of the AMN shape on its own evolution has also been analysed by varying its asymmetry, the shape ratio and the volume. The shape asymmetry is varied using the orientation of the 2D-Gaussian function. It turns out that it has little relevance on the diffusivity but it has a large influence on the feeding asymmetry, determining its sign in the short and in the long term (over 50 years). A symmetric perturbation with a 0° orientation, still has a FA value of 0.1, which can be attributed to the wave climate. The rest of the FA value is due to the initial orientation design. The long-term alongshore displacement shows the same rate (typically small) and direction (to the negative y-axis) for all the orientations but during the first 5 years the displacement follows the orientation sign. In the same line, the SA sign follows the sign of the orientation in the short term but in the long-term the SA curves tend to similar values for all orientations. The second parameter studied, the shape ratio (i.e. the ratio of the standard deviations of the Gaussian), has been tested using an orientation of 0°. The original shape ratio, obtained after the optimization of the AMN to mimic the ZM, is modified from a fourth of the original value until doubling it. Its principal effect is seen on the diffusivity: for wider perturbations the diffusivity is larger (the widest perturbation doubles the diffusivity of the narrowest perturbation) and vice versa. This suggests that the larger cross-shore amplitude of the depth contours linked to the narrower perturbations (more localized) produce larger perturbations in the wave field. This in turn diminishes the diffusivity and enhances the processes leading to HAWI. The FA is smaller for wider perturbations, practically 0 for the widest one. The Gaussian-displacement rate is smaller for wider perturbations and the SA values have a similar behaviour at first. However, the SA reaches similar values at the end of the simulations (for all shape factors). The initial volume size has a similar impact as the shape ratio: for smaller nourishments the diffusivity was larger but this trend is not observed for larger volumes than the original one. Both the FA and the Gaussian displacement are in general smaller for smaller nourishments. The volume size seems to have no impact in the SA.

In order to study the role of wave obliqueness on mega-nourishments, the real wave climate has been reduced to a few representative wave conditions defined by different wave incidence sectors, creating a synthetic wave climate. It has been found that the best way to extract the representative wave condition of each sector is by averaging the waves with its significant wave height to the 5/2 power, i.e. following the power in the CERC equation. Also, the number of bins necessary to represent the real wave climate has been tested. It is found that four wave conditions, two representing nearly shore-normal waves and two representing oblique waves, are optimal for representing the wave climate and that adding more wave conditions do not improve the performance of the SWC.

To study the influence of wave obliquity, the probability of occurrence of high-angle waves ($\theta > 45°$) has been varied in two different ways. In the first set of simulations, the frequency of occurrence of high-angle waves coming from the two sides has been varied (i.e. keeping the bimodal nature of the RWC). In the second set of simulations, only the frequency of occurrence of high-angle waves from one side is incremented (tending to an unimodal wave climate). The SWC with more than 80% of high-angle waves produce erosional hotspots at both sides of the mega-nourishment. This phenomena was linked to HAWI by van den Berg *et al.* (2011) and it was the first phase of the triggering of shoreline sand waves. However, the simulation time of 50-yr of the present work was not large enough to develop a full train of sand waves. The percentage of high-angle waves (80%) needed to trigger the instability agrees with the studies of van den Berg *et al.* (2012); Kaergaard & Fredsoe (2013*b*) but not with the more idealized model predictions of Ashton & Murray (2006*b*). The diffusivity produced by the SWCs is found to be linearly inverse to the proportion of oblique waves. However, for SWC with more than 80% of oblique waves the diffusivity inferred is not reliable because the shoreline does not follow a Gaussian shape and the diffusivity computation is not valid. The behaviour of FA, alongshore migration, and SA is significantly different in the bimodal and unimodal scenarios. In the former case, the FA is larger for more oblique wave climates. This means that the waves incoming from sector I are largely responsible for the FA of the mega-nourishment. The FA shows an odd behaviour for wave climates with a percentage of high-angle waves above 80% due to the erosional hotspots formed at the sides of the perturbation. The alongshore Gaussian displacement is in the same direction (negative y-axis) for every SWC during the first four years. This initial migration is due to the mega-nourishment shape asymmetry. For SWC with a frequency of high-angle waves lower than 60%, the mega-nourishment starts to migrate in the opposite direction because sector-III waves become dominant. In the second set of simulations (unimodal scenarios), the FA starts to behave differently quite fast. If the frequency of high-angle waves is larger than 70% the FA increases, and when this frequency is larger than 80% the formation of hotspot has a strong influence on this parameter. Mega-nourishment migration changes dramatically when the frequency of high-angle waves is high, and this effect is exponential. After 50 years, the displacement is of 800 m in case of 90% of high-angle waves and of 2 km in case of 100% of high-angle waves. The SA follows the same behaviour as the Gaussian displacement.

The results of this chapter allow to make recommendations about the optimal design of future mega-nourishments. According to the obtained results (Fig. 4.3.16, left panel), a volume of sand such as the one used in the construction of the ZandMotor optimizes its diffusivity (i.e. the diffusivity is the lowest). The shape ratio can be varied to modulate the diffusivity: narrow mega-nourishments are less diffusive than wide ones. The asymmetry in the mega-nourishment feeding to adjacent beaches is mainly controlled by the initial shape asymmetry. This effect is important in the long term and it is more pronounced for larger mega-nourishments. Finally, a warning must be made regarding the wave obliquity. The wave climates with a percentage of high-angle waves occurrence larger than 80% can cause erosional hotspots in the sides of the mega-nourishment. These erosional hotspots become more and more pronounced with slight increments of that percentage. In particular, wave climates dominated by high-angle waves coming from one side of the mega-nourishment (i.e. tending to be unimodal) develop faster the erosional hotspots than bimodal wave climates. The migration of the mega-nourishment in such situation can also become dramatic.

Chapter 5

Formation of shoreline sand waves

5.1 Introduction

The potential for shorelines to develop high-angle wave instability has been amply confirmed by mathematical modelling during the last two decades. These studies focus on the physics of the basic positive feedback (Ashton *et al.*, 2001; Falqués *et al.*, 2017), the bathymetric and wave conditions which are prone to the instability (Falqués & Calvete, 2005; Idier *et al.*, 2017), its characteristic length scale (van den Berg *et al.*, 2014) and its finite amplitude development (Ashton *et al.*, 2001; Ashton & Murray, 2006*a*; van den Berg *et al.*, 2012; Kaergaard & Fredsoe, 2013*a*). Also, the proportion of high-angle waves in the wave climate which is necessary to trigger HAWI has been investigated. The highly idealized model of Ashton *et al.* (2001) predicts a 50% while more realistic models require up to 80% of high-angle waves (van den Berg *et al.*, 2012; Kaergaard & Fredsoe, 2013*a*).

However, testing HAWI as the origin of Kilometric-Scale Shoreline Sand Waves (KSSW) in nature is more difficult. It has been well substantiated that KSSW tend to occur along coasts where the wave climate is dominated by high-angle waves. The cases of some elongate water bodies (Ashton *et al.*, 2009), Lake Erie (Davidson-Arnott & van Heyningen, 2003; Ashton & Murray, 2006*b*) or the west coast of Africa (Kaergaard & Fredsoe, 2013*b*; Idier & Falqués, 2014) are quite clear. Other less conclusive examples include the case of the west Danish coast (Kaergaard *et al.*, 2012; Falqués *et al.*, 2017), the Carolina capes (Ashton *et al.*, 2001; Ashton & Murray, 2006*b*), the Dutch coast (Ruessink & Jeuken, 2002; Falqués, 2006) and the eastern gulf of Finland (Ryabchuk *et al.*, 2011). However, all these cases concern already fully formed features while observations of the initiation (or the destruction) moments are very scarce. An important reason is that such tests require detailed measurements of the

This chapter is largely based on Arriaga *et al.* (2018*a*): Arriaga, J., Falqués, A., Ribas, F. & Crews, E. 2018*a* Formation events of shoreline sand waves on a gravel beach. *Ocean Dynamics* **68** (6), 735–748

bathymetry and the wave conditions at the moment of their formation from a featureless morphology.

Dungeness is a cuspate foreland located in the eastern English Channel and formed by a mix of sand and gravel. This cape has been growing during the last two millennia and it is a highly dynamic geologic system, which still presents a trend to grow and migrate towards north (Long *et al.*, 2006). At the northern flank, which trends roughly SSE-NNW, shoreline undulations with a wavelength ∼400 m sometimes develop. The wave climate at this coast is bimodal, with main wave directions from the south-west (SW) and from the north-east (NE). The dominant SW waves are very oblique with respect to the northern flank while the NE waves are between shore normal and moderately oblique. According to the HAWI hypothesis the SW waves have the potential to trigger KSSW while the NE waves could sometimes favour the growth, sometimes inhibit it. Thus this coast is a potential site to test the HAWI hypothesis. The investigation of these undulations at Dungeness is relevant not only from a geomorphological point of view but also because they produce erosional hot spots in the embayments. Moreover, the most recent work explaining the formation of the Dungeness Foreland (Lewis, 1932; Eddison, 1983) is not entirely satisfactory, and understanding the formation of the shoreline undulations and the role of high-angle waves can provide insight into the dynamics of the whole foreland.

This chapter focuses on two goals: (i) to present a new kilometric-scale shoreline sand waves site by characterizing the events of formation, and further development of the shoreline undulations at Dungeness and (ii) to test the HAWI hypothesis for the formation of these KSSW by investigating the possible correlation between the KSSW events and both the propagated wave conditions and the output of a linear morphodynamic model. The observations are first presented and the shoreline waviness is quantified using the Discrete Fourier Transform (Section 5.2). Subsequently, the measured 10-year wave conditions are propagated from an available buoy (located at 43-m depth) up to 4-m depth in front of the features, using the SWAN model (Booij *et al.*, 1999) (Section 5.3.1). Then, the dominance of high-angle waves over low-angle waves is correlated with the presence of shoreline sand waves (Section 5.3.2). Afterwards, the 1Dmorfo model (described in Chapter 2.3) based on linear stability analysis (Falqués & Calvete, 2005) is used to compute the initial growth rates of the relevant wavelengths using the propagated wave conditions as model input (Section 5.3.3). Finally, the results are discussed in Section 5.4 and the most important conclusions are listed in Section 5.5.

5.2 Observations

5.2.1 Site

Dungeness is the largest cuspate foreland of the southern English shore (Fig. 5.2.1) and, together with the adjacent areas, form a shingle system of 37 kilometres of coastline (from Winchelsea at the south-west to Hythe at the north-east). This shingle system forms a coastal barrier protecting several marshes (McGregor & Green, 1989). Actually, the name Dungeness is derived from the Denge marsh and the nose-shape (or "ness") of the protecting

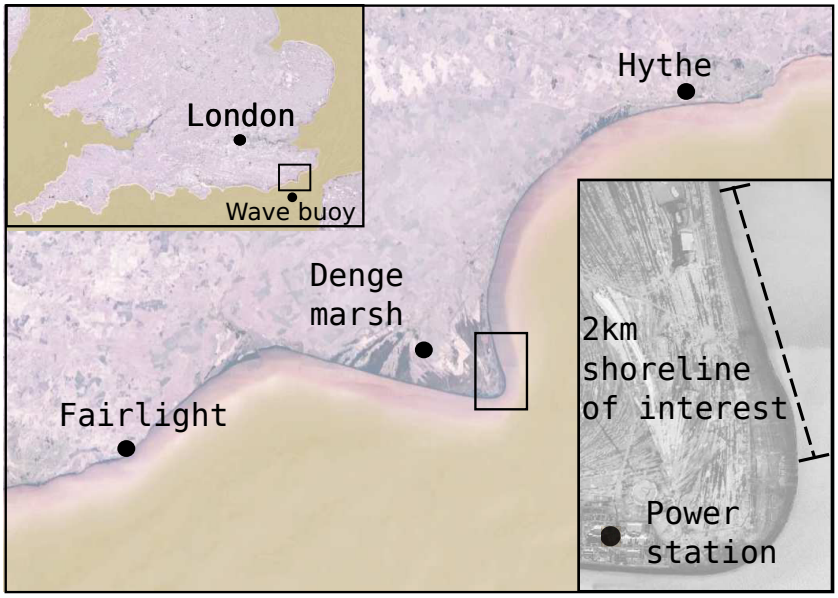

Figure 5.2.1: Location map with a zoom in the particular area of interest. The satellite images are taken from Google Earth and correspond to September 2013.

shingle shore (Redman, 1882). The foreland was already present back in the year 300-400 A.D., and it has been growing and migrating towards north-east since then (Long *et al.*, 2006). Thereby, the south-west (north-east) flank shows an eroding (accreting) long-term trend. The area studied in this contribution is the 2-km long coastline at the north-east flank of the foreland (see Fig. 5.2.1), which has an average shoreline orientation of $\sim 170^\circ$ with respect to north. The shingles in our area of interest, with a mean grain size varying between 10 mm and 20mm, can be classified as gravel sediment (Dornbusch, 2003-2005). The beach foreshore in this area is steep, consistent with the large grain size, with a mean intertidal beach slope of 0.08. The slope is largest at the tip of the cape and decreases northward. The region is macrotidal with a mean tidal range of 6.7 m (Long *et al.*, 2006). The waves arrive to Dungeness mainly from the SW and from the NE, the former being dominant. The offshore averaged significant wave height ($\overline{H_s}$) is 1.0 m and the corresponding peak period ($\overline{T_p}$) is 5.5 s. Here, the study is done focusing on the potential role of waves and the tidal forcing is ignored because the waves have been attributed as being the principal driver of littoral drift in this site (Lewis, 1932).

The offshore wave conditions during the study period are obtained from a wave buoy at 43 m depth located at the south of Dungeness Foreland, in front of Hastings. The bimodal wave climate consists of SW waves (high-angle waves at our area of interest) occurring during 65% of the time and NE waves (between low- and intermediate-angle waves at our area of interest) occurring during 35% of the time. The SW waves are also more energetic, with an average significant wave height ($\overline{H_s}$) of 1.1 m and an average peak period ($\overline{T_p}$) of 5.7 s, while the NE waves show $\overline{H_s}$ of 0.9 m and $\overline{T_p}$ of 4.9 s. Fig. 5.2.2 presents wave roses

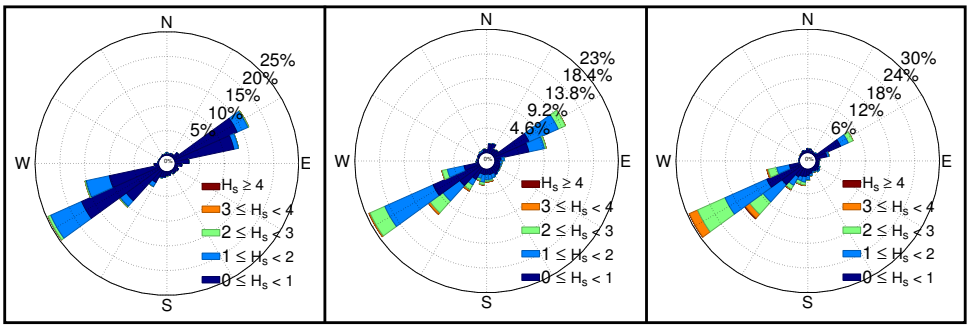

Figure 5.2.2: Offshore wave roses for the periods of March 2005-September 2005 (left), October 2005-March 2006 (center), and February 2014-July 2014.

during different time intervals showing that the percentage of occurrence and intensity of both types of incoming waves varies significantly during the study period.

5.2.2 Qualitative description of the shoreline sand waves

A high-resolution topographic monitoring is being undertaken by the Canterbury Council as part of the South-east Strategic Regional Coastal Monitoring Program, providing one topographic survey every year around July from 2010 to 2016. The surveys are recorded using differential GPS randomly sampled with a spatial horizontal resolution of approximately 2-4 m. They cover a vertical range from +6 m to −3 m with respect to the ordnance datum of Great Britain, encompassing the intertidal zone. Fig. 5.2.3 shows the topographic maps and the bed level change plots, which have been generated using the open source topographical scatter data obtained from the Channel Coastal Observatory (U.K.).

Two striking shoreline undulations with a wavelength of about 450 m are clearly observed in the topographic survey of 2014 (Fig. 5.2.3). These undulations persist during 2015 and 2016 while migrating about 350 m to the north. The undulations are observed across the whole intertidal zone. The bed-level-change-plot during the formation moment (2013-2014) displays a clear pattern of erosion/accretion (red/blue in the lower plots of Fig. 5.2.3). This erosion/accretion pattern translates to the north during 2014-2015 and 2015-2016 coherent with the growth and migration of the undulations. In contrast, for previous years, the bed level change is weaker and the corresponding erosion/accretion patterns go back and forth without a net translation. The topographic plot of 2016 indicates that the northern crest (at $y \sim 1800$ m) starts to diffuse, as it can also be seen from the distortion in its accretion pattern. This is coherent with the fact that farther north no undulations appear (not shown here).

Moreover, intertidal profile surveys are also performed by the Canterbury Council every spring, summer and autumn using differential GPS since 2003. The profiles have a cross-

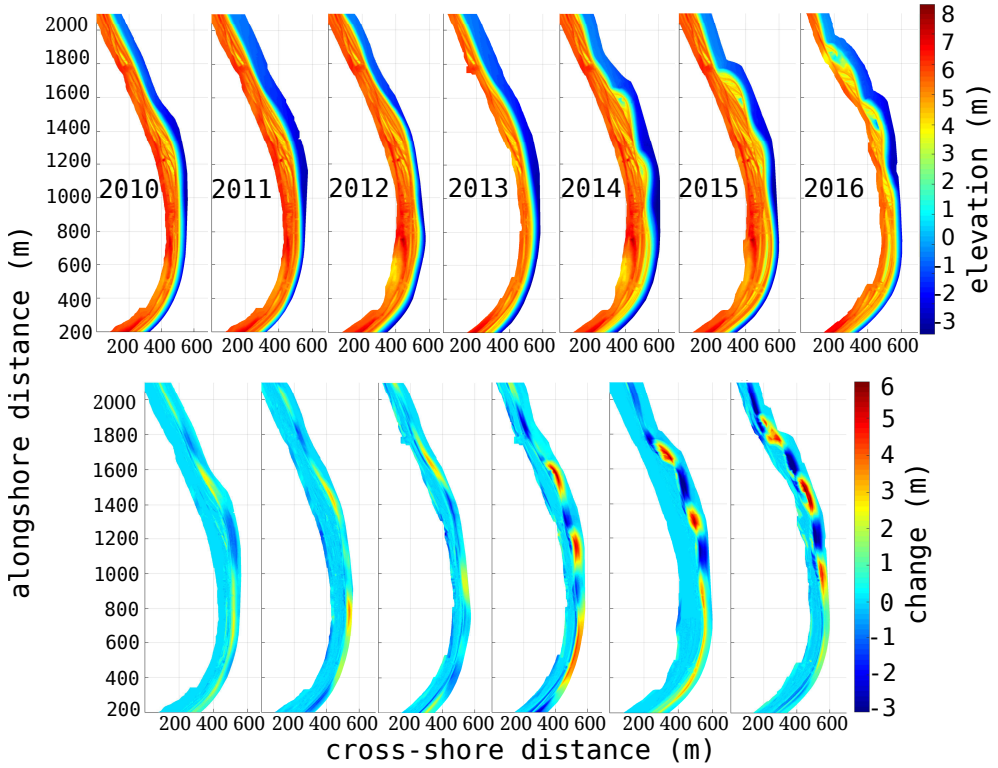

Figure 5.2.3: Surface elevation plots (up) for the years 2010-2016 around July and the corresponding elevation change plots (down) between years. The North direction points upwards.

shore resolution of about 5 m (to some $z = -2$ m) and an alongshore spacing of about 60 m. This second data set is also obtained from the Channel Coastal Observatory. The shorelines have been derived from the two available data sets by interpolating the position corresponding to $z = 0$. In total, 36 shorelines of 2-km length are extracted from February 2003 until February 2016.

Fig. 5.2.4 displays the evolution of the shoreline in time, in which undulations of various wavelengths can be observed. In general, the shorelines can be classified visually in three types: straight (e.g. September 2005, red line), with small-scale undulations (around 200 m wavelength, e.g. March 2006, purple line), and with larger-scale undulations (around 400 m wavelength, e.g. February 2007, orange line, and July 2014, green line). The shoreline data confirm the presence of undulations of $\sim$ 450 m wavelength from July 2014 until February 2016. Moreover, in the shoreline of February 2007, undulations with a slightly smaller wavelength are also visible (of $\sim$ 350 m). Finally, smaller-scale undulations with a wavelength of $\sim$ 200 m appear and disappear throughout the whole study period in many of the shorelines.

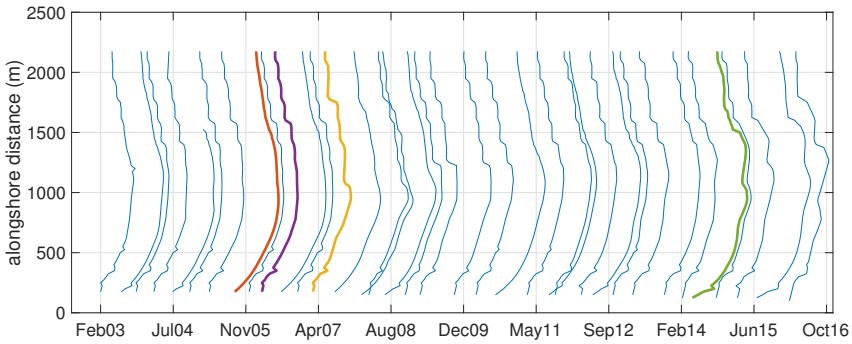

Figure 5.2.4: Shorelines extracted from February 2003 until February 2016. The time is displayed in the x-axis (the lower end of each shoreline indicates its survey time) but the shorelines have the same spatial scale in both axes. The thicker lines correspond to the four dates analysed in Fig. 5.2.5 and discussed in the text.

5.2.3 Shoreline analysis

The Discrete Fourier Transform (DFT) technique is used to quantify the shoreline undulations. The shorelines are first smoothed using a running average (with a window size of 500 m) to obtain average shorelines. Then, the average shorelines are subtracted from the original ones obtaining the rectified shorelines, which show the characteristics of the undulations around an approximately constant straight line. Finally, the DFT of the rectified shorelines is computed. Fig. 5.2.5 shows the DFT magnitude of the three shorelines shown with colours in Fig. 5.2.4. The first one (September 2005) represents a shoreline with no clear dominant wavelength, the second one (March 2006) has a clear peak around 200 m, the third one (February 2007) shows a dominant wavelength of about 350 m, and the fourth one (July 2014) shows a dominant wavelength of about 450 m.

In order to have a condensed and robust representation of the time evolution of the undulations, the DFT magnitude of the two wavelengths that best characterize the observed undulations (350 and 450 m) are extracted for each shoreline (upper panel of Fig. 5.3.6). In particular, the average of the DFT magnitude is computed within a range of ± 30 m around each of the two wavelengths. From November 2006 until May 2007, there is a peak corresponding to the undulations at wavelengths of 350 m. These latter undulations decay gradually and they are no longer observed during spring-summer 2009. From July 2014 until the end of the study period a second (and the largest) peak is detected, corresponding to the undulations at wavelengths of 450 m.

The DFT magnitude of the 200-m wavelength has also been computed (not shown) and it displays a different behaviour from that of the larger wavelengths, with smaller values and a shorter term variability, apparently not correlated with any characteristic of the wave climate. Moreover, these smaller wavelengths are close to the alongshore resolution of the surveyed profiles (60 m) so that the alongshore spacing between cross-shore sections may be

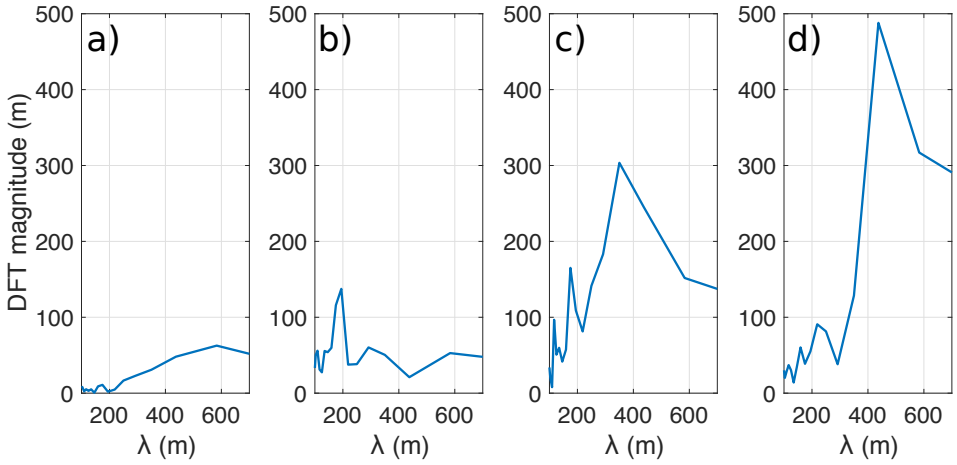

Figure 5.2.5: Magnitude of the Discrete Fourier Transform of the rectified shorelines of September 2005 (a), March 2006 (b), February 2007 (c), and July 2014 (d).

too large to properly resolve such scale. Given that the detection of such wavelengths is not completely reliable and that they seem to be related to different physical processes (because they show a different behaviour), the rest of this study focuses on the larger-scale features.

5.3 Modelling

5.3.1 Wave transformation

In order to investigate the relationship between the observed shoreline sand waves and the high-angle wave instability, the wave parameters at the depth of closure in front of the sand wave area are needed. Thereby, the 10-yr hourly wave parameters at the offshore buoy are propagated to this onshore location using the SWAN model. This is a third-generation wave model that represents the sea state in two dimensions by solving the spectral action balance equation. The details of the model are reported by Booij *et al.* (1999) (version 41.10 is used here). Some physical processes that can be described with the SWAN model are ignored in the present simulations. In particular, the wind wave generation, and the quadruplet and triad interactions are ignored. Instead, diffraction and dissipation by depth-induced breaking and bottom friction are accounted for.

The bathymetry is created by combining two surveys. The first one has a resolution of 0.5×1.0 km (in the north and east directions respectively) and reaches depths of 50 m. The second survey has a resolution of $\sim 2 \times 2$ m and reaches $\sim$1.0 km offshore. For optimization purposes, the SWAN model is first applied to two coarse grids, one of 46×45 km for SW

waves (Fig. 5.3.7) and another of 37×65 km for NE waves (not shown). The cell size in these two coarse grids is 380×380 m. A nested grid of 2×5 km is also used for both types of waves (Fig. 5.3.8), which has a resolution of 8×50 m. A sensitivity analysis to the size of the grids and their resolution has shown that this configuration is optimal and provides an acceptable accuracy. The lateral and offshore boundaries are forced uniformly using a JONSWAP spectrum with the peak enhancement parameter default of 3.3 and a directional spreading of 10 degrees (for each wave condition). The directional spreading is chosen accordingly to the work done by Kaergaard & Fredsoe (2013*b*) in the context of HAWI.

After applying the SWAN model, the parameters of the propagated 10-yr wave series are averaged along the 4 m contour depth in front of the area of interest (i.e. the 2 alongshore kilometres shown in Fig. 5.2.1). Fig. 5.3.9 shows the wave conditions at the buoy and at 4-m depth from October 2013 until June 2014, as an example. The SW waves experience strong refraction during their propagation towards the sand wave area, which causes a significant energy dispersion. This is translated into a significantly smaller H_s in shallow waters in comparison with the buoy (Fig. 5.3.7, 5.3.8 and 5.3.9). In contrast, the H_s of NE waves is kept relatively unchanged. Moreover, the waves with a very high incidence angle (with respect to the studied shoreline) do not necessarily have an effect on the study area as only waves with an angle smaller than 90° (from now on, the incidence wave angles are referenced with respect to shore normal) contribute to alongshore sediment transport. For example, at 6 m depth only 23% of SW waves have a wave angle smaller than 90°, while this is true for 63% of SW waves at 4 m depth. This percentage increases for decreasing depths due to the wave transformation over the fan-shaped bathymetric contours (i.e. the bathymetric contours gradually diverge northwards, as can be seen in the left panel of Fig. 5.3.8).

5.3.2 Correlation between shoreline sand wave presence and high-angle wave incidence

There is some debate on the definition of high angle waves, i.e. on the precise value of the wave angle at the depth of closure, θ_c, above which HAWI develops. Ashton *et al.* (2001) gave the value of $\theta_c = 42°$. However, this theoretical prediction can vary depending on the sediment transport formula (Ashton & Murray, 2006*b*), on the assumptions of the model (Falqués & Calvete, 2005; van den Berg *et al.*, 2012; Kaergaard & Fredsoe, 2013*a*) and on the shape of the bathymetric undulations associated to the shoreline undulations (Idier *et al.*, 2017). In this section we adopt the value $\theta_c = 45°$ for being representative of most of the predicted values.

To quantify the degree of dominance of destabilizing over stabilizing waves in the wave climate (i.e. high-angle waves, $|\theta| > 45°$, versus low-angle waves, $|\theta| < 45°$), the "strength" of the high-angle waves for each time survey, t_k, is defined as

$$E(t_k)_{>45^\circ} = \int_{45^\circ}^{89^\circ} d\theta \int_{t_{k-1}}^{t_k} H^{5/2} dt + \int_{-89^\circ}^{-45^\circ} d\theta \int_{t_{k-1}}^{t_k} H^{5/2} dt \tag{5.3.1}$$

where H and θ in these formulas are those computed at 4 m depth in front of the shoreline wave area. The 5/2 power is introduced because, according to the widely used CERC formula

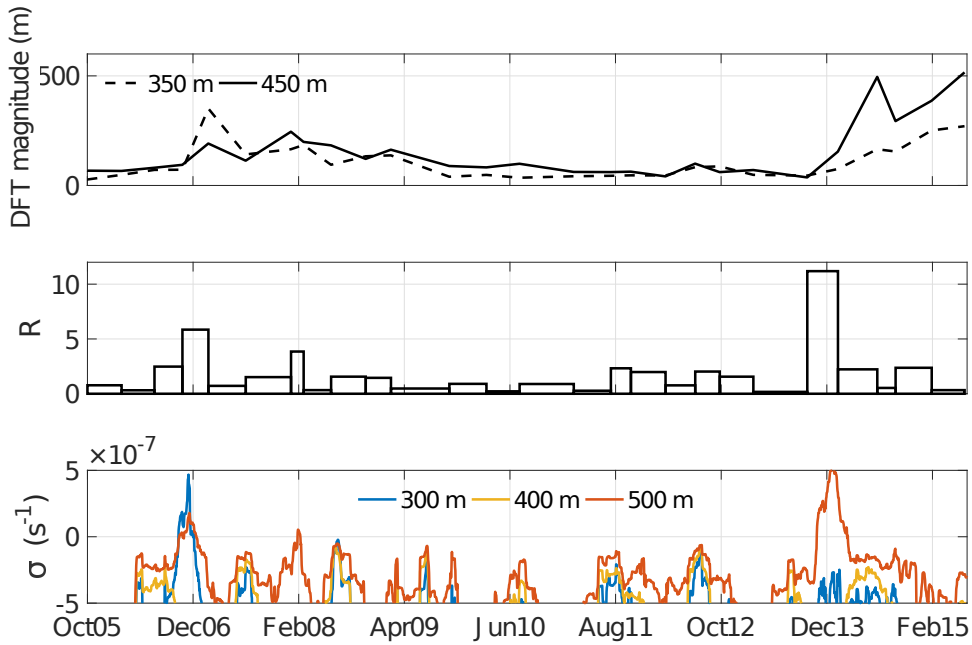

Figure 5.3.6: DFT magnitude of the two wavelengths characterising the observed shoreline sand waves (upper panel), coefficient R averaged during the time period between consecutive shoreline surveys (middle panel) and growth rate of the LSA for three wavelengths (lower panel).

(Komar, 1998), the total alongshore transport rate is proportional to $H_b^{5/2}$. Similarly, the "strength" of the low-angle waves is defined as

$$E(t_k)_{<45^\circ} = \int_{-45^\circ}^{45^\circ} d\theta \int_{t_{k-1}}^{t_k} H^{5/2} dt \tag{5.3.2}$$

Afterwards, the wave-dominance ratio, R, is defined as $R(t_k) = E(t_k)_{>45^\circ}/E(t_k)_{<45^\circ}$. The time intervals with $R > 1$ correspond to a dominance of high-angle waves over low-angle waves. The larger R, the stronger the relative influence of high-angle waves.

The middle panel of Fig. 5.3.6 shows the time series of R, obtained during the time period between consecutive shoreline measurements, from October 2005 to November 2015. The coefficient R is almost always above 1 and there are two main peaks of about $R = 11$ and $R = 6$. The peak of $R = 6$ coincides with the formation event of sand waves around February 2007, as can be seen in the corresponding DFT-magnitude peak for $\lambda = 350$ m. Relative low values of R during April 2009 to September 2013 are roughly consistent with small DFT magnitudes of the two analysed wavelengths. The largest peak in R takes place around February 2014, clearly related with the formation event of 2014 that is visible as an increase in DFT magnitude for $\lambda = 450$ m. Notice that the R peaks and the DFT-magnitude peaks display a small time lag of 3-6 months. This makes sense because on the one hand the surveys are available every 3-4 months and on the other hand the shoreline undulations

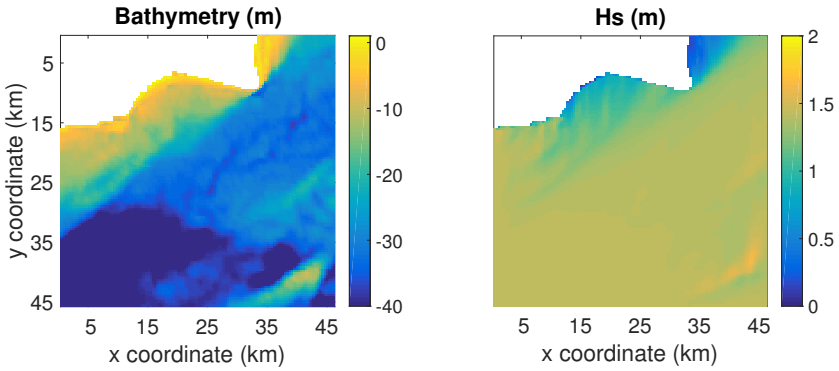

Figure 5.3.7: Coarse grid bathymetry (left panel) and significant wave height (right panel) for the SW wave averaged conditions The North direction points upwards.

can only be detected when they have reached a significant amplitude.

5.3.3 Linear stability analysis

1Dmorfo setup

Here, the linear stability model 1Dmorfo, described in Chapter 2.3, is used to investigate the formation events of the undulations observed in Dungeness. Regarding the model setup, the equilibrium cross-shore beach profile is extracted from combining the high-resolution intertidal topographic surveys (which extend to about 3 m depth) and the bathymetry extending 1 km offshore. The wave conditions at D_c are obtained from those propagated with SWAN and two different types of simulations are performed: one type uses the full 10-yr wave series and the other type applies constant wave conditions. The empirical constant μ (in the CERC equation, Eq. 2.2.9), which modulates the strength of the alongshore transport, is set to μ =0.15 $m^{1/2}s^{-1}$. Regarding the perturbation, several values of λ in the range of the observed ones (λ =200-1000 m) are used. Regarding the cross-shore shape of the perturbation, a cross-shore shift of the profile is used as the shoreline moves onshore/offshore. Given that the available high-resolution topographic measurements show that the shoreline sand waves extend across the whole measured domain, from $z = +4$ m until $z = -3$ m (Fig. 5.2.3), a default depth of closure of $D_c = 4$ m is used. The latter two choices are motivated and discussed in Chapter 5.4.3.

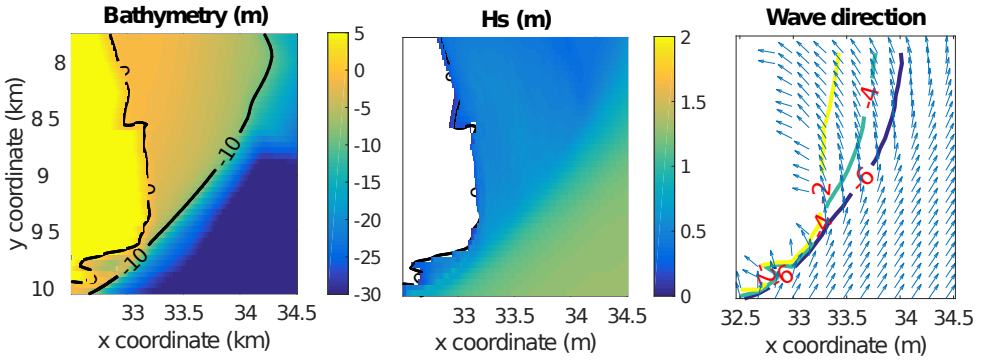

Figure 5.3.8: Nested grid bathymetry (left panel), significant wave height (central panel) and wave direction (right panel) for the SW averaged conditions. The North points upwards.

Wave series simulations

The 10-yr alongshore averaged wave series at 4 m depth (e.g. red lines in Fig. 5.3.9) is used as input for the 1Dmorfo model. For each (hourly) record of the time series, t_j, and for a number of wavelengths, λ, the growth rate $\sigma(t_j) = \sigma_r(t_j) + i\sigma_i(t_j)$ for each wavelength is computed. This means that the amplification factor of a small amplitude sand wave with wavelength λ from t_j to $t_j + \Delta t$, where $\Delta t = 1$ h is $\exp(\sigma_r(t_j)\Delta t)$. Thus, when $\sigma_r(t)$ for a given λ is positive, sand waves of this wavelength are expected to grow. On the contrary, when $\sigma_r(t)$ for a λ is negative, such sand waves are expected to decay. The wave time series has a strong variability at hourly level while the morphology reacts much more slowly. For this reason, instead of examining the raw $\sigma_r(t)$ time series, a filtered time series with a running average (window of 90 days) is used. The wave series simulation has been done for $\lambda = 200$ m to $\lambda = 1000$ m with a 20 m spacing. Notice that the 1Dmorfo model can only resolve length scales significantly larger than the surf zone width (which is about 30 m for the energetic periods in this area).

The lower panel of Fig. 5.3.6 shows the time series of the filtered σ_r for $\lambda = 300$, 400 and 500 m, which are relevant wavelengths according to the observations. It is seen that the growth rate for $\lambda = 300$ m is always negative, except during December 2006, preceding the sand wave formation event that is observed during the winter 2006-2007. In December 2006, the σ_r corresponding to 500 m also has a positive value although smaller. This σ_r corresponding to $\lambda = 500$ m is always negative except in December 2006 and in winter 2013-2014. During this second period it shows a remarkable peak, preceding the observed sand wave formation event of spring 2014. Thereby, the LSA model accurately predicts the observed shoreline sand wave formation moments, with the modelled wavelengths slightly under-predicting/over-predicting the observed ones in the first/second event. The characteristic growth time of the instability, σ_r^{-1}, is of 23 days in the peak of winter 2013-2014 (and slightly larger). This is in the correct order of magnitude in account of the observed reaction time of this morphological system.

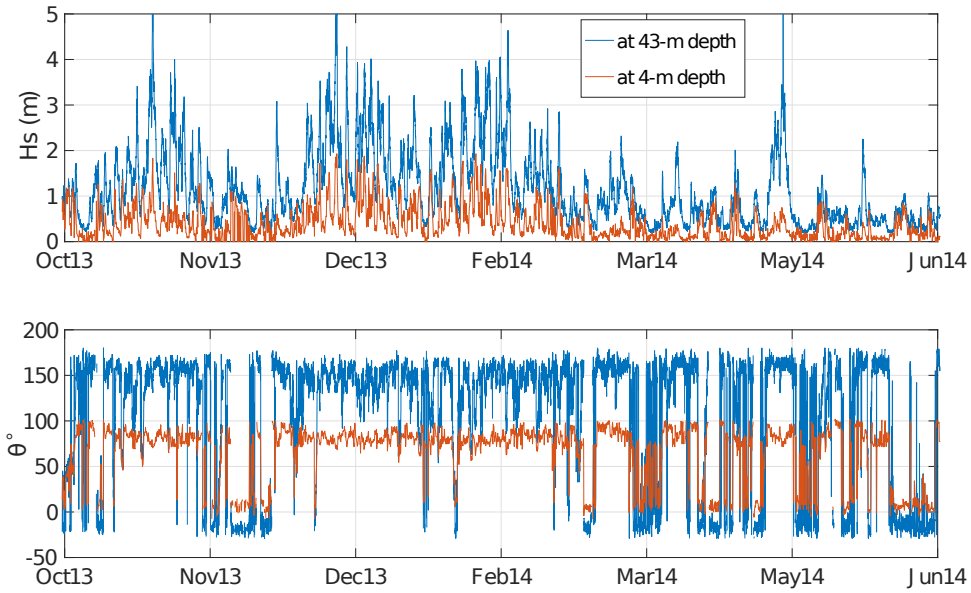

Figure 5.3.9: Time series of the significant wave height (upper panel) and wave direction with respect to the shore normal of the studied shoreline stretch (lower panel) from October 2013 until June 2014. The blue line shows the offshore wave conditions recorded at the buoy (43-m depth) and the red line are the wave parameters at 4-m depth in front of the shoreline sand waves area.

It is found that the positive σ_r periods occur when the R ratio is large enough ($R > 5$), which is consistent with the HAWI theory. After the formation, although the modelled σ_r switches from positive to negative values, the observed sand waves can persist or even keep on growing for a while. We must recall that the linear stability analysis is valid only for small amplitude sand waves and it is possible that, after the initial formation, non-linear interactions drive their dynamics. Finally, it is important to notice that the growth rate for $\lambda = 400$ m is always negative while one would expect positive σ_r for this wavelength during the two formation events (since this λ is close to the observed ones).

Finally, the model predicts an averaged migration rate of 600 m/yr, for λ =500 m, during the period 2014-2016 (the period when undulations of this wavelength are observed to migrate, see Fig. 5.2.3). The migration direction and its order of magnitude agree with the observed ones (about 200 m/yr, see Chapter 5.2). The over-prediction might be related to the fact that the model assumes perturbations of infinitesimal amplitude whereas the migration is observed for fully developed shoreline undulations. In other studies of coastal morphodynamic patterns, the migration rate in the non-linear regime is half of that obtained in the linear regime (Garnier *et al.*, 2008).

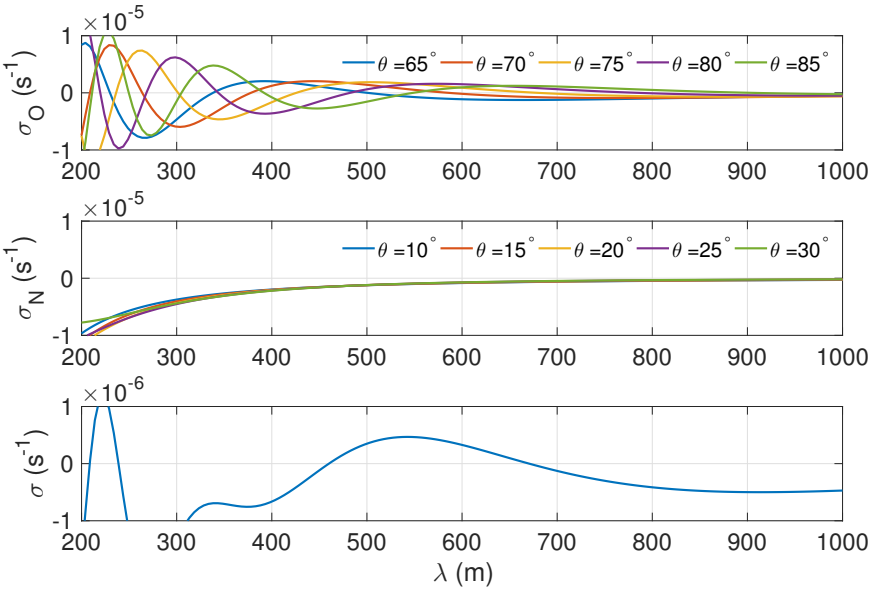

Figure 5.3.10: Growth rate curves for different incident angles representing high-angle waves (upper panel) and low-angle waves (middle panel) during winter 2013-2014. Average growth rate curve (lower panel) using a weighting associated to the frequency of high- and low-angle waves.

Constant waves simulations

In order to understand the results of the wave series simulations, an analysis for constant (in time) wave parameters is very convenient. First of all, the average wave statistics of high-angle ($|\theta| > 45°$) and low-angle ($|\theta| < 45°$) waves are computed for the period period prior to the second formation event (December 2013 - March 2014). This gives $H_s = 0.85$ m, $\theta = 75°$ and $T_p = 6.8$ s for high angles and $H_s = 0.58$ m, $\theta = 20°$ and $T_p = 5.1$ s for low angles. During this period, high-angle waves occur 93% of the time and only 7% of the waves are low-angle (this can be appreciated in Fig. 5.3.9). The 1Dmorfo model is then run for high-angle and for low-angle waves with the corresponding values of H_s and T_p. Five different angles are considered for each case: the average one and the latter $\pm 5°$ and $\pm 10°$. In this way, five growth rate curves (σ_r-λ) for high-angle and five for low-angle waves are computed and shown in Fig. 5.3.10.

As can be seen in that figure, the low-angle waves damp all the wavelengths, with a stronger damping for smaller wavelengths and smaller angles. In contrast, the high-angle waves produce positive σ_r but, remarkably, each instability curve has three local maxima (in the range $\lambda > 200$ m). The larger the the angle, the larger the wavelengths of the maxima and the smaller the corresponding maximum σ_r values. Typically, the instability curves for HAWI present a single maximum (Falqués & Calvete, 2005). However, as was found by

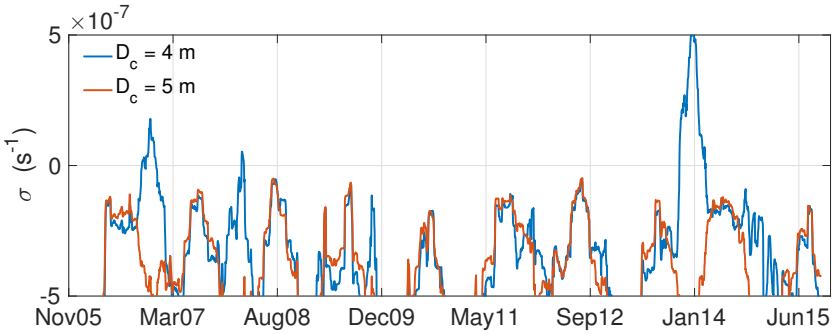

Figure 5.3.11: Growth rate sensitivity of $\lambda = 500$ m to the depth of closure.

van den Berg *et al.* (2014), secondary maxima can sometimes occur. This happens for a marginal region in the parameter space, for very high wave angles, for some combinations of bathymetric profiles and wave periods, and for relatively short wavelengths ($\lambda \sim 1$ km or less), and it can be interpreted as follows. The damping of short wavelengths in HAWI is controlled by wave energy focusing/defocusing by the undulations (van den Berg *et al.*, 2014). For relatively long wavelengths, in comparison with the offshore reach of the bathymetric perturbation, the focusing is always near the sand wave crests (i.e. the prograding section) and the defocusing near the embayments. This was also explained by Uguccioni *et al.* (2006) as a result of each wave ray crossing only one of the shoals associated to the shoreline undulation. However, for relatively short wavelengths, large angle and small periods, each wave ray can cross several shoals. In this situation, the wave focusing can take place away from the crests and is highly sensitive to the wavelength, wave angle and bathymetry. As a result, the instability curve becomes quite complex for short wavelengths featuring several local maxima that look somewhat erratic (very sensitive to small changes in the angle and the bathymetry).

A way to filter out such strong sensitivity, in account of the inherent uncertainty sources coming from the parameters and the model, is to make an average of the different growth rate curves with a weighting associated to the frequency of high and low-angle waves. The corresponding averaged curve shows a local positive maximum at $\lambda \approx 540$ m and another at $\lambda \approx 220$ m (lower panel of Fig. 5.3.10). Since the 220 m wavelength peak is in the lower limit of the length scales that can be resolved by the 1Dmorfo model (given the surf zone width in this case) this averaging lends support to the robustness of $\lambda \approx 500$ m as an output of the LSA for the time series of wave parameters. This is in good agreement with the 450-m wavelength of the formation event in 2014. Rather, the wavelengths below 500 m must be taken with care and this explains why the linear stability analysis can predict growth for $\lambda = 300$ m and decay for $\lambda = 400$ m during the 2006-2007 event, where the observed wavelength is $\lambda \approx 350$ m.

5.4 Discussion

5.4.1 Role of HAWI on Dungeness shoreline undulations

Our hypothesis is that the shoreline undulations observed in Dungeness with wavelengths of about 350 m and 450 m can be classified as self-organized km-scale shoreline sand waves (KSSW). Their wavelength is smaller than other observed KSSW because they appear in a relatively sheltered area. However, these undulations could be related to other types of features like beach cusps. Indeed, although beach cusps are quite common on gravel beaches their wavelength is at least one order of magnitude smaller than the observed one, discarding such hypothesis. Instead, $350 - 450$ m could be a very plausible wavelength for megacusps linked to rhythmic surf zone bars. However, rhythmic surf zone bars have never been observed on macrotidal gravel beaches (van Enckevort *et al.*, 2004) and they do not show up in any of the available surveys of Dungeness. This is consistent with the fact that this beach is nearly reflective ($\Omega \sim 1.2$, where Ω is the dimensionless fall velocity parameter in Wright & Short, 1984). Therefore, we can also discard that the shoreline undulations are associated to rhythmic bars. The possibility that the shoreline sand waves could be forced rather than self-organized can also be discarded. Offshore Dungeness, there are sand banks (which can be observed in Fig. 5.3.7) and the SWAN computations indeed show that they influence wave refraction and can focus wave energy. However, sensitivity analysis to the presence of such offshore banks made with the SWAN model prove that the influence of the sand banks does not reach the sand wave area. Another potential hydrodynamic template forcing that could drive the shoreline undulations is wave diffraction, which can generate patterns in the wave energy field, which in turn could lead to associated patterns in the shoreline morphology. Indeed, the configuration of the Dungeness Cuspate Foreland causes diffraction of the SW waves around its tip. However, the SWAN model has been run including and excluding wave diffraction. The simulations showed that this process just causes a slight decrease in wave energy without inducing alongshore rhythmic wave patterns.

The observations also confirm that the KSSW are a result of the high-angle wave instability (HAWI) because i) a clear correlation between its formation period and the occurrence of high-angle waves is found and ii) the results of the 1Dmorfo model, which includes such instability, are coherent with the observations (Fig. 5.3.6). Also, it can be seen that the larger shoreline undulations (λ =350-450 m) appear when the wave energy is at least five times larger than the low-angle wave energy ($R > 5$). Several authors (Ashton & Murray, 2006*b*; van den Berg *et al.*, 2012; Kaergaard & Fredsoe, 2013*a*) studied numerically the proportion of high-angle waves, U, required to de-stabilize the shoreline. This was done by forcing an idealized bathymetry with two wave conditions: $\theta = 60°$ or $\theta = 30°$ (having the same H_s and T). The limit found ranged from $U \approx 0.5$ up to $U \approx 0.8$. In the present approach, the proportion of high-angle waves, U, can be related with R as $U = R/(1 + R)$. Thus, a threshold of $R \approx 5$ implies $U \approx 0.83$ which differs from the threshold $U \approx 0.5$ predicted by Ashton & Murray (2006*b*) but is consistent with the threshold $U \approx 0.8$ found by the more realistic models of van den Berg *et al.* (2012) and Kaergaard & Fredsoe (2013*a*)

Fig. 5.3.6 also shows that the DFT magnitude of the 350 m and 450 m wavelengths is maintained (or it even continues to increase) despite the R values decreasing below the threshold (and the 1Dmorfo model hence predicting negative growth rates). It seems that

once the sand waves have been formed, R values above 2 would favour their maintenance and growth despite being below the R threshold. As discussed in Section 5.3.3, this behaviour cannot be reproduced by a linear model because non-linear effects play an important role in the finite-amplitude behaviour. Moreover, the morphological response do not only depend on the wave forcing but also on the previous morphological state (as has been recognized for different types of rhythmic features, see e.g. Calvete *et al.*, 2007).

As mentioned in Section 5.2.2, the shoreline sand waves are restricted to the area close to the Dungeness tip, i.e. no undulations appear further north. Actually, no more than 3 crests can be observed at the same time. Also, during the migration experienced by the undulations in 2015-2016, the crest further north exhibits a distorted accretion/erosion pattern (it starts to diffuse) while the southern crests exhibit a consistent accretion/erosion pattern. There are two factors favouring this behaviour. First, the beach profiles have a milder slope to the north and according to HAWI theory milder slopes tend to diminish growth rates (Falqués & Calvete, 2005). Second, the SW waves have to travel larger distances further north, experiencing more refraction and more energy loss (Fig. 5.3.7), while NE waves have approximately the same energy along the whole north-east flank of Dungeness. Therefore, the wave energy leading to a stable coastline (NE) is alongshore constant while the wave energy favouring the formation of the KSSW (SW) decays gradually to the north. The combination of the alongshore decrease of the SW energy and in beach profile would explain why the sand waves develop only close to the tip of the foreland.

5.4.2 Role of tides on Dungeness shoreline undulations

This study has been based on the effect of the alongshore wave-driven transport while the possible morphodynamic effect of the tides (both the induced currents and sea-level variations) has been ignored. It is well known that the coupling of tidal waves and the sea bed morphology in the continental shelf can originate the formation of sand waves and sand ridges with wavelengths from hundreds of meters to kilometres, respectively (Blondeaux, 2001). Regarding the coastal zone, a tidal wave propagating along an undulating shoreline can create vortices in the horizontal residual circulation that can feedback positively into the undulations (Zimmerman, 1981; van der Vegt *et al.*, 2007). However, the alongshore characteristic length scales of the corresponding positive feedback are typically larger than those of the observed undulations at Dungeness.

Besides producing currents, the tides vary the water level and therefore the shoreline location. This is important because the linking of the shoreline undulations with the depth contours is accomplished by the cross-shore exchange of sediment. On a microtidal coast, this is only done by storm waves, but on a macrotidal coast, the cross-shore sediment exchange can be enhanced by the cross-shore translation of the surf zone during tidal oscillations. The 1Dmorfo model does not take explicitly into account variations in the sea level but the tidal effect of enhancing the cross-shore sediment exchange is considered implicitly by increasing the depth of closure (see also next Section). In any case, a modelling study including sea-level variations and both wave- and tide-driven currents would be desirable to study the role of tides.

5.4.3 Justification of the setup chosen in the 1Dmorfo model

Taking into account the bathymetric perturbation associated to the shoreline undulations is essential for the feedback between waves and morphology leading to HAWI. However, as the 1Dmorfo model is based in the one-line approximation, the link between shoreline undulations and bathymetric undulations must be prescribed. Available one-line models (e.g. Genesis, Unibest-CL) make this link by assuming a cross-shore shift of the profile following the perturbed shoreline. Applying this bathymetric perturbation, called $P1$, the perturbed shoreline amplitude is the same as the cross-shore amplitude of any depth contour. Another plausible link is based on assuming a linear decay of the bed level perturbation. For this bathymetric perturbation, called $P2$, the cross-shore amplitude of the depth contours beyond the surf zone can be larger than the amplitude of the perturbed shoreline (for certain profiles). The influence of this choice in the formation of KSSW has been investigated thoroughly by Idier *et al.* (2017). It was found that low-angle waves can be de-stabilizing only for the perturbation $P2$. It is unknown how frequent this occurs in nature, but it seems that it can happen in at least one case (Falqués *et al.*, 2017). For the present study, the 1Dmorfo model has been applied assuming both perturbations ($P1$ and $P2$) because the bathymetric perturbation in the field can not be inferred from the available data. The growth rates using the perturbation $P2$ (not shown) are positive for low-angle waves and negative for high-angle waves, for wavelengths in the order of the observed ones. In contrast, the growth rates using the perturbation $P1$ are negative for low-angle waves and positive for high-angle waves (Fig. 5.3.6). Since the observed formation events of sand waves are correlated with high-angle waves, it is concluded that only the perturbation $P1$ adequately represents the physics of the initial instability mechanism in this site.

Based on the fact that the observed KSSW extend up to 3 m depth, a depth-of-closure value of 4 m is chosen in Section 5.3.3. In our study area, there are no available measurements of the D_c derived from cross-shore profiles dynamics. A relatively close site with these type of measurements is the south of the Dutch coast, which is subject to more energetic waves. Hinton & Nicholls (1998) reported $D_c = 5$ m. Also, the well-known Hallermeier formula (Hallermeier, 1981) can be used to provide an estimate (see, e.g. Falqués *et al.*, 2017). For the case of Dungeness, the extremal wave height from the 10-yr propagated series is $H_e \approx 1.3$ m, with a wave period $T_p \approx 5.2$ s, which gives $D_c \approx 2.5$ m. This closure depth is smaller than the depth at which the undulations are observed. Besides, the D_c is overshadowed by the tidal range of 6.7 m. As discussed in Section 5.4.2, on a macrotidal coast D_c can be larger than in a microtidal coast with the same wave conditions. Therefore, the chosen closure depth of 4 m is reasonable.

In order to check the sensitivity to the value of D_c, larger depths of closure have also been used in which case no growth is predicted to occur. As an example, Fig. 5.3.11 shows that if $D_c = 5$ m only negative growth rates are obtained for $\lambda = 500$ m. The reason for this behaviour is that the 1Dmorfo wave propagation does not represent well the real propagation at this site. The model assumes alongshore-uniform unperturbed depth contours parallel to the shoreline, while the contours at the north-east flank of the Dungeness foreland show a fan shape (i.e. the bathymetric contours gradually diverge northwards, as can be seen in Fig. 5.3.8). Then, if a depth of closure of 6 m is taken, 77% of the SW incoming waves have an angle larger than 90° at that depth and the model ignores the morphodynamic effect of these waves. Instead, at 4 m depth only 37% of SW waves can not be properly represented

by the model.

5.5 Conclusions

The formation of km-scale shoreline sand waves (KSSW) with alongshore wavelengths of $350 - 450$ m has been observed along the north-east flank of Dungeness foreland (U.K.), close to the tip. Two clear formation moments have been detected during the study period (February 2003 - February 2016), one on February 2007 with a wavelength of 350 m and the second one on July 2014 with a wavelength of 450 m. A gradual decay of the 2007 shoreline undulations is observed and they are no longer visible on autumn 2009. The undulations formed at the second event persist at least until February 2016 (with some decay) and migrate northward at a mean rate of about 200 m/yr.

The role of the high-angle wave instability (HAWI) on the formation and dynamics of the shoreline undulations has been examined. A ratio quantifying the degree of dominance of high-angle waves over low-angle waves, R, has been computed at 4 m depth and a good correlation between high R values and the formation of the shoreline sand waves has been found. In particular, the undulations occur when $R > 5$ implying that a climate with 80% of high-angle waves is needed to trigger their formation, in agreement with previous HAWI studies. Therefore, it is concluded that HAWI is the primary cause of the shoreline sand wave formation in Dungeness.

A linear stability analysis has also been performed using a morphodynamic model based on the one-line approximation that can describe HAWI. The model predicts positive growth rates previous to the two observed formation moments for wavelengths similar to the observed ones. It is also found that a bathymetric perturbation corresponding to a cross-shore profile shift is required to reproduce the growth of sand waves with the observed characteristics. Moreover, the morphological response occurs at time scales of the order of the observed ones (characteristic growth time of about 1 month and migration rates of hundreds of metres per year) and it is not only related to the wave forcing but also to the preceding bathymetric configuration. Finally, the applied linear model has been able to represent the initial formation of the undulations but it fails to reproduce the dynamics of the finite-amplitude features. A non-linear model is needed to reproduce the medium-term and long-term evolution of the observed shoreline undulations. Indeed, the two events with KSSW formation and further evolution detected at Dungeness represent a unique opportunity to validate such models.

Chapter 6

Synthesis

The present thesis aims at providing more insight into the dynamics of shoreline large-scale perturbations with an emphasis on the wave obliquity. A non-linear morphodynamic model, called Q2Dmorfo, that describes large-scale shoreline dynamics has been improved and used to predict the evolution of the ZandMotor (ZM) mega-nourishment. The performance of future mega-nourishments has been further investigated, focusing on the role of its initial shape and the wave climate. Finally, events of formation of km-scale shoreline sand waves (KSSW) have been detected in a shoreline stretch at the Dungeness Cuspate Foreland. A linear stability analysis based on the one-line approximation (1Dmorfo model) has been used to investigate the origin of those sand waves. Below, the findings of Chapters 2-5 are summarised by answering the research questions posed in the introduction and the future research is subsequently outlined.

6.1 Main findings

1) Can the fuzzy shoreline algorithm improve the performance of morphodynamic models?

The version of the Q2Dmorfo model presented by van den Berg *et al.* (2012) treated the shoreline as a sharp boundary between the dry and the wet beach, as is done in most existing morphodynamic models. The numerical implementation of the corresponding boundary conditions is not straightforward and led to a severe limitation on the maximum shoreline angle deviation induced by the perturbation that could be described (13°). The fuzzy shoreline algorithm makes no essential difference between dry and wet cells and treats the shoreline and its neighbouring area as a transition zone, which can be interpreted as the swash zone. As a result, the implementation of the sediment transport equations is simpler and the model now overcomes the shoreline slope limitation of 13°. In the case of shoreline sand waves, the model is able to describe its dynamics for longer times and with larger amplitudes up to the transition to spit formation. Also, the obtained wavelengths are similar but the initial growth rates are smaller for the self-organized sand waves, which is

in better agreement with the linear stability model predictions of Falqués & Calvete (2005). Interestingly, the longer simulation time allows to observe a clearer tendency to growth saturation.

The fuzzy shoreline algorithm is very efficient and improves significantly the performance of the Q2Dmorfo model. This is an indication that it could also be applied to other morphodynamic models, which typically have problems in dealing with the shoreline boundary conditions.

2) Can the long-term evolution of a mega-nourishment be reproduced by current numerical models?

One-line numerical models, classically used for designing nourishments, assume that the cross-shore amplitude of the depth contour perturbations is the same as the one of the shoreline. However, the ZandMotor bathymetric measurements show that the perturbation of the depth contours gradually decays until the depth of closure. Given that the alongshore wave transport is expected to drive the ZM evolution and that it depends on the wave conditions at breaking, the correct description of the bathymetric contours is crucial to successfully transform the waves from offshore until the breaking depth. The Q2Dmorfo model takes these processes into account by using a cross-shore transport that gradually drives the bathymetry to the equilibrium. The Q2Dmorfo has been calibrated with the ZM bathymetries (filtering out the nearshore bars) measured during 1 yr. After this calibration process, the model properly reproduced the observed ZM evolution during the next 2 yr, not only of the shoreline but also of the bathymetric contours. Therefore, the model is able to reproduce the most relevant traits exhibited by the ZM.

In this thesis it is proved that a model such as the Q2Dmorfo can successfully reproduce the long-term behaviour of mega-nourishments. However, it is crucial to include the feedback of the bathymetric evolution into the wave field. Also, all wave angles of the wave climate must be considered, in particular those larger than 45° can have a critical influence.

3) What is the long-term behaviour of the ZandMotor and in particular what is its lifetime?

The calibrated Q2Dmorfo model has been used to predict the long-term behaviour of the ZandMotor using different wave climates, WC, with slightly different high-angle wave occurrence (frequency around 62%). The results show that the shoreline will behave diffusively, so that the amplitude of the perturbation will have decayed from the initial 960 m (immediately after construction) to about 350 m, 30 yr after the ZM installation. At the same time, the shoreline of the adjacent beaches, 2.5 km at each side, will have prograded (on average) by about 100 m at the NE defined section and about 80 m at the SW defined section. These results are very robust since they are reproduced with the five applied WC. The model predicts very small alongshore migration rates (due to the bidirectional WC). The diffusivity is smallest for the WC showing the largest percentage of high-angle waves.

An effective diffusivity of the shoreline, due to the alongshore sediment transport, has been evaluated by analysing the shoreline evolution during the first 3 yr, obtaining similar results for the measured and the modelled shorelines, of about 0.0022 m^2/s. In contrast, the classical one-line approach, which neglects the bathymetry-wave feedback, over-predicts

the diffusion by a factor of 2.5. The diffusivity can be used to compute the ZM lifetime, here defined as the time needed to reduce the amplitude after construction by a factor 5. The classical diffusivity predicts a lifetime of only $\sim$ 35 yr whereas the Q2Dmorfo diffusivity predicts a lifetime of $\sim$ 90 yr.

4) What is the effect of wave obliquity in the evolution of a mega-nourishment? Could a mega-nourishment trigger the formation of shoreline sand waves?

The wave angle has an important influence on the dynamics of mega-nourishments and should be taken into account in their design. If the wave climate is dominated by low-angle waves (<45°) the diffusivity of a mega-nourishment is larger than in case where both low- and high-angle waves are present. In particular, the diffusivity decreases linearly with increasing frequency of high-angle waves. If high-angle waves dominate (frequency above 80%) erosional hotspots are formed at the sides of the mega-nourishment. This is specially strong when the high-angle waves come mostly from one side (unimodal wave climate), in which case a dramatic alongshore migration of the mega-nourishment is also produced (e.g. a displacement of 800 metres occurs after 50 years for 90% of high-angle waves). A smaller but significant migration can also occur with bimodal wave climates that have a certain directional asymmetry. In this cases there is also an asymmetry in the feeding to adjacent beaches.

According to van den Berg *et al.* (2011), the formation of erosional hotspots precedes the triggering of km-scale shoreline sand waves due to high-angle wave instability (HAWI). In the present simulations it is found that, as explained above, this occurs above a frequency of 80% of high-angle waves. However, the simulation time of 50-yr used in this thesis was not large enough to develop a full train of sand waves. Only in the case of a 100% of unidirectional high-angle waves, the formation of sand waves has been directly observed. In the case of the ZandMotor, the beach is safe from being destabilized by the mega-nourishment because the wave climate only has 62% of high-angle waves.

A collateral result of the importance of wave obliquity is that, when building synthetic wave climates, four wave incidence sectors must be considered: two representing low-angle waves and two representing high-angle waves. Using one or two wave sectors gives large errors and using more than four wave sectors does not improve the performance.

5) What is the role played by the initial shape and size of a mega-nourishment on its own evolution?

The role of the mega-nourishment shape on its own evolution has been analysed focusing on its initial shape asymmetry, the shape ratio and the volume. The initial shape asymmetry only affects the asymmetry in the feeding to adjacent beaches. The beach at the side of the mega-nourishment with the largest shoreline slope receives more sediment, not only in the short term but also in the long term. The shape factor and the volume control the diffusivity. Smaller and wider mega-nourishments are more diffusive than larger and narrower (more localized) ones. This might be due to the fact that the larger cross-shore perturbations of the depth contours linked to the narrower and larger mega-nourishments produce larger perturbations in the wave field. This, together with the obliquity of the wave climate, in turn enhances the processes leading to shoreline instability, thereby decreasing the diffusivity.

6) Can the formation of km-scale shoreline sand waves be observed in nature, and if so, is it linked to the wave climate?

Detecting the formation of km-scale shoreline sand waves is in general very difficult due to the large time and length scales involved. In the present thesis, KSSW have been observed along the north-east flank of Dungeness foreland (U.K.). Two clear formation moments have been detected during the study period, the first one on February 2007 with a wavelength of 350 m and the second one on July 2014 with a wavelength of 450 m. A gradual decay of the 2007 shoreline undulations is observed and they are no longer visible on autumn 2009. The undulations formed at the second event persist at least until February 2016 (with some decay) and migrate northward at a mean rate of about 200 m/yr.

The role of HAWI on the formation and dynamics of these shoreline undulations has been examined. A ratio quantifying the degree of dominance of high-angle waves over low-angle waves, R, has been computed at 4 m depth and a good correlation between high R values and the formation of the shoreline sand waves has been found. In particular, the undulations occur when $R > 5$ implying that a climate with 80% of high-angle waves is needed to trigger their formation, in agreement with previous HAWI studies and with the results about mega-nourishments of this thesis (see the previous question). Therefore, it is concluded that HAWI is the primary cause of the shoreline sand wave formation in Dungeness. This is a unique data set that shows for the first time the formation moment of KSSW showing a clear correlation with the dominance of high-angle waves at that time.

7) How morphodynamic models results compare with observed shoreline sand wave formation?

The 1Dmorfo linear stability model was used to model the formation of KSSW in Dungeness. The model predicts positive growth rates previous to the two observed formation moments for wavelengths similar to the observed ones. It is also found that a bathymetric perturbation corresponding to a cross-shore profile shift is required to reproduce the growth of sand waves with the observed characteristics. Moreover, the morphological response occurs at time scales of the order of the observed ones (characteristic growth time of about 1 month and migration rates of hundreds of metres per year). Despite the applied linear model has been able to represent the initial formation of the undulations it can not to reproduce the dynamics of the finite-amplitude features.

6.2 Future Research

The design and prediction of beach nourishment evolution has been traditionally done with one-line numerical models, which assume an instantaneous profile shift as cross-shore link between the shoreline and the depth contours. This approach has been successful because the correct description of the depth contours (over which waves are transformed) can be neglected for small nourishments and moderate wave angles. However, larger nourishments, such as the ZandMotor, perturb significantly the depth contours. Under these conditions, the one-line modelling studies of mega-nourishments implicitly confirm that an accurate description of the bathymetric contours is key for the correct prediction of its evolution. For

example, in the ZM context, Tonnon *et al.* (2018) tested two different depths of closure (6 m vs 19 m) and found a large discrepancy in the obtained one-year net alongshore sediment transport. A long-term comparative study between one-line models and models that better describe the depth-contours evolution, such as the Q2Dmorfo model, is necessary to understand the limitations of the one-line approximation and improve the design of mega-nourishments.

The Q2Dmorfo model, once calibrated with the evolution of the ZandMotor, initially overpredicts the cross-shore diffusion, i.e. with a decay rate of the amplitude higher than the observed one. This is due to the initial bathymetric slope, which is much larger than the equilibrium one. Although the cross-shore diffusion can be modulated in the model with the parameter ν, using a low ν value gives rise to artificial shoals. In order to solve this problem, it is necessary to use a cross-shore transport that does not need to prescribe an equilibrium profile but which, at the same time, reaches an equilibrium under constant wave forcing. Nevertheless, the previous issue is only problematic in the first months of simulation and the model as it is allows to further investigate the mega-nourishment dynamics in the mid and long term.

Another limitation of the Q2Dmorfo model is that the shoreline curve has to be univalued and thereby can not describe the formation of spits, which occur when there is a high frequency of unidirectional high-angle waves (Ashton *et al.*, 2001). The use of a fuzzy shoreline algorithm can certainly help to make this improvement. Finally, the present sea-level rise implementation is not yet fully operative because the lateral boundary conditions must be improved. This is an important issue given the long time scales involved in mega-nourishment dynamics, for which the sea level rise induced by climate change may play a role.

Some of the results here obtained with the Q2Dmorfo model deserve further attention. In particular, the reason of the diffusivity decay with volume and shape ratio increments must be analysed in depth. Intuitively, these morphological conditions are characterised by large cross-shore perturbation in the depth contours, which, in case of oblique wave climates, would enhance the instability mechanisms and reduce the diffusivity. This hypothesis could be tested by modelling mega-nourishments with different shape ratios and volumes using different wave climates (i.e. with different frequencies of high-angle waves).

Shoreline sand waves have been observed in a shoreline stretch of the Dungeness Cuspate Foreland. The wave climate is ideal for testing the HAWI and LAWI hypothesis. In agreement with the former, the shoreline sand waves are formed during events were the high-angle incidence wave energy is largely dominant. The 1Dmorfo model captures these formation events despite ignoring the observed 6-m tidal range. However, the model can not describe the subsequent behaviour, i.e. maintenance and even growth of the perturbations, due to the linearity assumption. The good-quality data and the relative small characteristic scales of the observed features allow to use more complex models to simulate its behaviour. In particular, simulations with a two-dimensional non-linear morphodynamic model are required to investigate the finite-amplitude regime and understand the role played by the tides.

Bibliography

Arriaga, J., Falqués, A., Ribas, F. & Crews, E. 2018*a* Formation events of shoreline sand waves on a gravel beach. *Ocean Dynamics* **68** (6), 735–748.

Arriaga, J., Ribas, F., Falqués, A., Rutten, J. & Ruessink, B. 2018*b* Long-term performance of mega-nourishments: role of the initial shape and the wave climate. *Coast. Eng.* In preparation.

Arriaga, J., Ribas, F., Marino-Tapia, I. J. & Falqués, A. 2014 Km-scale shoreline sand waves: numerical modelling and observations. In *Coastal Eng. 2014*. Doi: 10.9753/icce.v34.sediment.68.

Arriaga, J., Rutten, J., Ribas, F., Ruessink, B. & Falqués, A. 2017 Modeling the longterm diffusion and feeding capability of a mega-nourishment. *Coast. Eng.* **121**, 1–13.

Ashton, A. & Murray, A. B. 2006*a* High-angle wave instability and emergent shoreline shapes: 1. Modeling of sand waves, flying spits, and capes. *J.Geophys.Res.* **111**, F04011,doi:10.1029/2005JF000422.

Ashton, A. & Murray, A. B. 2006*b* High-angle wave instability and emergent shoreline shapes: 2. Wave climate analysis and comparisons to nature. *J.Geophys.Res.* **111**, F04012,doi:10.1029/2005JF000423.

Ashton, A., Murray, A. B. & Arnault, O. 2001 Formation of coastline features by large-scale instabilities induced by high-angle waves. *Nature* **414**, 296–300.

Ashton, A. D., Murray, A. B., Littlewood, R., Lewis, D. A. & Hong, P. 2009 Fetch-limited self-organization of elongate water bodies. *Geology* **37**, 187–190.

Battjes, J. A. 1975 Modeling of turbulence in the surfzone. In *Proc. Symp. Model. Tech.*, pp. 1050–1061. Am. Soc. of Civ. Eng., New York.

Blondeaux, P. 2001 Mechanics of coastal forms. *Ann. Rev. Fluid Mech.* **33**, 339–370.

Booij, N., Ris, R. C. & Holthuijsen, L. H. 1999 A third-generation wave model for coastal regions: 1. Model description and validation. *J. Geophys. Res.* **104** (C4), 7649–7666.

Bruun, P. 1962 Sea-level rise as a cause of shore erosion. *J. Waterways abnd Harbours Division* **88**, 117–130.

Calvete, D., Coco, G., Falqués, A. & Dodd, N. 2007 (un)predictability in rip channel systems. *Geophys. Res. Lett.* **34** (L05605), doi:10.1029/2006GL028162.

Calvete, D., Dodd, N., Falqués, A. & van Leeuwen, S. M. 2005 Morphological development of rip channel systems: Normal and near normal wave incidence. *J. Geophys. Res.* **110** (C10006), doi:10.1029/2004JC002803.

Coco, G. & Murray, A. B. 2007 Patterns in the sand: From forcing templates to self-organization. *Geomorphology* **91** (271-290).

Coco, G., O'Hare, T. J. & Huntley, D. A. 1999 Beach cusps: a comparison of data and theories for their formation. *J. Coastal Res.* **15** (3), 741–749.

Cooper, J. & Pilkey, O. 2004 Longshore drift: Trapped in an expected universe. *J. Sediment. Res.* **74**, 599–606.

Davidson-Arnott, R. G. D. & van Heyningen, A. 2003 Migration and sedimentology of longshore sandwaves, Long Point, Lake Erie, Canada. *Sedimentology* **50**, 1123–1137.

de Schipper, M. A., de Vries, S., Ruessink, G., de Zeeuw, R. C., Rutten, J., van Gelder-Mass, C. & Stive, M. J. F. 2016 Initial spreading of a mega feeder nourishment: Observations of the Sand Engine pilot project. *Coastal Eng.* (111), 23–38.

de Schipper, M. A., de Vries, S., Rutten, J. & Aarninkhof, S. 2014 Morphological development of a mega-nourishment; first observations of the Sand Engine. In *Coastal Eng. 2014*. Doi: 10.9753/icce.v34.sediment.73.

Dean, R. G. 2002 *Beach nourishment. Theory and practice*. Singapore: World Scientific.

Deigaard, R., Drønen, N., Fredsoe, J., Jensen, J. H. & Jørgensen, M. P. 1999 A morphological stability analysis for a long straight barred coast. *Coastal Eng.* **36** (3), 171–195.

Dornbusch, U. 2003-2005 BAR Phase I, Beach Material Properties . *Tech. Rep.*. University of Sussex.

van Duin, M. J. P., Wiersma, N. R., Walstra, D. J. R., van Rijn, L. C. & Stive, M. J. F. 2004 Nourishing the shoreface: observations and hindcasting of the Egmond case, The Netherlands. *Coast. Eng.* **51**, 813–837.

Eddison, J. 1983 The evolution of the barrier beaches between fairlight and hythe. *The Geographical Journal* **149**.

Elfrink, B., Prestedge, G., Rocha, C. B. M. & Juhl, J. 2003 Shoreline evolution due to highly oblique incident waves at Walvis bay, Namibia. In *Coastal Sediments'03* (ed. R. Davis, A. J. Sallenger & P. Howd). Cd-rom.

Falqués, A. 2003 On the diffusivity in coastline dynamics. *Geophys. Res. Lett.* **30** (21), 2119, doi:10.1029/2003GL017760.

Falqués, A. 2006 Wave driven alongshore sediment transport and stability of the Dutch coastline. *Coastal Eng.* **53**, 243–254.

Falqués, A. & Calvete, D. 2003 Shoreline sand waves and 1D coastal modelling. In *Coastal Sediments 2003*. World Scientific, iSBN:981-238-422-7(CD-ROM).

Falqués, A. & Calvete, D. 2005 Large scale dynamics of sandy coastlines. Diffusivity and instability. *J. Geophys. Res.* **110** (C03007), doi:10.1029/2004JC002587.

Falqués, A., Calvete, D. & Ribas, F. 2011 Shoreline instability due to very oblique wave incidence: Some remarks on the physics. *J. Coastal Res.* **27** (2), 291–295.

Falqués, A., Garnier, R., Ojeda, E., Ribas, F. & Guillén, J. 2008 Q2D-morfo: a medium to long term model for beach morphodynamics. In *River, Coastal and Estuarine Morphodynamics: RCEM 2007,* vol. 1 (ed. Dohmen-Jansen & Hulscher), pp. 71–78. London: Taylor and Francis Group.

Falqués, A., Ribas, F., Idier, D. & Arriaga, J. 2017 Formation mechanisms for self-organized km-scale shoreline sand waves. *J. Geophys. Res. Earth Surf.* **122**, 10.1002/2016JF003964.

Gardner, M. 1970 Mathematical Games - The fantastic combinations of John Conway's new solitaire game "life". *Scientific American* **223**, 120–123.

Garnier, R., Calvete, D., Falqués, A. & Dodd, N. 2008 Modelling the formation and the long-term behavior of rip channel systems from the deformation of a longshore bar. *J. Geophys. Res.* **113** (C07053), doi:10.1029/2007JC004632.

Grijm, W. 1960 Theoretical forms of shorelines. In *Coastal Eng. 1960*, pp. 197–202. Am. Soc. of Civ. Eng.

Hallermeier, L. 1981 A profile zonation for seasonal sand beaches from wave climate. *Coastal Eng.* **4** (3), 253–277.

Hallermeier, R. J. 1978 Uses for a calculated limit depth to beach erosion. In *Coastal Eng. 1978*, pp. 1493–1512. Am. Soc. of Civ. Eng.

Hamm, L., Capobianco, M., Dette, H. H., Lechuga, A., Spanhoff, R. & Stive, M. J. F. 2002 A summary of European experience with shore nourishment. *Coastal Eng.* **47**, 237–264.

Hanson, H. 1989 Genesis: A generalized shoreline change numerical model. *J. Coastal Res.* **5** (1), 1–27.

Hanson, H. & Larson, M. 2001 Simulating coastal evolution using a new type of n-line model. *Coastal Engineering Proceedings* pp. 2808–2821.

Hinton, C. & Nicholls, R. J. 1998 Spatial and temporal behaviour of depth of closure along the Holland coast. In *Coastal Eng. 1998* (ed. ASCE), pp. 2913–2925.

Idier, D. & Falqués, A. 2014 How kilometric sandy shoreline undulations correlate with wave and morphology characteristics: preliminary analysis on the Atlantic coast of Africa. *Advances in Geosciences* **39**, 55–60, doi:10.5194/adgeo-39-55-2014.

Idier, D., Falqués, A., Rohmer, J. & Arriaga, J. 2017 Self-organized kilometre-scale shoreline sandwave generation: sensitivity to model and physical parameters. *J. Geophys. Res.* **122**, doi:10.1002/2017JF004197.

Idier, D., Falqués, A., Ruessink, B. G. & Garnier, R. 2011 Shoreline instability under low-angle wave incidence. *J. Geophys. Res.* **116** (F04031), doi:10.1029/2010JF001894.

Kaergaard, K. & Fredsoe, J. 2013*a* Numerical modeling of shoreline undulations part 1: Constant wave climate. *Coastal Eng.* **75**, 64–76.

Kaergaard, K. & Fredsoe, J. 2013*b* Numerical modeling of shoreline undulations part 2: Varying wave climate and comparison with observations. *Coastal Eng.* **75**, 77–90.

Kaergaard, K., Fredsoe, J. & Knudsen, S. B. 2012 Coastline undulations on the West Coast of Denmark: Offshore extent, relation to breaker bars and transported sediment volume. *Coastal Eng.* **60**, 109–122.

Komar, P. D. 1998 *Beach Processes and Sedimentation*, 2nd edn. Englewood Cliffs, N.J.: Prentice Hall.

Lewis, W. V. 1932 The Formation of Dungeness Foreland. *Geographical Journal* **80** (4), 309–324.

Long, A. J., Waller, M. P. & Plater, A. J. 2006 Coastal resilience and late Holocene tidal inlet history: The evolution of Dungeness Foreland and the Romney Marsh depositional complex (U.K.). *Geomorphology* **82** (3-4), 309–330.

McGregor, D. F. M. & Green, C. P. 1989 Geomorphology in conservation assessment-The dungeness shingle system. *Ocean and Shoreline Management* **12** (2), 107–124.

Medellín, G., Medina, R., Falqués, A. & González, M. 2008 Coastline sand waves on a low-energy beach at 'El Puntal' spit, Spain. *Mar. Geol.* **250**, 143–156.

Mulder, J. P. M., Hommes, S. & Hostman, E. M. 2011 Implementation of coastal erosion managenement in the netherlands. *Ocean Coast. Manag.* **54**, 888–897.

Ortega-Sánchez, M., Lobo, F. J., López-Ruiz, A., Losada, M. A. & Fernández-Salas, L. M. 2014 The influence of shelf-indenting canyons and infralittoral prograding wedges on coastal morphology: The Carchuna system in Southern Spain. *Mar. Geol.* **347**, 107–122.

Pelnard-Considère, R. 1956 Essai de theorie de l'evolution des formes de rivage en plages de sable et de galets. In *4th Journees de l'Hydraulique, Les Energies de la Mer, Paris*, , vol. III(1), pp. 289–298. Société Hydrotechnique de France.

Redman, J. B. 1882 Sea-Shore Alluvion - Dungeness or Denge-nesse. *Nature* **25** (651), 583–584.

Ribas, F., Falqués, A., van den Berg, N. & Caballeria, M. 2013 Modelling shoreline sand waves on the coasts of Namibia and Angola. *Int. J. Sediment Res.* **28** (3), 1-11.

Ruessink, B. G. & Jeuken, M. C. J. L. 2002 Dunefoot dynamics along the dutch coast. *Earth Surf. Process. Landforms* **27**, 1043–1056.

de Ruig, J. H. M. & Hillen, R. 1997 Developments in Dutch coastline management: Conclusions from the second governmental coastal report. *J. Coastal Conservation* **3**, 203–210.

Ryabchuk, D., Leont'yev, I., Sergeev, A., Nesterova, E., Sukhacheva, L. & Zhamoida, V. 2011 The morphology of sand spits and the genesis of longshore sand waves on the coast of the eastern Gulf of Finland. *Baltica* **24** (1), 13–24.

Schwartz, M. 1984 The Bruun theory of sea-level rise as a cause of shore erosion. *Journal of Geology* **75** (1), 76–92.

Scientific Committee on Ocean Research, Working Group 1991 The response of beaches to sea level changes: a review of predictive models. *J. Coast. Res.* **7**, 895–921.

Stive, M. J. F., de Schipper, M. A., Luijendijk, A. P., Aarninkhof, S. G. J., van Gelder-Maas, C., van Thiel de Vries, J. S. M., de Vries, S., Henriquez, M., Marx, S. & Ranasinghe, R. 2013 A new alternative to saving our beaches from sea-level rise: The sand engine. *Coastal Eng.* **29** (5), 1001–1008.

Sutherland, J., Peet, A. H. & Soulsby, R. L. 2004 Evaluating the performance of morphological models. *Coastal Eng.* **51**, 917–939.

Tonnon, P. K., Huisman, B. J. A., Stam, G. N. & van Rijn, L. C. 2018 Numerical modelling of erosion rates, life span and maintenance volume of mega nourishments. *Coast. Eng.* **131**, 51–69, doi:10.1016/j.ocemod.2012.11.011.

Uguccioni, L., Deigaard, R. & Fredsoe, J. 2006 Instability of a coastline with very oblique wave incidence. In *Coastal Eng. 2006*, pp. 3542–3553. World Scientific.

van den Berg, N. 2012 Modelling the dynamics of large sce shoreline sand waves. PhD thesis, Appl. Physics Dept., Univ. Politècnica de Catalunya, Barcelona, Spain.

van den Berg, N., Falqués, A. & Ribas, F. 2011 Long-term evolution of nourished beaches under high angle wave conditions. *J. Marine Systems* **88**, 102–112.

van den Berg, N., Falqués, A. & Ribas, F. 2012 Modelling large scale shoreline sand waves under oblique wave incidence. *J. Geophys. Res.* **117** (F03019), doi:10.1029/2011JF002177.

van den Berg, N., Falqués, A., Ribas, F. & Caballeria, M. 2014 On the wavelength of self-organized shoreline sand waves. *J. Geophys. Res. Earth Surf.* **119**, 665–681, doi:10.1002/2013JF002751.

van Enckevort, I. M. J., Ruessink, B. G., Coco, G., Suzuki, K., Turner, I. L., Plant, N. G. & Holman, R. A. 2004 Observations of nearshore crescentic sandbars. *J. Geophys. Res.* **109** (C06028), doi:10.1029/2003JC002214.

van Rijn, L. C. 1997 Sediment transport and budget of the central coastal zone of Holland. *Coastal Eng.* **32**, 61–90.

van der Vegt, M., Schuttelaars, H. M. & de Swart, H. E. 2007 Modeling the formation of undulations of the coastline: The role of tides. *Continental Shelf Research* **27** (15), 2014–2031.

Wang, J. D. & LeMehaute, B. 1980 Criterion for stability of shoreline planform. In *Coastal Eng.*, pp. 1295–1305. Am. Soc. of Civ. Eng.

Wang, P., Krauss, N. C. & Davis, R. A. 1998 Total longshore sediment transport rate in the surf zone: field measurements and empirical predictions. *Coastal Res.* **14**, 268–298.

Werner, B. T. & Fink, T. M. 1993 Beach cusps as self-organized patterns. *Science* **260**, 968–971.

Wijnberg, K. M. & Kroon, A. 2002 Barred beaches. *Geomorphology* **48**, 103–120.

Wijnberg, K. M. & Terwindt, J. H. J. 1995 Extracting decadal morphological behavior from high–resolution, long-term bathymetric surveys along the Holland coast using eigenfunction analysis. *Mar. Geol.* **126**, 301–330.

Wright, L. D. & Short, A. D. 1984 Morphodynamic variability of surf zones and beaches: A synthesis. *Mar. Geol.* **56**, 93–118.

Yu, J. & Slinn, D. N. 2003 Effects of wave-current interaction on rip currents. *J. Geophys. Res.* **108** (C33088), doi:10.1029/2001JC001105.

Zenkovitch, V. P. 1959 On the genesis of cuspate spits along lagoon shores. *J. Geol.* **67**, 269–277.

Zimmerman, J. T. F. 1981 Dynamics, diffusion and geomorphological significance of tidal residual eddies. *Nature* **290**, 549–555.